

**DYNAMIC RATING OF TRANSMISSION LINES FOR  
IMPROVED WIND ENERGY INTEGRATION IN  
COMPLEX TERRAIN**

by

Tyler Bennett Phillips

A thesis

submitted in partial fulfillment

of the requirements for the degree of

Master of Science in Mechanical Engineering

Boise State University

May 2014

© 2014  
Tyler Bennett Phillips  
ALL RIGHTS RESERVED

BOISE STATE UNIVERSITY GRADUATE COLLEGE

**DEFENSE COMMITTEE AND FINAL READING APPROVALS**

of the thesis submitted by

Tyler Bennett Phillips

Thesis Title: Dynamic Rating of Transmission Lines for Improved Wind Energy Integration in Complex Terrain

Date of Final Oral Examination: 07 April 2014

The following individuals read and discussed the thesis submitted by student Tyler Bennett Phillips, and they evaluated his presentation and response to questions during the final oral examination. They found that the student passed the final oral examination.

Inanc Senocak, Ph.D. Chair, Supervisory Committee

Joseph C. Guarino, Ph.D. Member, Supervisory Committee

Jake P. Gentle, M.S. Member, Supervisory Committee

The final reading approval of the thesis was granted by Inanc Senocak, Ph.D., Chair of the Supervisory Committee. The thesis was approved for the Graduate College by John R. Pelton, Ph.D., Dean of the Graduate College.

dedicated to my family

## ACKNOWLEDGMENTS

Foremost, I would like to express my gratitude to my advisor, Dr. Inanc Senocak, for presenting me with the opportunity to work on the research discussed in this thesis and guiding me throughout the entire process. This thesis would not have been possible without his continuous support, motivation, and immense knowledge.

I would also like to express my appreciation to Dr. Joe Guarino and Jake Gentle for being members on my thesis committee and the feedback they have provided throughout this work. Review and feedback from Phil Anderson of Idaho Power and Kurt Myers of Idaho National Laboratory was also very appreciated. The weather data Boise State University has received from the collaborative INL and IPCo test bed is also appreciated.

I also would like to thank Micah Sandusky and Rey DeLeon for their help in generating the CFD simulation, as well as everyone who has helped me throughout my studies here at Boise State University. The experience has been very beneficial to me, having been exposed to several new areas of study and learning numerous valuable skills that will most certainly help me throughout my career.

## ABSTRACT

Transmission congestion is a growing concern that could limit integration of new renewable energy projects to the electricity grid. Because construction of new transmission lines is a long and expensive process, transmission service providers (TSP) are investigating dynamic line rating (DLR) methods that could potentially increase capacity of existing transmission lines. DLR is a smart-grid technology that enables rating of power lines based on real-time conductor temperature that is dependent on local weather conditions, whereas conventional practice relies on a static rating, which is based on conservative local weather assumptions to limit transmission line sag.

With today's improved wind and weather models, communication systems, and computing hardware, a computational-based approach for DLR is a possibility. Current thesis research investigates year-long wind patterns over a large test bed area in southern Idaho, in collaboration with Idaho National Laboratory (INL) and Idaho Power Company (IPCo). To instil further confidence in the DLR approach, as proposed in the IEEE Standard 738, the ordinary differential equation (ODE) model that governs conductor temperature change in time has been first validated by coupled computational fluid dynamics (CFD) and heat transfer analysis. Both steady-state and transient thermal rating assumptions have been evaluated using field measurements and high order numerical methods. Under low-wind conditions, it is found that the steady-state thermal rating assumption can cause unnecessary curtailments

of power.

To better model the variation of temperature along the path of a transmission line, a large-eddy simulation (LES) of winds over the moderately complex terrain of the test bed area has been performed using clusters of graphics processing units (GPU). LES results indicate that wind speed as well as direction relative to the transmission line is a critical factor in determining the conductor temperature, which implies that numerical wind models need to provide accurate estimates of wind speed and direction in regions of complex terrain.

# TABLE OF CONTENTS

<b>ABSTRACT</b> .....	vi
<b>LIST OF TABLES</b> .....	xii
<b>LIST OF FIGURES</b> .....	xiii
<b>LIST OF ABBREVIATIONS</b> .....	xix
<b>1 Introduction</b> .....	1
1.1 Background .....	2
1.1.1 Renewable Energy .....	3
1.1.2 Transmission Network .....	3
1.1.3 Operation of Transmission Lines .....	4
1.2 Thesis Statement .....	6
1.3 Works Published .....	9
<b>2 LITERATURE REVIEW</b> .....	10
2.1 Smart-Grid Technology .....	10
2.1.1 Commercial DLR Technologies .....	11
2.2 Current DLR Technology Limitations .....	14
2.3 Dynamic Line Rating Field Test Results .....	15
2.4 DLR Research at Durham University .....	16
2.5 INL & IPCo Collaborative DLR Research .....	17

2.5.1	INL & IPCo CFD Dynamic Rating Method . . . . .	18
2.5.2	Analysis of DLR Capacity Over the INL & IPCo Test Bed . . . .	20
<b>3</b>	<b>Technical Background . . . . .</b>	<b>22</b>
3.1	ACSR Transmission Conductor . . . . .	22
3.2	IEEE Standard 738-2006 . . . . .	24
3.2.1	Steady-State Heat Balance . . . . .	24
3.2.2	Transient Heat Balance . . . . .	26
	Conductor Heat Capacity . . . . .	26
	Conductor Electrical Resistance . . . . .	28
	Solar Heating . . . . .	29
	Convective Cooling . . . . .	32
	Radiative Cooling . . . . .	33
3.3	Numerical Methods . . . . .	34
3.3.1	Euler Method . . . . .	35
3.3.2	Runge-Kutta Method . . . . .	36
3.4	Structure of the Atmospheric Boundary Layer . . . . .	39
3.4.1	ABL Mechanical Turbulence . . . . .	42
3.4.2	ABL Convective Turbulence . . . . .	43
3.4.3	ABL Surface Layer . . . . .	46
	ABL Roughness Sublayer . . . . .	47
3.4.4	ABL Ekman Layer . . . . .	47
3.5	Numerical Wind Modeling and Prediction . . . . .	48
3.6	Turbulence Modeling . . . . .	50
3.6.1	Reynolds-averaged Navier-Stokes Equations . . . . .	51

3.6.2	Large-eddy Simulation Technique . . . . .	53
3.6.3	Turbulence Closure Problem . . . . .	54
3.7	Standard k- $\epsilon$ Turbulent Closure Model . . . . .	55
<b>4</b>	<b>IEEE Standard 738 Validation . . . . .</b>	<b>57</b>
4.1	Computational Setup for the Heated Conductor Analysis . . . . .	57
4.2	Standard Turbulence Wall-Function . . . . .	59
4.3	Conjugate Heat Transfer . . . . .	62
4.4	IEEE Transient Temperature Calculation . . . . .	62
4.5	Steady-State and Transient Heating Validation . . . . .	66
4.6	Conclusion . . . . .	70
<b>5</b>	<b>INL &amp; IPCo Test Bed Analysis . . . . .</b>	<b>72</b>
5.1	INL & IPCo DLR Motivation, Test Bed Area, and Previous DLR Analysis	72
5.2	Weather Station Selection for DLR Analysis . . . . .	77
5.3	DLR Capacity Results . . . . .	80
5.4	Conclusion . . . . .	81
<b>6</b>	<b>DLR Using a Numerical Wind Solver Over Complex Terrain . . . . .</b>	<b>83</b>
6.1	Accelerated Multi-GPU Numerical Wind Solver . . . . .	84
6.2	Application of the Numerical Wind Solver . . . . .	85
6.3	Spatial Variation of Thermal Ratings Across Complex Terrain . . . . .	89
6.4	Conclusion . . . . .	97
<b>7</b>	<b>DLR Utilizing a Transient Conductor Temperature Calculation . . . . .</b>	<b>98</b>
7.1	INL & IPCo Concurrent Cooling Calculation . . . . .	98
7.2	Transient Calculations for Conductor Temperature . . . . .	99

7.2.1	Short-Term Test Case Comparison . . . . .	101
7.2.2	Season Long Test Case Comparison . . . . .	103
7.3	Conclusion . . . . .	105
<b>8</b>	<b>Conclusions and Future Directions . . . . .</b>	<b>106</b>
8.1	Conclusions . . . . .	106
8.2	Future Directions . . . . .	107
	<b>REFERENCES . . . . .</b>	<b>109</b>

## LIST OF TABLES

3.1	Starling 26/7 ACSR physical and electrical properties [48, 85]. . . . .	23
3.2	Specific heat of conductor wire materials as listed in Black and Byrd [15].	27
3.3	Atmosphere correction coefficients [48]. . . . .	31
3.4	Solar azimuth constant, $C$ , as a function of hour angle, $\omega$ , and solar azimuth variable, $\chi$ [48]. . . . .	32
4.1	Normalized L2-norm of conductor temperature. Reference tempera- ture calculated with MATLABs [59] 4 <sup>th</sup> order Runge-Kutta method (ode45) with a time step size of 1 second. . . . .	64
6.1	Calculated conductor temperature using real-time and simulated wind velocity at weather stations. . . . .	96
7.1	Time steady-state and transient methods indicate emergency ratings and curtailment. Temperature calculated using summer real-time weather data with a constant 849 Amp load and maximum solar heating. . . . .	103

## LIST OF FIGURES

2.1	Illustration of transmission span between dead-end structures when insulators are not free to rotate. Conductor temperature will vary along the length of transmission line due to different environmental conditions and tension monitoring systems will give inaccurate results with fixed insulator position [51]. . . . .	13
2.2	Illustration depicting freely swinging insulators that equalize the tension between load cells mounted on dead-end structures giving the average conductor temperature [51]. . . . .	13
3.1	Schematic of ACSR high-voltage transmission cable [44]. . . . .	23
3.2	Diagram of the heat balance within a conductor [45]. . . . .	25
3.3	Transient temperature response to a change in electrical current from a pre-load of 800 Amps to 1,200 and 1,300 Amps. Graph adopted from [48].	27
3.4	(a) The local truncation error over a single time step, denoted by $h$ . (b) Reducing the size of the time step results in a better estimation of the true solution. Illustration adopted from [18]. . . . .	36
3.5	Schematic of the vertical sublayer structure in the atmospheric boundary layer. In this diagram, $h$ is the boundary layer depth, $z$ is height, and $z_0$ is the aerodynamic roughness length [40]. . . . .	40

3.6	Vertical cross-section of the atmospheric boundary layer structure and its typical evolution over land under fair weather, cloud free conditions. Heating from below sets to a convective very turbulent mixing layer during the day, while at night a less turbulent residual layer containing former mixed layer air and a nocturnal stable boundary layer of sporadic turbulence (dark region). Illustration adopted from Stull [88].	41
3.7	Flow over a flat plate. Illustration adopted from [22].	42
3.8	Flow over a two-dimensional ridge showing formation of an increased velocity over the crest and a separation bubble when the downwind slope is steep enough [53].	44
3.9	Vertical pressure gradients in warmer (right) and colder (left) air. Planes symbolize constant pressure levels. Numbers give air pressure in hPa. Capital letters indicate high (H) and low (L) pressure at the surface (lower letters) and on constant height surfaces aloft (upper letters). Arrows indicate a thermally directed circulation. Illustration adapted from Emeis [34].	45
3.10	Turbulent flow velocity fluctuations and time averaged velocity using RANS approach. Illustration adopted from [35].	51
4.1	Computational mesh generated using ICEMCFD. The conductor has been suppressed, only showing the fluid domain for visualization. The mesh quality has a minimum of 0.802 and maximum of 1, and $\sim 98\%$ of the cells having a quality $> 0.9$ .	58

4.2	Closeup view of the computation mesh at the conductor. The fluid, aluminum, and steel zones are shown with small wall-adjacent cell at the conductor. . . . .	59
4.3	Subdivisions of the near-wall region. Adopted from [10]. . . . .	60
4.4	The two near-wall approaches used in turbulence modeling are depicted. The wall function approach is shown on the left, where the flow is not resolved but bridged with the use of a wall function. On the right, the near-wall model approach is shown, here the flow is resolved using a refined mesh near the wall. Illustrations adopted from [10]. . . . .	61
4.5	Transient conductor temperature solution using Euler’s method with 5, 10, and 20 minute time step size. The time step used in the IEEE digitize solution is 1 minute. . . . .	65
4.6	Transient conductor temperature solution using <i>4th</i> order Runge-Kutta method with 5, 10, and 20 minute time step size. The time step used in the IEEE digitize solution is 1 minute. . . . .	65
4.7	ACSR conductor consists of many individual wires but is modeled as two concentric cylinders, aluminum outer with a steel core. The outer diameter and aluminum cross-sectional area are kept constant. . . . .	67
4.8	Validation of IEEE Standard 738 steady state conductor temperature. Laminar flow model was used for low wind velocity, 0.5-3 m/s, and a standard k- $\epsilon$ model with standard wall functions for velocity ranging from 2-10 m/s. Results show different cell-adjacent size near the wall. . . . .	69
4.9	Maximum wall-adjacent $y^+$ value of different wall-adjacent cell size. . . . .	69

4.10	Velocity vectors (top) and temperature contour (bottom) of the laminar CFD simulation. Here the inlet velocity is 1 m/s, giving a Reynolds number $\sim 1,500$ . . . . .	71
5.1	Idaho National Laboratory and Idaho Power’s dynamic line rating research test bed location in southern Idaho [41]. . . . .	75
5.2	Land topology and transmission line’s traversing through INL & IPCo DLR research test bed area [41]. Weather stations are labeled and the location is indicated by a white square. . . . .	76
5.3	Wind velocities at all 17 weather stations from July 2012 through June 2013. Here the box represents the 75 <sup>th</sup> and 25 <sup>th</sup> percentile at the top and bottom, respectively, and the center line indicates the median. . . . .	78
5.4	Seasonal day and night wind velocity from July 2012 to June 2013 at weather stations 7, 16, and 17. The box represents the 75 <sup>th</sup> and 25 <sup>th</sup> percentile at the top and bottom respectively, the center line represents the median. WS7 winter wind velocity data is deficient. . . . .	79
5.5	Winter wind velocity at weather stations 7, 16, and 17. Weather station 7 did not collect data over several large time spans, giving readings of 0 m/s, therefore it has been deemed deficient. . . . .	80
5.6	Hourly seasonal DLR at weather station 17. The horizontal line is the static ampacity and the variable lines represent the 10 <sup>th</sup> – 90 <sup>th</sup> DLR percentile from bottom to top, respectively. . . . .	82
6.1	Seasonal wind velocity and direction. . . . .	87
6.2	Wind contour over the test bed area, having a general wind flow from the west to east direction and $\sim 6$ m/s wind velocity at 10 meters height. . . . .	88

6.3	Example showing a discrete time interval of real-time wind velocity and angle selected for validation. The selected hour long data used is between the vertical dashed lines, when direction and velocity are stable and mimic the boundary conditions imposed on the wind solver. The horizontal dashed line represents wind that is out of the west, blowing in the east direction. . . . .	90
6.4	Initial attempt at validation of wind flow solver over the INL & IPCo test bed area. The mean and standard deviation of real-time hour-long (27 samples) data reading from the summer are compared with the mean wind velocity from the numerical wind solver. . . . .	91
6.5	Superimposed INL & IPCo test bed area and calculated conductor temperature. The flow field incoming velocity resembles a 12.5 mph wind field out of the east. Temperature is calculated assuming 35°C ambient temperature and 12 W/m solar heating. . . . .	92
6.6	Superimposed INL & IPCo test bed area and calculated conductor temperature. The aspect is stretched in the vertical direction by a factor of 6 to better show the terrain. . . . .	93
6.7	Plot of transmission line temperature along its length across the test bed area. Horizontal line represents temperature that indicates emergency ratings, 75°C. . . . .	94
6.8	Plot showing the sensitivity of the wind direction factor, $K_{angle}$ , used in convective cooling equations. Here 0° is wind direction parallel to the conductor and 90° is perpendicular. . . . .	95

7.1	Real-time DLR ampacity using the steady-state calculation procedure as described in [41–43, 45]. . . . .	102
7.2	Real-time conductor temperature comparison using transient and steady-state equations. The horizontal lines represent the temperature where emergency and curtailment temperatures are reached. . . . .	102
7.3	Histogram of conductor temperature using real-time summer weather data and a constant load of 849 Amps and maximum solar heating applied. . . . .	104
7.4	Histogram of conductor temperature above 75°C using real-time summer weather data and a constant load of 849 Amps and maximum solar heating applied. . . . .	104

## LIST OF ABBREVIATIONS

- TSP** – Transmission Service Provider
- DLR** – Dynamic Line Rating
- SLR** – Static Line Rating
- CFD** – Computational Fluid Dynamics
- FERC** – Federal Energy Regulatory Commission
- EIA** – Energy Information Administration
- NERC** – North American Electric Reliability Corporation
- DOE** – Department of Energy
- IEEE** – Institute of Electrical and Electronics Engineers
- INL** – Idaho National Laboratory
- IPCo** – Idaho Power Company
- EPRI** – Electric Power Research Institute
- ERCOT** – Electric Reliability Council of Texas
- WWPTO** – Wind and Water Power Technology Office
- RANS** – Reynold-Average Navier-Stokes
- ACSR** – Aluminum Conductor Steel Reinforced
- ABL** – Atmospheric Boundary Layer

**CIGRE** – Conseil International des Grands Reseaux Electriques

**ODE** – Ordinary Differential Equation

**IVP** – Initial Value Problem

**RK** – Runge-Kutta

**WAsP** – Wind Analysis and Application Program

**NS** – Navier-Stokes

**NWP** – Numerical Weather Prediction

**DNS** – Direct Numerical Simulation

**LES** – Large-eddy Simulation

**SGS** – Subgrid-scales

**WS** – Weather Station

**GPU** – Graphics Processing Unit

**BSU** – Boise State University

**MPI** – Message Passing Interface

**CUDA** – Compute Unified Device Architecture

**IBM** – Immersed Boundary Method

## CHAPTER 1

### INTRODUCTION

U.S. utilities have long been under government sanctioned regulation, however they are now shifting towards a deregulated market. This has put increased pressure on transmission service providers (TSP) to increase energy transfer capacity on the existing transmission grid. Over the last several decades utility investment on transmission infrastructure has not kept pace with the growing generation and capacity needs [97]. Many transmission lines are already congested, and the electricity demand is predicted to grow 28% by 2040 [5]. TSPs are investigating alternative technologies such as dynamic line rating (DLR) to increase transmission capacity.

Congestion in existing transmission lines is a growing concern. Construction of new transmission lines is a difficult and lengthy process, and may not be an economical solution for congestion relief. Renewable energy projects, such as wind farms, can be dismissed if proximity to adequate transmission lines is not available [19, 83]. Completed wind projects are routinely connected to the existing congested network. However, most transmission lines are operated under the conventional static line rating (SLR) system, and there may be excess capacity not being utilized. Research has shown there is a strong connection between wind power output and transmission line ratings [13]. Implementing a DLR system can potentially increase the capacity of transmission lines, eliminating the need to build new transmission lines.

Current DLR technologies used in industry include direct line sag, line tension, and conductor temperature measurements. These technologies are expensive per unit and typically don't take enough measurements to give an accurate assessment of the variation of conductor temperature along its length [42]. Current DLR technologies only allow average temperature calculations over large transmission spans or single point temperature measurements. Application of these systems is also not clear in regions of complex terrain.

With today's improved wind and weather modeling, communication systems, and computational capabilities, using computer simulations to determine conductor capacity has become a possibility. An approach utilizing computer simulations potentially allows dense temperature calculations along transmission lines and has the advantage of implementation without de-energizing the lines.

However, as with any computational simulation approach, capability needs to be tested and validated before actual implementation. Therefore, one of the major goals of this thesis research is to critically investigate a DLR system using year-long weather data collected over a test bed area and computational fluid dynamics (CFD) simulations over complex terrain.

## 1.1 Background

Recently the U.S. electric industry has undergone changes in the way it delivers electricity, it's slowly being deregulated toward a competitive market for transmission and generation. The Public Utility Holding Company Act of 1935 [23] gave utilities a government sanctioned monopoly over a given territory. Only minor alterations were made until substantial reforms occurred by the passage of the Energy Policy Act of

1992 [91]. In 1996, the Federal Energy Regulatory Commission (FERC) issued order 888 [67] requiring all public utilities to open their transmission lines to competitors. The commission's goal was to remove impediments to competition in the wholesale of bulk power and bring more efficient, lower cost power to consumers.

### **1.1.1 Renewable Energy**

Due to favorable regulatory frameworks, wind energy has maintained rapid growth over the past decade. The U.S. Energy Information Administration (EIA) projects the wind energy growth to continue over the next 30 years [5]. According to the North American Electric Reliability Corporation (NERC), approximately 260,000 MW of new renewable capacity is projected over the coming ten years, of which wind will account for approximately 88% [24]. However, increasing the percentage of wind energy in the overall energy portfolio is much more complex than simply installing wind farms in windy areas. In the 20% Wind by 2030 technical report [68], the Department of Energy (DOE) has recognized the many challenges involved in increasing the amount of wind energy resources in overall electricity production. One of the largest challenges being the lack of adequate transmission infrastructure.

### **1.1.2 Transmission Network**

Since the 1970s, investment in transmission line infrastructure has lagged behind the growth of power demand and new generation [97]. Energy secretary Bill Richardson referred to the U.S. transmission network as a "third-world grid" [95]. However, upgrading the transmission network is not an easy task; under the best circumstances, the process to plan, permit, and construct transmission lines is a difficult one [83]. There are a host of environmental and regulatory challenges that

need to be met along with the siting of new transmission lines. However, public opposition is often the largest barrier of new transmission projects [93, 97]. The frequently cited poster child is the American Electric Power Wyoming-Jacksons Ferry line that took 16 years to site and construct in Virginia [24]. According to FERC, between 2000 and mid-2007, only 14 interstate high-voltage transmission lines, with a total length of 668 miles, have been built [63]. This compares with current proposals to build many thousands of miles of new long-distance transmission lines [54]. Almost a quarter of the newly constructed transmission is specifically linked to the integration of renewable generation [25].

Construction of new high-voltage transmission lines typically takes 7–10 years to plan, permit, and erect, costing upward of \$1 million per mile [19, 97]. In its 2009 Scenario Reliability Assessment [24], NERC stated over 40,000 miles of new transmission is needed to achieve 15% generation from renewable sources. A DOE study [68] on expanding the use of wind power estimated transmission expansion to cost \$60 billion by 2030. Such a level of investments may enable the industry to meet the state mandated renewable energy portfolio standards.

Ultimately, an aging transmission network is a barrier to rolling out more renewable sources. It's easier and faster to site renewable generation than the needed transmission [19, 83]. Clearly, any technology developments that lead to an increase of capacity on existing transmission lines will help renewable energy project installation by relieving the need for new transmission lines.

### **1.1.3 Operation of Transmission Lines**

The move toward a deregulated market, the rising electricity demand, and renewable energy targets, has put pressure on TSPs to maximize utilization of existing

transmission network [38,39]. TSPs commonly rely on SLR methods that are based on historical weather to determine a conductor's ampacity. Ampacity is the maximum electrical current a line can carry without exceeding its sag limit or the annealing onset temperature of the conductor, whichever is lower [57,99]. There are several environmental variables that affect the conductor temperature, such as wind speed and direction, ambient temperature, and solar radiation. As these are difficult to predict, SLR often assumes conservative assumptions, such as full sun, high ambient temperature, and low wind speeds [30,31]. The conservative assumptions are used to prevent overheating of the conductor, resulting in low ground clearance, which might interfere with public safety. However, SLR conservative assumptions can often cause unnecessary curtailments for wind power generation [69].

DLR is a smart-grid technology that allows the rating of power lines to be based on real-time conductor temperature dependent on local weather conditions. Wind speed and its direction relative to the power line are two major factors contributing to a conductor's temperature. Research has shown a natural synergy exists between wind power generation and conductor cooling [13].

Trial site studies have shown switching from current SLR to DLR can increase capacity by 20–70%, depending on location. Potential benefits of implementing a DLR technology includes improved system reliability and safety, reduce capital expenditures, increased efficiency of generation resources, and lower rates for utility customers.

DLR technologies used in industry today include direct line sag, line tension, and conductor temperature measurements. Sag and tension monitoring systems only give the average sag/tension measurement over large transmission sections, therefore only the average conductor temperature over the given section can be calculated. On the

other hand, direct temperature measurement systems only give information at a single fixed point location. The concern with these systems is that they typically don't take enough measurements to give an assessment of the variation of temperature along a conductor's length [42], potentially leading to an over estimation of actual ratings [81]. This may lead to unknowingly overloading transmission lines, which could potentially put the public in danger. However, a DLR system based on numerical wind prediction potentially allows for conductor temperatures to be monitored along its path at dense intervals. Equally important, this technology may not require large investments like current technologies, or have safety concerns during installation. Therefore, a computationally-based DLR technology that can safely be put into operation to expand transmission capacity is very attractive for TSPs.

## 1.2 Thesis Statement

The present thesis research aims to provide a foundation for a computationally-based DLR system that can estimate the conductor temperature at dense intervals along a transmission line crossing a complex terrain region in real-time. The specific objectives of the present thesis research are as follows:

- Validate the theoretical formulation presented in the Institute of Electrical and Electronics Engineering (IEEE) Standard 738-2006 using detailed CFD analysis of a heated conductor in cross-flow.
- Investigate transmission capacity in the Idaho National Laboratory (INL) and Idaho Power Company (IPCo) test bed area using year-long weather data broken into seasonal and daily periods.

- Apply real-time weather data to the transient thermal rating approach to calculate conductor temperature, and compare it against the real-time steady-state thermal rating procedure presented in [41–43, 45].
- Adopt high order numerical methods in the transient thermal rating approach and assess the benefits.
- Apply a large-eddy simulation (LES) based numerical wind solver over a moderately complex terrain, and investigate the feasibility of a computationally based DLR system over a large area.

The present thesis is organized in the following way:

Chapter 2 summarizes the smart-grid and contributing role DLR has. Today's commercially available DLR technologies are listed and details are given on systems commonly used in practice. This is followed by the limitations facing current DLR technologies as well as field test results. DLR research conducted at Durham University and the joint efforts of INL & IPCo are also summarized.

Chapter 3 is devoted to describing the IEEE Standard 738-2006 in detail. Necessary background on the Starling 26/7 ACSR conductor used in the analysis throughout this thesis is given. Sufficient detail on the numerical methods used to solve the IEEE ordinary differential equation (ODE), which governs conductors temperature change in time, are covered and the atmospheric boundary layer is introduced. Surface layer turbulence, where wind turbines and transmission lines reside, is explained and details in numerical wind modeling relevant to the present thesis research is presented.

Chapter 4 presents the steps taken to validate the IEEE standard equations used in DLR calculations. ANSYS FLUENT software is used to simulate the conjugate heat transfer problem between transmission conductor and ambient wind flow, and a

comparison to numerical results using IEEE equations is completed. The model, computational mesh generation, and CFD numerical processing are described in sufficient details.

Chapter 5 summarizes the assessment on the increase in transmission line capacity DLR may potentially allow if implemented over the INL & IPCo test bed area. The test bed location and topology as well as weather measuring instrumentation is sufficiently described. Capacity results are given for each season of the year as well as the hourly evolution due to the diurnal cycle of wind across the region.

Chapter 6 is devoted to the application of a LES-based wind solver over moderately complex terrain within a hypothetical DLR system to determine conductor temperature along a transmission line in real-time. Wind simulation results are compared against weather station data collected over the INL & IPCo test bed area.

Chapter 7 is devoted to assess transient versus steady-state thermal rating methods to calculate the real-time ampacity of transmission conductor. Both methods make use of real-time season-long weather data, and the resulting conductor temperature calculations are compared to draw conclusions on their applicability.

Chapter 8 gives concluding remarks and suggests future work for successful implementation of a DLR method over complex terrain regions.

### 1.3 Works Published

Works published during the course of this study:

- T. Phillips, I. Senocak, J. Gentle, K. Myers, P. Anderson “Investigation of a Dynamic Power Line Rating Concept for Improved Wind Energy Integration Over Complex Terrain,” 4th Joint US European Fluids Engineering Division Summer Meeting, August 2014.

## CHAPTER 2

### LITERATURE REVIEW

Transmission congestion is a growing concern that could limit integration of new renewable energy projects. The construction of new transmission lines is a long and expensive process, so TSPs are investigating DLR technologies that can increase the capacity of existing transmission lines.

This chapter presents a review of the smart-grid, as well as current DLR technologies, including direct sag, line tension, and conductor temperature measurements. Additionally, the on-going research at Durham University and the joint efforts by INL & IPCo is covered in sufficient detail.

#### 2.1 Smart-Grid Technology

The current electrical grid was initiated over 100 years ago when electricity needs were simple. Power generation was localized, built around communities with a one-way interaction from generation to consumers. This limited one-way interaction makes it difficult for the grid to respond to renewable generation and the rapidly changing demands of modern society and industry. Smart-grid technologies promise a two-way dialog, where electricity and information are exchanged between generation and electrical consumers in real-time [3]. It's an evolving network of communication, controls, computers, and automation working together to make the grid more efficient,

reliable, and secure, while enabling better integration of new renewable technologies, such as wind and solar power [29].

One fundamental component of the smart-grid is more efficient transmission of electricity. It's critical for TSPs to know the maximum electrical capacity that can be transmitted at any given time [47]. The idea of DLR for efficient transmission has been around for a long time, it is an economic and effective way of upgrading overhead power lines [66, 87]; however, it has proven difficult in practice. Public safety is of utmost importance, concerns over the uncertainty in DLR have kept TSPs reluctant to adopt such technologies. Over the last couple of decades, there has been research, testing, pilots, demos, and actual use of DLR systems in several locations with a number of commercial methods and equipment [11, 47, 74, 99]. The smart-grid and DLR represents an unprecedented opportunity to move the energy industry into a new era of reliability, availability, and efficiency that will contribute to our economic and environmental health [3].

Several commercial DLR technologies are available, however these systems are not widely adopted in practice. Some of the DLR technologies used in industry today include direct line sag, line tension, and conductor temperature measurements. Other direct systems not as widely used include the Ampacimon [8] and Promethean RT-TLM [28]. Two available indirect systems are the ThermalRate [71] and Alstom P341 [7]. The most common DLR systems are briefly described in the order of their development, followed by the limitations these technologies face.

### **2.1.1 Commercial DLR Technologies**

Underground Systems Inc. (USi) Power Donut was developed in 1988. The Power Donut is directly attached to transmission conductor measuring the current, voltage,

temperature, and angle of inclination. The inclination angle is used to calculate the conductor sag, which has been validated within 5 inches in 30 feet [92], and the accuracy of conductor surface temperature is within  $\pm 1$  °C [37]. According to USi, more than 1,000 Power Donuts have been installed between 1988 and 2012.

CAT-1 is a tension monitoring system developed by the Valley Group (currently under Nexans) in 1990 [4]. Today there are over 300 tension monitoring systems installed by over 100 utilities in more than 20 countries. CAT-1 load cells are attached at dead-end structures where they monitor the mechanical tension of the conductor. When tension monitoring is implemented, insulators between dead-end structures must be freely rotating to equalize the tension along the span. If the insulators do not rotate correctly, the system can give inaccurate tension readings; this is illustrated in Figure 2.1. Freely rotating insulators will equalize the tension as illustrated in Figure 2.2. CAT-1 system measurements give the average tension between load cells. The tension is then used to calculate the conductors average temperature over the given span.

Span Sentry also know as the Sagometer was developed by Electric Power Research Institute (EPRI) and sponsoring utilities in 1997 [12]. It was first installed in 1999 and over 80 Sagometer units are installed throughout North America today. The Sagometer uses a digital video camera with near infrared laser technology to capture a targets position that is attached to the conductor. The accuracy of conductor sag using the Sagometer is  $\pm 15$  mm [92]. Like tension systems, the insulators must be free to rotate between dead-end structures for the Sagometer to give accurate measurements. This systems will only indicate the conductor's average sag between dead-end structures.

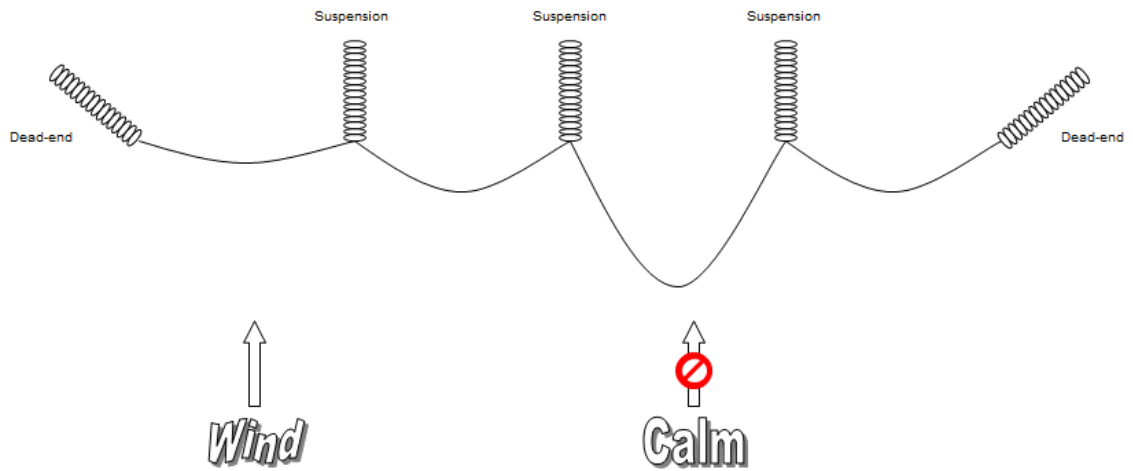


Figure 2.1: Illustration of transmission span between dead-end structures when insulators are not free to rotate. Conductor temperature will vary along the length of transmission line due to different environmental conditions and tension monitoring systems will give inaccurate results with fixed insulator position [51].

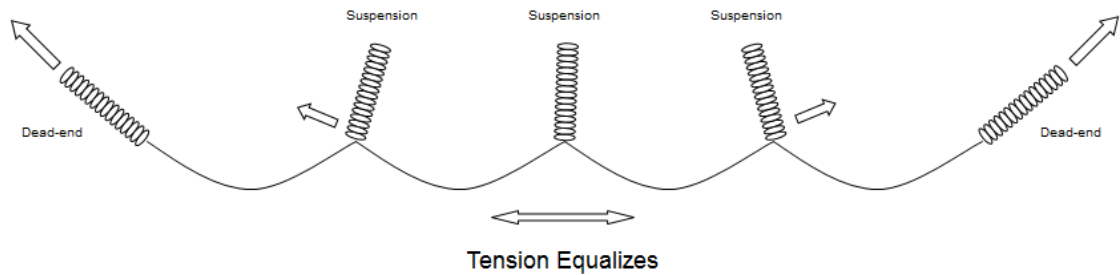


Figure 2.2: Illustration depicting freely swinging insulators that equalize the tension between load cells mounted on dead-end structures giving the average conductor temperature [51].

## 2.2 Current DLR Technology Limitations

It has been observed that conductor temperature can vary significantly along its length [33] due to variation of environmental conditions. In complex terrain, wind velocity and its direction are highly dependent on the physical surface topology, therefore conductor temperature can have large spatial variation. According to Seppa et al. [81], monitoring the line in a few discrete locations would lead to severe over or under estimations of actual line ratings. Measurements have shown spatial line temperature variation in a single span can amount to 10–20°C [80]. A 363 meter long transmission test site at Oak Ridge National Laboratory [81], sheltered by 15 meter tall trees at one end, have shown longitudinal temperature difference between a single span, 180 meters, to be 29°C. The same test site has shown above ground elevation change of 4.3–10.6 meters can cause temperature to vary by an average of 20°C.

The concern with current DLR technologies is that they typically don't take enough measurements to give an accurate assessment of the spatial varying conductor temperature [42], potentially leading to over estimation of actual ratings [81]. Sag and tension monitoring systems only give the average measurement over large transmission section, therefore only the average conductor temperature over the given section can be calculated. Direct temperature measurements are only taken at a single fixed point location and are often placed near the dead-end structure, at the apex of transmission line height. This practice can result in underestimating the conductor temperature because of the elevated winds at the apex location. Additionally, in complex terrain, dead-end structures are often placed on elevated hill tops, where wind velocity is generally higher. Furthermore, direct measurement sensors mounted on a conductor represents a heat sink and tests have indicated unacceptable transmission temperature

reductions of 15–20% [81].

Adding more monitoring devices would be a potential solution of the limitations facing current DLR technologies, however these systems are typically expensive, requiring many instruments to reduce error to an acceptable level [41]. Equally important, implementation of direct measurement systems can prove to be challenging, as transmission lines may need to be de-energized during installation.

### **2.3 Dynamic Line Rating Field Test Results**

The Electric Reliability Council of Texas (ERCOT) is one of eight regional reliability councils in North America. It's responsible for ensuring the reliability of the electrical network connecting 23 million Texas customers [36]. ERCOT schedules power on an electric grid with 72,500 kilometers of transmission line. In order to fully meet the interest of market participants, ERCOT has implemented an indirect DLR system, the primary purpose is to improve the economic efficiency by reflecting the change of real-time ambient weather temperature on the ratings of transmission lines. ERCOT receives temperature data from various TSPs via telemetry, on which real-time dynamic rating are determined. The increased transmission capacity using real-time ambient temperature is given in [47]; the capacity fluctuates throughout the day and lower ambient temperature during the winter provides additional conductor cooling.

San Diego Gas and Electric tested the feasibility and reliability of DLR in their system in the late 1990s. A CAT-1 tension monitoring system was installed on a 230 kV transmission line that limits electrical import capability. Data was collected from April through July of 1999; it indicated that the monitored line could increase

ampacity between 40–80% when using real-time conditions instead of static ratings. This increase would result in significant capital cost savings in deferred transmission line projects and improved usage of existing generation resources [74].

Eco Central Networks UK has been using dynamic ratings on the 40 km Skegness-Boston 132 kV transmission line. The ratings are calculated using local weather measurements from two weather stations mounted in Skegness and Boston at the transmission line ends. The DLR uses an assumed solar heating value as well as an angle of  $20^\circ$  due to the variable wind and transmission line directions. USi Power Donut units are used to directly monitor the line temperature in three locations. Comparison of line measurements and calculated temperature values are reported to have rather good correspondence with each other. Using the DLR monitoring system on the Skegness-Boston line enables 20–50% more wind generation to be connected to the grid [11, 99].

## 2.4 DLR Research at Durham University

The DLR trial site in the UK is 43 square kilometers in North Wales, located just south of the coast. The terrain features a large valley containing small towns, villages, and forest. A section of transmission line approximately 20 km long, containing 5 weather stations spaced between 1 and 5 km apart is used for validation of their DLR technique.

The environmental conditions at weather stations are read in real-time and an inverse distance interpolation technique [82] is used to estimate environmental conditions in every component location. At each point in the geographical area, the value of a parameter is estimated as a weighted average of the parameter values known at

$n$  points,  $i_1, i_2, \dots, i_n$ . The weighting factor is a function of the distance between the points. For example, wind speed,  $W_s$ , is estimated with

$$W_{s_k} = \frac{\sum [(1/l_{i,k}^2) W_{s_i}]}{\sum (1/l_{i,k}^2)}, \quad (2.1)$$

where  $k$  and  $l$  are the point location and distance between the points, respectively. This method is also used for the estimation of wind direction, solar radiation, and ambient temperature. Ground roughness is taken into account using the log-law for the determination of wind speed change in height [45].

To account for the uncertainties a probability distribution for each variable is assumed, with all variables being treated statistically independent of one another. The functions involved are quite complicated and analytic derivation of the probability distribution of the line rating is not feasible. Therefore, the Monte Carlo method is employed, samples from the probability distributions of the input variables are used for deterministic calculations of the output. The results approximate the probability distribution of the line rating [45, 62].

Trial results conducted in the winter of 2008/2009 when low ambient temperatures dominate line cooling can be found in [62]. Results from the 2009 summer when wind speed and direction dominate line cooling is given in [46]. The method does not perform as well in the summer, and as a result, work to improve wind speed and direction estimation using CFD calculations is ongoing.

## 2.5 INL & IPCo Collaborative DLR Research

INL with funding from the DOE through the Wind and Water Power Technology Office (WWPTO), and IPCo have been working on a DLR project with the aim to

alleviate the problems current DLR technologies face. They have installed weather measurement equipment along high voltage transmission lines at 17 locations. The weather equipment collects wind speed, wind direction, ambient air temperature, and solar irradiation. The solar irradiation data was not available for the work conducted in this study. Using weather station data, they have developed a system to dynamically rate transmission lines in real-time with the use of CFD computer simulations. Development of the system is currently ongoing and some of the research is protected under critical infrastructure information. Additionally, they have completed an analysis of the increased transmission capacity associated with a DLR system using real-time weather station data. The DLR test site and instrumentation is fully described in Section 5.1, it's the same test site used throughout this thesis work.

### **2.5.1 INL & IPCo CFD Dynamic Rating Method**

The DLR system developed by INL and IPCo [41–43, 45] uses large volumes of weather and environmental measurements to perform CFD simulations. The land topography, surface roughness of the terrain, and wind conditions at the 17 weather stations are used to initialize the CFD simulations over the test area. The project team uses WindSim CFD software, which calculates the wind field with conventional steady-state 3-D RANS (Reynolds-averaged Navier-Stokes) equations and the  $k-\epsilon$  turbulence model. This technique allows wind velocity and direction to be calculated where no telemetry is available.

A digital terrain model of the area is created with a length scale sufficient to describe the geography within the applied mesh, according to the phenomenon under consideration. The mesh is created using a body-fitted-coordinates mesh over the

digital terrain model, capturing hills, valleys, ridges, and other large topographical features. A variable spaced mesh is used in the vertical direction to provide more refinement near the ground where large wind velocity gradients exist. The finished mesh incorporates  $\sim 48$  million cells in the domain, covering a land area roughly  $40 \times 37.5$  kilometers.

In addition to the topographical land forms, surface roughness is also input into the model accounting for terrain effects that are smaller than the mesh: such as trees, shrubs, and buildings. The WindSim model is too computationally intensive to be executed in real-time. Therefore, the project team adopts a library approach, which uses a database of pre-simulated results. The real-time weather station readings are then used to lookup a pre-simulated result that most accurately matches the real-time weather data. The wind conditions from the selected simulation are then used to solve the IEEE steady-state thermal rating, Equation 3.3, and determine the ampacity along the entire transmission line.

A blind study using wind velocity data from a mobile meteorological tower has been done in several locations to “gage” the accuracy of wind speed modeling using this method [41,43,45]. The comparison is made between real-time field measurements and  $\pm 20\%$  simulated wind speeds at a single model point. Although the wind speed measured by the mobile meteorological tower at times exceeds the 20% error generated from the model, measured results during the majority of the time are within this range. Wind speed is typically only outside the 20% error for 3 minute time sample. In general, modeled results at the single test point appear to be more accurate at higher wind speeds than at lower wind speeds.

The IEEE steady-state thermal rating equation has been adopted to calculate the real-time conductor temperature, on the grounds of thermal time constant of

conductor is typically 10–20 minutes [98]. However, during times of rapidly changing environmental or electrical current conditions, the INL & IPCo DLR method using the steady-state thermal rating equation assumption may not accurately predict the conductors true temperature, due to a conductor heat capacity.

It's expected that an approach that calculates the transient temperature response of conductor potentially leads to more accurate assessment of conductor's temperature. Increased information about the conductor's actual thermal condition may allow TSPs to transfer energy more efficiently and reliable. Therefore, one of the goals of this thesis is to further assess the use of steady-state assumptions when determining real-time ratings. Transient and steady-state conductor temperature calculations will be completed using real-time weather data collected over the INL & IPCo test bed area for comparison.

### **2.5.2 Analysis of DLR Capacity Over the INL & IPCo Test Bed**

INL & IPCo conducted a study on the potential transmission capacity rating due to a hypothetical DLR implementation. Results from their study can be found in [41]. The increase of transmission capacity has been calculated for summer and winter conditions, using different average wind speed and direction. Summer results indicate capacity can potentially be increased by 35–95% and winter ratings by 98–177%.

INL & IPCO analysis does not further breakdown the potential transmission changes into daily and seasonal changes. The variable nature of the wind throughout the day can impact transmission capacity estimates. Wind exhibits a diurnal patten generally having higher velocity during the day than at night [80]. Additionally, capacity calculations using seasonally averaged wind speeds may not best represent

the wind speeds. Generally wind speed doesn't follow a normal distribution; a Weibull distribution is a better fit [58].

Therefore, a goal of this thesis is to expand on the DLR weather data analysis done by INL & IPCo to provide a critical assessment of the DLR technology. The analysis done in this thesis uses year-long real-time weather station data to determine the probability of capacity occurring at different hours of the day during each season.

## CHAPTER 3

### TECHNICAL BACKGROUND

This chapter gives detailed background information on the IEEE Standard 738-2006 equations for calculating over-head conductor temperature. The IEEE Standard equations as well as the numerical methods used in calculation of the ODE representing conductor transient temperature change in time are described in sufficient detail. Background on high-voltage aluminum conductor steel reinforced (ACSR) transmission conductor is also provided. The structures of the atmospheric boundary layer (ABL) where wind turbines and transmission conductor reside is explained and the theory of turbulence modeling with CFD is described.

#### 3.1 ACSR Transmission Conductor

Because of its broad adoption in practice, ACSR has been chosen for the present analysis, however it doesn't represent actual conductor used by ICo. ACSR stands for aluminum conductor steel reinforced, other conductor options are all aluminum, aluminum alloy, and copper. Copper is a better conductor than aluminum, however it is more expensive and has a higher density, requiring additional reinforcement on support towers. ACSR's most desirable property is its high strength-to-weight ratio, while maintaining good conductivity. For this reason, it is common to use ACSR in medium and high-voltage transmission lines.

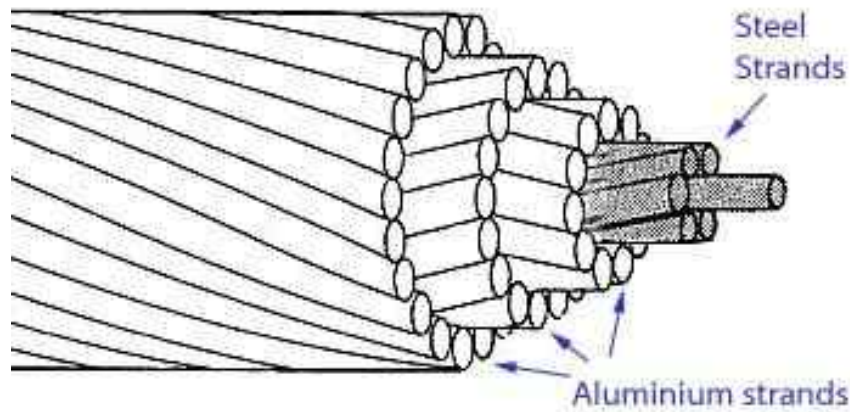


Figure 3.1: Schematic of ACSR high-voltage transmission cable [44].

Table 3.1: Starling 26/7 ACSR physical and electrical properties [48, 85].

Property	Value	Unit
Conductor nominal diameter	2.667	[cm]
Aluminum wire diameter	4.214	[mm]
Steel wire diameter	3.277	[mm]
Resistance at 25°C	8.00525	[Ω/m]
Resistance at 75°C	9.58005	[Ω/m]
Aluminum specific heat	955	[J/kg·°C]
Steel specific heat	476	[J/kg·°C]

ACSR is not a single wire but comprised of several aluminum and steel strands built in a spiraled configuration. The stranded design is used to give flexibility in the cable [76]. Figure 3.1 shows a schematic of 54/7 ACSR cable; it consist of 54 outer strands of aluminum wire and 7 center strands of steel wire. Starling 26/7 ACSR conductor is used in the analysis throughout this thesis work. Table 3.1 gives the physical and electrical properties of the conductor.

## 3.2 IEEE Standard 738-2006

In engineering practice, thermal ratings of overhead lines are normally calculated using one of two standards: the Institute of Electrical and Electronics Engineers (IEEE) [48] or the Conseil International des Grands Reseaux Electriques (CIGRE) [20]. Both standards follow the same concept, the balance of the heat equation. In this study, the IEEE standard 738-2006 for calculating the temperature of bare overhead conductors is used. Conductor temperature is a function of the conductor material properties, conductor diameter, conductor surface condition, ambient weather conditions, and conductor electrical current. IEEE conducted a study on various methods for calculating the heat equation to find the ampacity of transmission line conductor. The mathematical model selected in the IEEE 738 standard is based on the House and Tuttle method, as modified by ECAR [1]. The House and Tuttle formulas consider all of the essential factors without the simplifications that were made in other formulas.

### 3.2.1 Steady-State Heat Balance

Transmission conductor is heated from solar radiation and electrical current, and it's cooled via convection and radiation, as illustrated in Figure 3.2. The conductor is at a steady-state thermal condition when the heat generated in the conductor equals the heat lost to the surroundings. The steady-state heat balance equation is given by

$$q_c + q_r = q_s + q_j, \quad (3.1)$$

where  $q_c$  is the conductor convective heat loss,  $q_r$  is the conductor radiated heat loss,  $q_s$  is the conductor solar heat gain, and  $q_j$  is the joule or resistance heating.

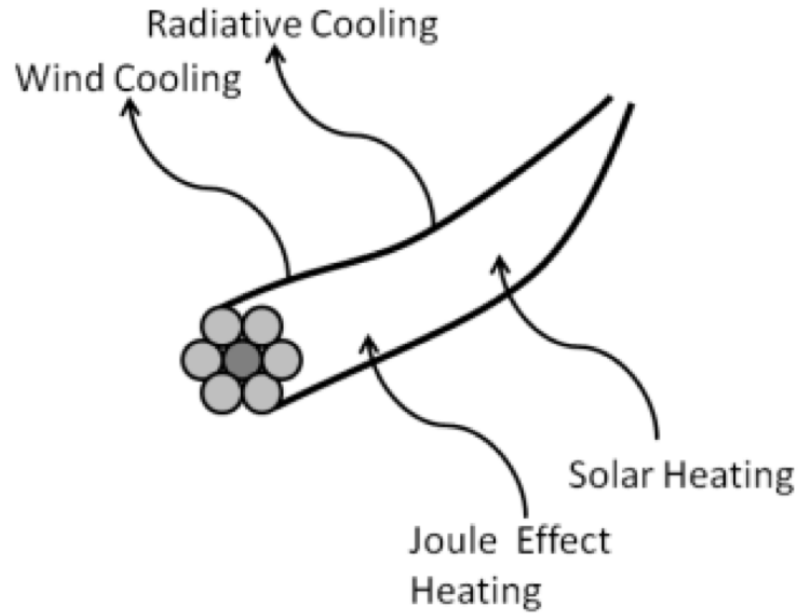


Figure 3.2: Diagram of the heat balance within a conductor [45].

Joule heating is the process of heat generation due to the passage of electrical current through a conductor. It's the main source of heating in transmission line conductors, especially under high loading conditions. The Joule heating is given as

$$q_j = I^2 R(T_c), \quad (3.2)$$

where  $I$  is the electrical current,  $R$  is the resistance, and  $T_c$  is the conductor temperature.

The steady-state thermal rating is defined as the constant electrical current that would yield the maximum allowable conductor temperature for specified weather conditions and conductor characteristics under the assumption that the conductor is in thermal equilibrium. The steady-state thermal rating is therefore calculated as follows

$$I = \sqrt{\frac{q_c + q_r - q_s}{R(T_c)}}, \quad (3.3)$$

and is used to calculate the steady-state ampacity using the resistance of conductor at its maximum permissible temperature. It is used in the DLR calculation procedure described in [41–43, 45].

### 3.2.2 Transient Heat Balance

The temperature of overhead power line conductors are constantly changing in response to changes in weather and electrical current. When a conductor at a steady-state condition undergoes weather or electrical current changes, its temperature will change in time, reaching a new steady-state temperature. A transient temperature response to a change in electrical current is shown in Figure 3.3. The rate of change the conductor experiences is calculated using the transient heat balance equation. It is expressed as

$$\frac{dT_c}{dt} = \frac{1}{mC_p} [q_j + q_s - q_c - q_r], \quad (3.4)$$

where  $mC_p$  is the total heat capacity of the conductor. The real-time conductor temperature and its change in time, represented by this ODE, is calculated using high order numerical methods in this study.

### Conductor Heat Capacity

The conductor heat capacity is defined as the product of specific heat and mass per unit length. Because the conductor is composed of multiple wires of different material, the heat capacity is calculated as the sum of individual heat capacities. The calculated heat capacity is given as

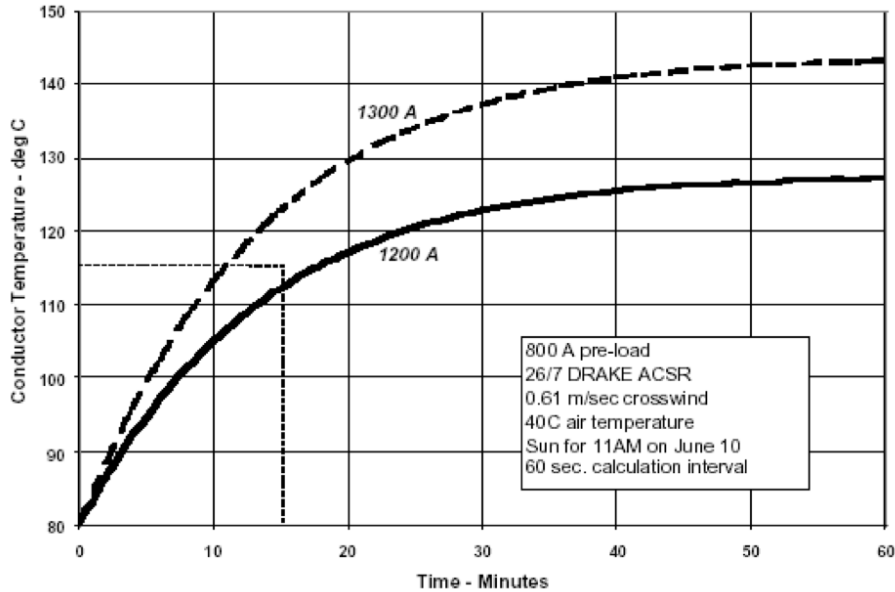


Figure 3.3: Transient temperature response to a change in electrical current from a pre-load of 800 Amps to 1,200 and 1,300 Amps. Graph adopted from [48].

$$mC_p = \sum m_i C_{pi}, \quad (3.5)$$

where  $m_i$  and  $C_{pi}$  are the mass per unit length of  $i^{th}$  conductor material and the specific heat of  $i^{th}$  conductor material, respectively. Values for specific heat of common metals used in stranded overhead conductors are listed in Black and Byrd [15]; they are given in Table 3.2.

Table 3.2: Specific heat of conductor wire materials as listed in Black and Byrd [15].

Material	Specific Heat [J/kg·°C]
Aluminum	955
Steel	476
Copper	423

## Conductor Electrical Resistance

The electrical resistance of bare stranded conductor varies with frequency, average current density, and temperature. The Aluminum Electrical Conductor Handbook [2] and Southwire [85] give calculated values of electrical resistance for 60 Hz AC current at 25 and 75°C for most standard aluminum conductors.

The calculated values include the frequency-dependent skin effect for all types of stranded conductor. However, it does not include a correction for current density dependent magnetic core effects, which is significant for ACSR conductors having an odd number of aluminum layers. The resistance of single-layer ACSR conductors is shown to be increased as much as 20%, and the resistance of three-layer ACSR may be as much as 3% higher than the tabulated values [48]. Engineering judgment is needed when using these conductors.

Electrical resistance is calculated solely as a function of conductor temperature using the calculated values at 25 and 75°C. The conductor resistance at any temperature,  $R(T_c)$ , is found with a linear interpolation or extrapolation using

$$R(T_c) = \left[ \frac{R(T_{high}) - R(T_{low})}{T_{high} - T_{low}} \right] (T_c - T_{low}) + R(T_{low}), \quad (3.6)$$

where  $T_{high}$  is the maximum conductor temperature where the resistance is specified,  $T_{low}$  is the minimum conductor temperature where the resistance is specified,  $R(T_{high})$  is the resistance at  $T_{high}$  and  $R(T_{low})$  is the resistance at  $T_{low}$ .

Resistivity of most common metals used in stranded conductors increases somewhat faster than linearly with temperature. Therefore, the resistance calculated using Equation 3.6 will be somewhat high, and thus conservative for rating calculations when the conductor temperature is between  $T_{low}$  and  $T_{high}$ . However, when the

conductor temperature exceeds  $T_{high}$ , the calculated resistance will be somewhat low, and thus non-conservative for rating calculations. For example, based upon measurements of individual 1350 H19 aluminum strand resistance at temperature of 175 and 500°C, give results approximately 1 and 5% higher values than calculated using Equation 3.6 with  $T_{low}$  and  $T_{high}$  of 25 and 75°C, respectively. The calculated and measured error of resistance between 25 and 75°C is negligible [48]. Therefore, the use of Equation 3.6 is adequate for the purpose of this study.

### Solar Heating

Conductor solar heating is caused by solar radiation from the sun. The magnitude of the solar heat gain depends on the geographical location, weather conditions, time of day, and time of year. The rate of solar heat gain,  $q_s$ , is defined as follows

$$q_s = \alpha Q_{se} \sin(\theta) A', \quad (3.7)$$

where  $\alpha$ ,  $Q_{se}$ , and  $A'$  are the solar absorptivity of the conductor, total corrected solar radiated heat flux, and the projected area of conductor per unit length, respectively. The angle,  $\theta$ , is given as

$$\theta = \arccos [\cos(H_c) \cos(Z_c - Z_L)], \quad (3.8)$$

where  $H_c$  is the solar altitude of the sun,  $Z_c$  is the azimuth of the sun, and  $Z_L$  is the azimuth of the conductor. The solar altitude of the sun and the solar declination are defined as follows, respectively

$$H_c = \arcsin [\cos(Lat) \cos(\delta) \cos(\omega) + \sin(Lat) \sin(\delta)], \quad (3.9)$$

$$\delta = 23.4583 \sin \left[ \frac{284 + N}{365} 360 \right], \quad (3.10)$$

where  $Lat$ ,  $\delta$ ,  $\omega$ , and  $N$  are the degrees of latitude, solar declination, hours from local sun noon times  $15^\circ$ , and the day of the year (January 21<sup>st</sup> = 21, February 12<sup>th</sup> = 43, etc.), respectively. The total corrected solar radiated heat flux is given by

$$Q_{se} = K_{solar} Q_s, \quad (3.11)$$

where  $K_{solar}$  and  $Q_s$  are the solar altitude correction factor and the total solar and sky radiated heat flux rate. The solar altitude correction factor is calculated by

$$Q_s = A + BH_c + CH_c^2 + DH_c^3 + EH_c^4 + FH_c^5 + GH_c^6, \quad (3.12)$$

where  $H_c$  is the solar altitude of the sun and the variable A–G are determined using Table 3.3.

The total heat flux elevation correction factor,  $K_{solar}$ , is given as

$$K_{solar} = A + BH_e + CH_e^2, \quad (3.13)$$

where  $H_e$  is the elevation above sea level. The variables A, B and C are given as 1.0,  $1.148 \times 10^{-4}$ , and  $-1.108 \times 10^{-8}$ , respectively. The solar azimuth,  $Z_c$ , is given as

$$Z_c = C + \arctan(\chi), \quad (3.14)$$

where the solar azimuth variable,  $\chi$ , is calculated using

Table 3.3: Atmosphere correction coefficients [48].

<b>Clear Atmosphere</b>	<b>Value</b>
A	-42.2391
B	63.8044
C	-1.9220
D	$3.46921 \times 10^{-2}$
E	$-3.61118 \times 10^{-4}$
F	$1.94318 \times 10^{-6}$
G	$-4.07608 \times 10^{-8}$
<b>Industrial Atmosphere</b>	<b>Value</b>
A	53.1821
B	14.2110
C	$6.6138 \times 10^{-1}$
D	$-3.1658 \times 10^{-2}$
E	$5.4654 \times 10^{-4}$
F	$-4.3446 \times 10^{-6}$
G	$1.3236 \times 10^{-8}$

$$\chi = \frac{\sin(\omega)}{\sin(Lat) \cos(\omega) - \cos(Lat) \tan(\delta)}. \quad (3.15)$$

The solar azimuth constant,  $C$ , is a function of the hour angle and the solar azimuth variable; it is determined using Table 3.4.

A pyronometer is a device that measures solar radiation and may be used to determine the real-time solar heating. However, on partly cloudy days, large spatial change in solar radiation can occur. Applying measured values over areas with no telemetry may lead to large over or under estimation of the actual solar heating value. The maximum real-time solar heating, using the above equations, is used in ampacity calculations throughout this report, and therefore should be considered conservative.

Table 3.4: Solar azimuth constant,  $C$ , as a function of hour angle,  $\omega$ , and solar azimuth variable,  $\chi$  [48].

Hour Angle	$\chi \geq 0$	$\chi < 0$
$-180 \leq \omega < 0$	0	180
$0 \leq \omega \leq 180$	180	360

### Convective Cooling

The convective heat loss is defined dependent on wind velocity. For zero, low, and high wind velocities convective heat loss,  $q_c$ , is defined as follows: for zero wind velocity or natural convection

$$q_{c_n} = 0.0205 \rho_f^{0.5} D^{0.75} (T_c - T_a)^{1.25}, \quad (3.16)$$

for low wind velocity

$$q_{c_1} = \left[ 1.01 + 0.0372 \left( \frac{D \rho_f V_w}{\mu_f} \right)^{0.52} \right] k_f K_{angle} (T_c - T_a), \quad (3.17)$$

and for high wind velocity

$$q_{c_2} = \left[ 0.0119 \left( \frac{D \rho_f V_w}{\mu_f} \right)^{0.6} k_f K_{angle} (T_c - T_a) \right]. \quad (3.18)$$

Here  $\rho_f$ ,  $\mu_f$ , and  $k_f$  are the air density, dynamic viscosity, and thermal conductivity of air, respectively. The convective cooling is determined by using the largest of the three convection equations. To take into account the wind direction, the convective heat loss rate is multiplied by the wind direction factor,  $K_{angle}$ , which is given by

$$K_{angle} = 1.194 - \cos(\phi) + 0.194 \cos(2\phi) + 0.368 \sin(2\phi), \quad (3.19)$$

where  $\phi$  is the angle between the wind direction and the conductor axis. For both forced and natural convection, air density, air viscosity, and coefficient of thermal conductivity of air are calculated using the film temperature,  $T_{film}$ . The film temperature is given as

$$T_{film} = \frac{T_c + T_a}{2}. \quad (3.20)$$

Dynamic viscosity of air, air density, and thermal conductivity of air are defined as follows, respectively

$$\mu_f = \frac{1.458 \times 10^{-6} (T_{film} + 273)^{1.5}}{T_{film} + 383.4}, \quad (3.21)$$

$$\rho_f = \frac{1.293 - 1.525 \times 10^{-4} H_e + 6.379 \times 10^{-9} H_e^2}{1 + 0.00367 \cdot T_{film}}, \quad (3.22)$$

$$k_f = 2.424 \times 10^{-2} + 7.477 \times 10^{-5} T_{film} - 4.407 \times 10^{-9} T_{film}^2. \quad (3.23)$$

### Radiative Cooling

Thermal radiation is the emission of electromagnetic waves generated by the thermal motion of charged particles in matter [49]. The radiative heat loss of a conductor is given as

$$q_r = 0.0178 D \varepsilon \left[ \left( \frac{T_c + 273}{100} \right)^4 - \left( \frac{T_a + 273}{100} \right)^4 \right], \quad (3.24)$$

where  $T_a$  is the ambient temperature,  $D$  is the conductor diameter,  $\varepsilon$  is the conductor emissivity, and  $\alpha$  is the conductor solar absorptivity. Depending on the conditions

of conductor, the absorptivity and emissivity constants range between 0.23–0.91 [48]. They are assumed to be 0.5 in this thesis.

### 3.3 Numerical Methods

The conductor temperature rate of change, given in Equation 3.4, is a differential equation. Differential equations are composed of an unknown function and its derivative(s). More specifically, it's a first order ODE. The conductor temperature is continually changing in response to electrical current and weather changes. ODEs of this form are termed initial value problems (IVPs); the general form is expressed as

$$\frac{dy}{dx} = f(t, y), \quad (3.25)$$

over a time interval

$$a \leq t \leq b,$$

subject to an initial condition

$$y(a) = y_o. \quad (3.26)$$

The general expression is solved conveniently using a time-marching method as follows

$$y_{i+1} = y_i + \phi h. \quad (3.27)$$

Here the slope estimate,  $\phi$ , is used to extrapolate from an old value,  $y_i$ , to a new value,  $y_{i+1}$ , over a time step size,  $h$ .

Numerical solutions of ODEs involve two types of error, truncation and round-off errors. Truncation or discretization errors are caused by the techniques employed to

approximate values of  $y$ . Truncation errors are composed of two parts: the single step or local truncation error, and a propagated truncation error, which occurs on successive steps. The sum of truncation error is the total or global truncation error. Round-off error is caused by the limited numbers of significant digits a computer can retain.

Insight into the magnitude and properties of the truncation error can be gained by deriving numerical methods directly from the Taylor series expansion. The Taylor series expansion about a starting value  $(t_i, y_i)$  is given as

$$y_{i+1} = y_i + f(t_i, y_i)h + \frac{f'(t_i, y_i)}{2!}h^2 + \cdots + \frac{f^{n-1}(t_i, y_i)}{n!}h^n + O(h^{n+1}), \quad (3.28)$$

where  $n$  is the order of the solution method and  $O(h^{n+1})$  is the local truncation error, it is proportional to the step size raised to the  $(n + 1)$  power. The truncation error occurs because the true solution is approximated by using a finite number of terms in the Taylor series.

### 3.3.1 Euler Method

The simplest method for solving an ODE is Euler's method. It is a first order method, where the slope at the beginning of the time interval is taken as an approximation of the slope over the entire interval. Starting with the general form of an initial value problem, the first derivative provides a direct estimate of the slope,  $\phi$ , at the initial time,  $t_i$ , given as

$$\phi = f(t_i, y_i). \quad (3.29)$$

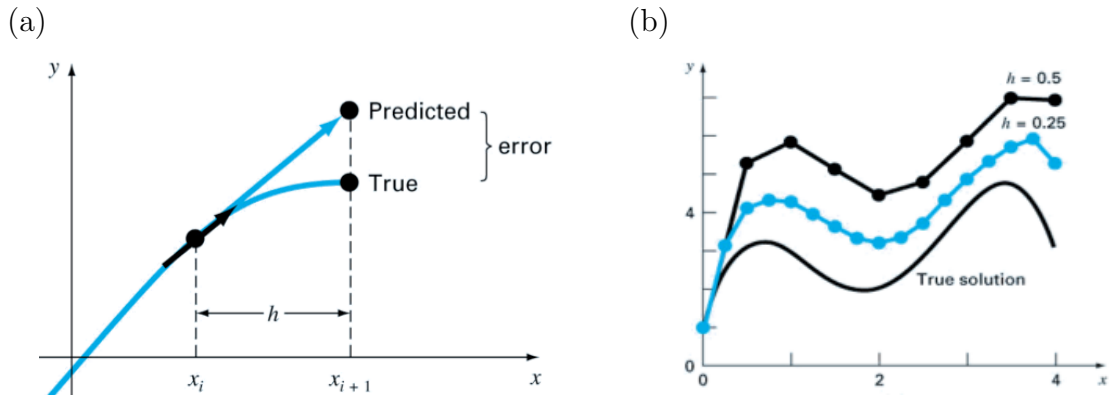


Figure 3.4: (a) The local truncation error over a single time step, denoted by  $h$ . (b) Reducing the size of the time step results in a better estimation of the true solution. Illustration adopted from [18].

Here  $f(t_i, y_i)$  is the differential equation evaluated at  $t_i$  and  $y_i$ , the initial value. Substituting this into Equation 3.27, gives the form

$$y_{i+1} = y_i + f(t_i, y_i)h, \quad (3.30)$$

and is known as a forward Euler method.

Figure 3.4 explains the Euler method graphically. Here (a) shows the local truncation error over a single time step, while the global truncation error can be seen over multiple steps in (b). It can be seen that reducing the step size reduces the truncation error, resulting in a better estimation of the true solution.

### 3.3.2 Runge-Kutta Method

Euler's method was derived using the first two terms of the Taylor Series. Larger numbers of terms can be used for better approximations. Higher order approximations are generally not practical because the partial derivatives of  $f(t, y)$  need to be determined analytically and can become very complicated [60]. However, Runge-Kutta

(RK) methods achieve higher order accuracy without requiring the calculation of higher derivatives. A full derivation of the RK method can be found in [18]; the general form is given as

$$y_{i+1} = y_i + \phi(t_i, y_i, h)h, \quad (3.31)$$

where  $\phi(t_i, y_i, h)$  is called the increment function, which is a representative slope over the interval  $h$ . The increment function's general form is

$$\phi = a_1k_1 + a_2k_2 + \cdots + a_nk_n, \quad (3.32)$$

where the  $a$ 's are constants and the  $k$ 's are defined as

$$k_1 = f(t_i, y_i), \quad (3.33)$$

$$k_2 = f(t_i + p_1h, q_{11}k_1h), \quad (3.34)$$

$$k_3 = f(t_i + p_2h, y_i + q_{21}k_1h + q_{22}k_2h), \quad (3.35)$$

⋮

$$k_n = f(x_i + p_{n-1}h, y_i + q_{n-1,1}k_1h + q_{n-1,2}k_2h + \cdots + q_{n-1,n-1}k_{n-1}h). \quad (3.36)$$

Values for the  $a$ 's,  $p$ 's and  $q$ 's are evaluated by setting the increment function equal to terms in the Taylor series expansion. The  $k$ 's are reoccurring,  $k_1$  appears in the equation for  $k_2$ , which appears in the equation for  $k_3$ , and so on. Unlike higher

order Taylor series expansion methods, this recurrence makes RK methods especially efficient for computer calculations.

Various types of RK methods can be devised by employing a different number of terms in the increment function, specified by  $n$ . For a second and fourth order RK, the increment function will have two and four terms, respectively. RK methods have an infinite number of variations. There is one less equation than unknowns when solving the  $a$ 's,  $p$ 's and  $q$ 's, an assumption of a value must be selected for one of the unknowns. Three of the most popular second order RK methods, the midpoint, Heun, and Ralston's, are given respectively,

$$y_{i+1} = y_i + k_2 h, \quad (3.37)$$

$$y_{i+1} = y_i + \left( \frac{1}{2} k_1 + \frac{1}{2} k_2 \right) h, \quad (3.38)$$

$$y_{i+1} = y_i + \left( \frac{1}{3} k_1 + \frac{2}{3} k_2 \right) h. \quad (3.39)$$

The most commonly used fourth order RK method is given as

$$y_{i+1} = y_i + \frac{1}{6} (k_1 + 2k_2 + 2k_3 + k_4) h. \quad (3.40)$$

Here the  $k$ 's represent a slope given as

$$k_1 = f(t_i, y_i), \quad (3.41)$$

$$k_2 = f \left( t_i + \frac{1}{2}h, y_i + \frac{1}{2}k_1h \right), \quad (3.42)$$

$$k_3 = f \left( t_i + \frac{1}{2}h, y_i + \frac{1}{2}k_2h \right), \quad (3.43)$$

$$k_4 = f (t_i + h, y_i + k_3h). \quad (3.44)$$

The multiple estimates of the slope are developed in order to come up with an improved average slope over the time step interval. In this thesis work, a 4<sup>th</sup> order Runge-Kutta method is used to solve the IEEE ODE that governs the transient temperature change of conductor. This is done using MATLABs built-in ode45 solver [59].

### 3.4 Structure of the Atmospheric Boundary Layer

The troposphere is the lowest layer of the earth’s atmosphere. Its height is roughly 7 and 20 kilometers at the poles and equator, respectively. It can be divided in two parts, the atmospheric boundary layer (ABL) that extends 1–2 kilometers up from the surface occupying 10–20% of the troposphere and the free atmosphere [96]. The ABL is characterized by its behavior being directly influenced by the Earth’s surface. It is the region most directly influenced by the exchange of momentum, heat, and water vapor [53]. The most dramatic temperature changes occur within the ABL.

The study of the ABL belongs to the fields of fluid mechanics and thermodynamics. In classical fluid mechanics, boundary layers are described as the layer between the surface and the free stream flow, where the velocity is less than 99% of the free stream velocity [64]. However, Stull [88] defines the ABL as “the part of the troposphere that

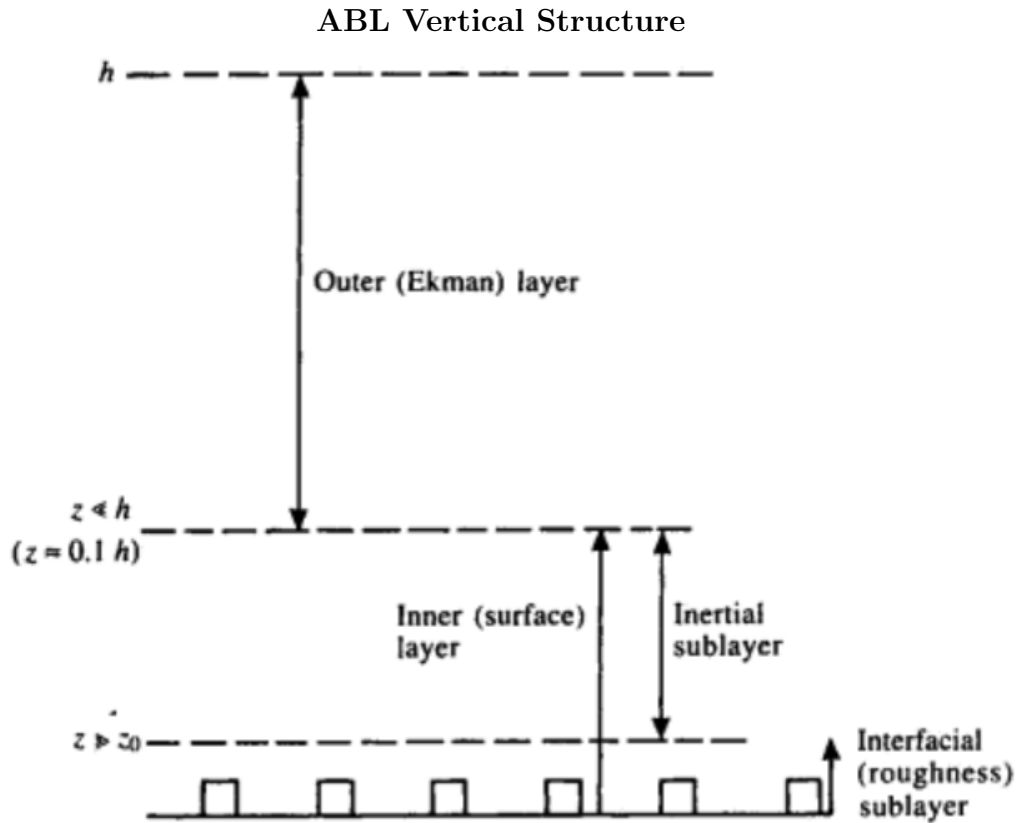


Figure 3.5: Schematic of the vertical sublayer structure in the atmospheric boundary layer. In this diagram,  $h$  is the boundary layer depth,  $z$  is height, and  $z_0$  is the aerodynamic roughness length [40].

is directly influenced by the presence of the Earth’s surface, and responds to surface forcing with a time scale of about an hour or less.” The ABL is vertically divided into two sublayers, the sublayer height depends upon the rate at which shearing stress vary. The lower layer is the inner Prandtl or surface layer and the outer layer is the Ekman or transition layer. At the bottom of the surface layer, a roughness sublayer is present that is influenced by physical characteristics of the surface. Figure 3.5 illustrates the vertical structure within the ABL.

The free atmosphere resides above the atmospheric boundary layer. Here viscous

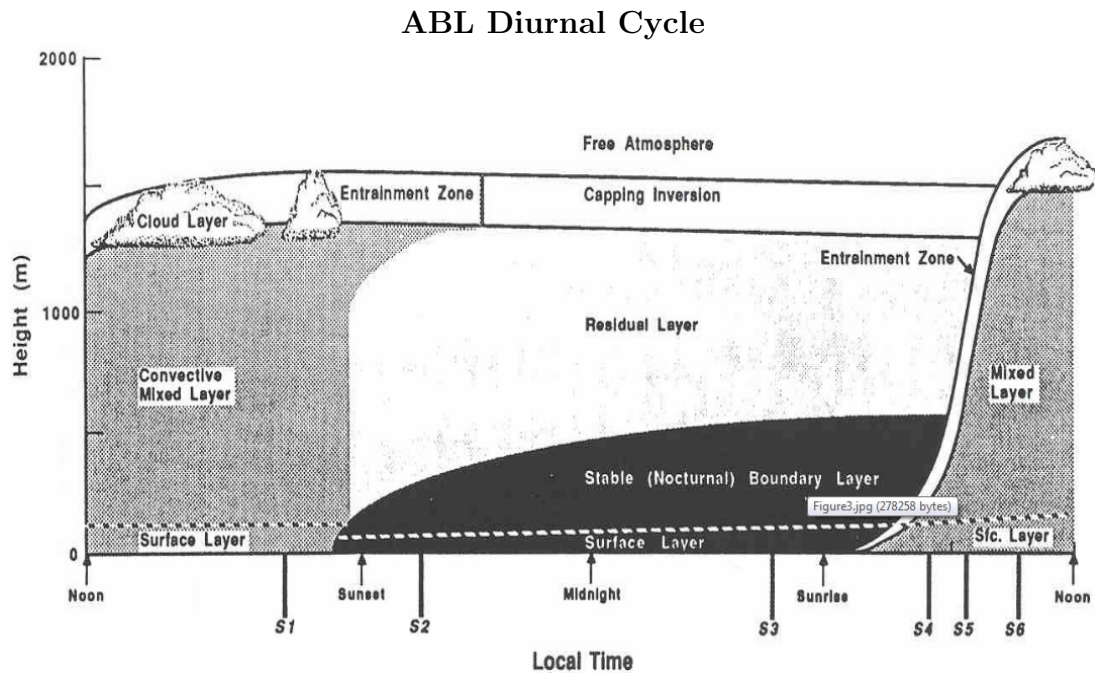


Figure 3.6: Vertical cross-section of the atmospheric boundary layer structure and its typical evolution over land under fair weather, cloud free conditions. Heating from below sets to a convective very turbulent mixing layer during the day, while at night a less turbulent residual layer containing former mixed layer air and a nocturnal stable boundary layer of sporadic turbulence (dark region). Illustration adopted from Stull [88].

stresses are regarded as negligible and it responds very slowly to surface events. There is a buffer region between the free atmosphere and the boundary layer, termed the entrainment zone. Entrainment occurs when air from a non-turbulent free atmosphere is drawn into an adjacent turbulent region. Figure 3.6 shows how the sublayers of the ABL evolve throughout a typical cloud free diurnal (daily) cycle.

The dynamical structure of the ABL is almost always under vertical mixing or turbulence. Turbulence refers to the vertical redistribution of three key elements in the atmosphere: momentum, mass, and heat. It consists of complex superposition of many different scales of motion or swirls called eddies that interact nonlinearly in

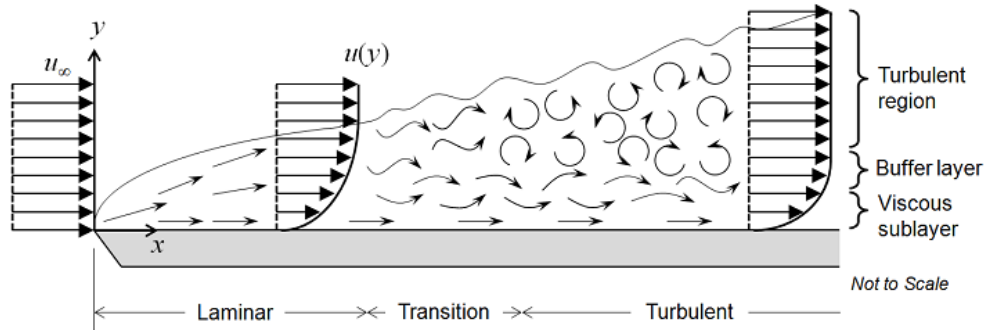


Figure 3.7: Flow over a flat plate. Illustration adopted from [22].

chaotic motions. Turbulence in the ABL differs from that studied in wind tunnels. Unlike wind tunnels, turbulence associated with thermal or convective mixing coexists with mechanical turbulence [40].

### 3.4.1 ABL Mechanical Turbulence

Mechanical turbulence results from wind shear due to viscous effects of the fluid. The magnitude of mechanical turbulence depends on the wind speed, roughness of the terrain, and stability of the air. Flow over a smooth flat plate is the most common and basic way to study mechanical turbulence. The boundary layer forms downstream from the leading edge of the plate, extending up where the velocity is 99% of the free stream velocity [64]. The no-slip surface condition and viscous forces generate shear stress turbulence. Initially the flow over a flat plate is laminar, but after covering some distance, fully turbulent flow is developed, illustrated in Figure 3.7.

Eddies in turbulent flow are evanescent and quickly disappear, being replaced by a succession of different eddies. However, the turbulent motion is not completely random, it is quasi-random [96]. Flow over an ideal smooth flat plate is great for academic interest, however, in practice mechanical turbulence is greatly affected

by the surface roughness and the physical terrain. Rough flow occurs when the shear stress is dominated by the drag of the roughness elements, and in smooth flow shear stress is dominated by viscosity [73]. A better model for atmospheric flow is a rough wall boundary layer, where both smooth wall shear and fixed objects generate mechanical turbulence.

Turbulent wake structures occur when wind flows over or around large terrain and obstructions. More and more wind turbines are being built away from flat regions in complex terrain. Elevated positions like hill tops are favorable sites due to the increased wind velocity. In complex terrain, wake turbulence may occur behind structures and rapid changing terrain. Flow over a two-dimensional ridge is an example of wake turbulence and is shown in Figure 3.8. There is an elevated wind velocity over the crest of the ridge, separation on the downwind slope where flow reverses direction, and a highly turbulent wake region follows.

The CFD simulations completed in this thesis are in a region of moderately complex terrain. Because of the turbulent effects that occur in these regions, it's necessary to use a computational mesh and turbulent model that can adequately resolve the turbulent flow characteristics that occur.

### **3.4.2 ABL Convective Turbulence**

Wind flow patterns emerge from horizontal surface and atmospheric temperature contrasts on all spatial scales, from global to local size [34]. The atmosphere is largely transparent to the sun's electromagnetic radiation [6]. The radiation reaches the Earth's surface, where it is absorbed, warming the surface. The absorption of solar energy is the driving force behind the wind. Thermal or convective turbulence consists of plumes or thermals of warm air that rises, and cold air that sinks due

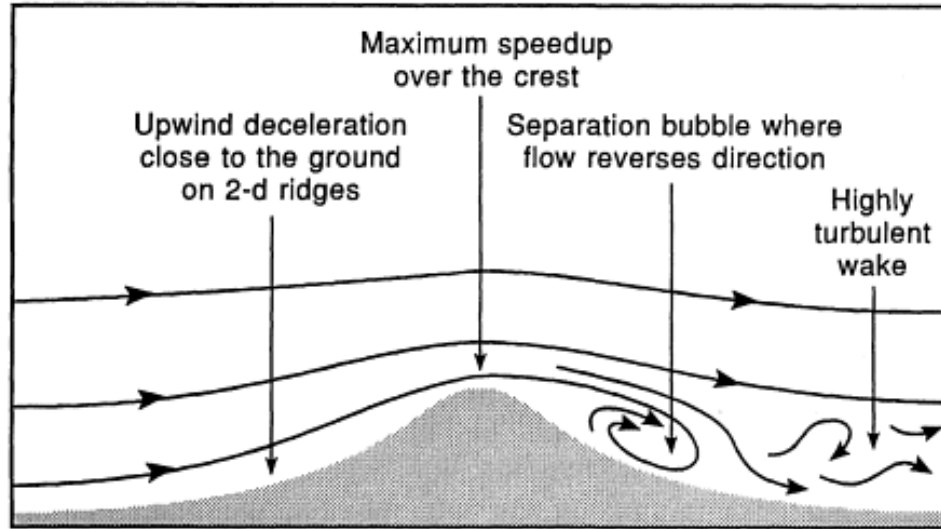


Figure 3.8: Flow over a two-dimensional ridge showing formation of an increased velocity over the crest and a separation bubble when the downwind slope is steep enough [53].

to buoyancy forces. Two principal types of thermal stability can be distinguished. If heating from below dominates, there is a convective or unstable ABL with high turbulence. If cooled from below, a stable boundary layer with low turbulence will exist.

Earth's surface is heated differently according to latitude, season, and surface properties. The uneven surface heating heats the layer of air nearest the ground at different rates, causing horizontal heat gradients. The vertical distance between two given levels of constant pressure depends on air temperature [34]. Warm air is less dense and has a larger vertical distance between two given pressure surfaces than colder air. Mathematically this is described by the hydrostatic equation, given as

$$\frac{\partial p}{\partial z} = -\rho g, \quad (3.45)$$

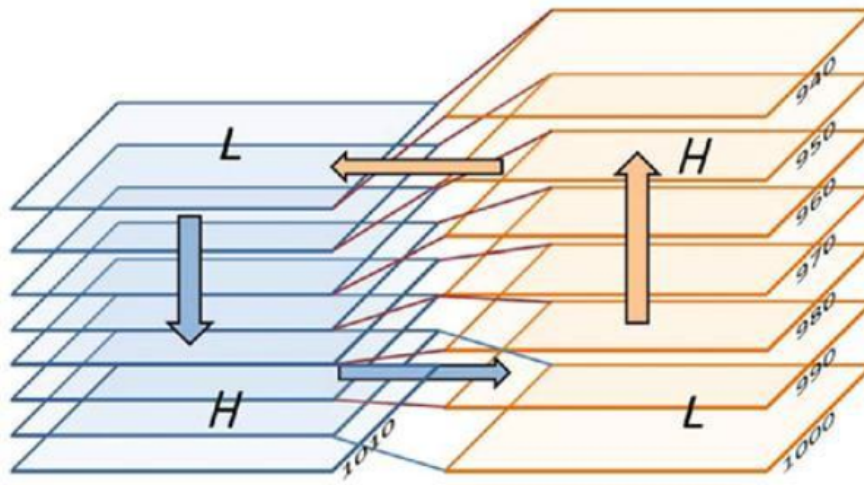


Figure 3.9: Vertical pressure gradients in warmer (right) and colder (left) air. Planes symbolize constant pressure levels. Numbers give air pressure in hPa. Capital letters indicate high (H) and low (L) pressure at the surface (lower letters) and on constant height surfaces aloft (upper letters). Arrows indicate a thermally directed circulation. Illustration adapted from Emeis [34].

where  $p$  is air pressure,  $z$  is the vertical coordinate,  $g$  is gravity, and  $\rho$  is air density. Assuming a constant surface pressure, this will result in horizontal pressure gradients. These pressure gradients produce compensating winds, blowing from higher pressure towards lower pressure to remove them. In reality, there isn't a constant surface pressure and a small pressure sink occurs in warmer regions; this is illustrated in Figure 3.9.

This is observed on a global scale, in the Hadley cell, warm air near the equator rises moving towards the poles aloft and descends in the subtropics. At the polar cell, cold air sinks and rises at higher latitudes. These cells meet in a region called the Ferrel cell, characterized by the rising colder of the Polar cell and the sinking warmer air from the Hadley cell. These global cells create global winds, such as the trade winds in the Hadley cell [34].

There are local wind systems that do not emerge from large global scale temperature differences, but from local temperature differences. Local wind systems, much like global systems, often exhibit a large regularity of daily and seasonal wind and weather cycles [26]. This regularity is attributed to the local terrain and surface properties.

### 3.4.3 ABL Surface Layer

The surface layer represents the bottom 10% of the ABL and is of particular importance in this study because it's where transmission lines and wind turbines reside. During the day, high convective turbulence can push the surface layer to heights of  $\sim 200$  meters. At night, when convective turbulence dies, the top of the surface layer drops to  $\sim 100$  meters [34, 88] and under strong stable conditions it can be even lower. The surface layer is defined meteorologically as the layer where the turbulent vertical fluxes of momentum, heat and moisture deviate less than 10% from their surface values, and the influence of the Coriolis force is negligible [34]. The most important features of the surface layer is the highly turbulent flow where viscous forces dominate and the wind speed increases strongly with height. A logarithmic wind profile or power-law are often used to extrapolate the wind velocity, they are only valid in the surface layer. The logarithmic wind profile is given as

$$\bar{u}(z) = \frac{u_*}{k} \left[ \ln \left( \frac{z}{z_0} \right) + \psi(z, z_0, L) \right], \quad (3.46)$$

where  $\bar{u}$  is the horizontal wind speed,  $u_*$  is the friction velocity,  $k$  is the von Karman constant,  $z$  is the elevation,  $z_0$  is the roughness length, and  $\psi$  is a stability term where  $L$  is the Monin-Obukhov stability parameter. Under neutral stability conditions, the

stability term is equal to zero and drops out. The logarithmic wind profile is derived from physical and dimensional arguments. However, the power-law can be convenient to use; it is found empirically and is given as

$$\bar{u}(z) = u(z_r) \left( \frac{z}{z_r} \right)^\alpha, \quad (3.47)$$

where  $z_r$  is a reference height and  $\alpha$  is the power law exponent. The power law exponent depends on the surface roughness and the thermal stability.

### **ABL Roughness Sublayer**

At the bottom of the surface layer, a roughness sublayer exists, referred to as the micro-layer. The micro-layer can be considered as the region influenced directly by the elements; it's where molecular diffusion is an important process by which heat and mass are exchanged between the surface and the air [40]. The top of the micro-layer is the roughness length ( $z_o$ ), the height above the ground where wind speed is theoretically zero [40, 88]. In reality, wind in the micro-layer is not zero, it no longer follows the mathematical logarithm velocity profile. The roughness layer depth is affected by surface topography and physical features. It's not a physical length; it's a length scale that represents the roughness of the surface. Estimates of the roughness length are usually determined from observations of the wind profile, preferably in neutral conditions [40].

#### **3.4.4 ABL Ekman Layer**

The Ekman layer is the upper 90% of the atmospheric boundary layer. Here, unlike the surface layer, the rotational Coriolis force becomes important, causing a

turning of the wind direction with height. It's the layer where the flow is a result of the pressure gradient, Coriolis, and turbulent drag forces. In the outer region, the flow shows little dependence on the physical terrain of the surface.

### 3.5 Numerical Wind Modeling and Prediction

Linear wind flow models such as WAsP [32] (Wind Analysis and Application Program) are widely used to predict the spatial variation of the average wind speed, directional frequency, wind shear, and other boundary layer characteristics. Linear models gained wide use in the 1980s due to the simple turbulence and surface roughness models requiring limited computing resources. They run fast while performing reasonably well where the wind is not significantly affected by nonlinear phenomena. The WAsP model is best suited for simple geometries and is known to poorly predict flow separation and recirculation [17]. Its strength is in simple regions. Transmission lines and wind farms are now being placed in complex terrain where linear models have been pushed past their limitations [70].

Computational fluid dynamic (CFD) models solve the complex Navier-Stokes (NS) equations that govern the physical phenomena of fluid flow as well as heat transfer. They are derived from Newton's second law with the assumption that fluid stress is the sum of a diffusing viscous term plus a pressure term. Solutions to the NS equations give a velocity or flow field, which describes the velocity of the fluid at a given point in space and time. The general form of the NS equations is given as

$$\rho \left( \frac{\partial v}{\partial t} + v \cdot \nabla v \right) = -\nabla p + \nabla \cdot \mathbb{T} + f, \quad (3.48)$$

where  $v$  is the flow velocity,  $\rho$  is the fluid density,  $p$  is the pressure,  $\mathbb{T}$  is the deviatoric

stress tensor, and  $f$  represents body forces. The NS equations are a statement of the conservation of momentum. Momentum is a vector quantity, therefore Equation 3.48 yields three independent equations.

In order to fully describe fluid flow, more information is needed. This may include the conservation of mass, the conservation of energy, and an equation of state, when compressibility effects are dominant. The conservation of mass is governed by the mass continuity equation, the general form given as

$$\frac{\partial \rho}{\partial t} + \nabla \cdot (\rho v) = 0. \quad (3.49)$$

The NS equations are highly non-linear partial differential equations, analytical solutions are only available for simple configurations, and numerical methods are often needed to solve. Anderson [52] refers to CFD as “the art of replacing the integrals or the partial derivatives in these equations with discretized algebraic forms, which in turn are solved to obtain numbers for the flow field values at discrete points in time and/or space.” CFD models perform well and give a high level of detail in turbulent flow. To perform a CFD calculation, a control volume is first created, a computational mesh is constructed inside the control volume, boundary conditions are set, physical models are chosen, and the governing equations are solved using numerical methods. ANSYS FLUENT applies the finite volume method, background and derivation are available from numerous sources; the reader is referred to Versteeg and Malalasekera [94] for a complete discussion.

The idea of numerical weather prediction (NWP) is to sample the state of the atmosphere and use fluid dynamic and thermodynamic equations to estimate the state of the atmosphere at some time in the future. NWP models like WRF (Weather

Research and Forecasting) solves the complex mathematical models for wind velocity, temperature, pressure, and moisture using meso-scale initial conditions provided by weather services [84]. Meso-scale is on the order of 1 km to 100 km horizontal spatial resolution. In principle, fully compressible, non-hydrostatic NWP models can simulate and capture a broad range of meteorological phenomena from synoptic to micro-scales. The micro-scale is the scale applicable to wind turbines and transmission lines where the spatial resolution can be below 2 km [77]. The challenge to a modeler is then to transfer weather information from the meso-scale to the micro-scale. The computational turnaround time can be long and increases rapidly with the number of computational points in a domain. Several NWP models exist and improvements in wind forecasting is the subject of several research projects in recent years [14, 65, 84].

### 3.6 Turbulence Modeling

Turbulence is characterized by fluctuations in velocity and thus transport quantities. Three CFD numerical approaches are used in turbulence modeling. Time-dependent solutions of the NS equations that set out to resolve the smallest scales of turbulent motion directly are termed direct numerical simulation (DNS). These simulations are not feasible for practical applications due to prohibitively large computational resource requirements. The velocity fluctuations in many practical applications are small scale and high frequency, as depicted in Figure 3.10. Therefore, to circumvent computational complexity, two alternative methods are often used. Turbulent flows can be averaged over reasonably short time intervals, resulting in a modified set of equations requiring less computational power. This approach is known as the Reynolds-averaged Navier-Stokes (RANS). The other method is a

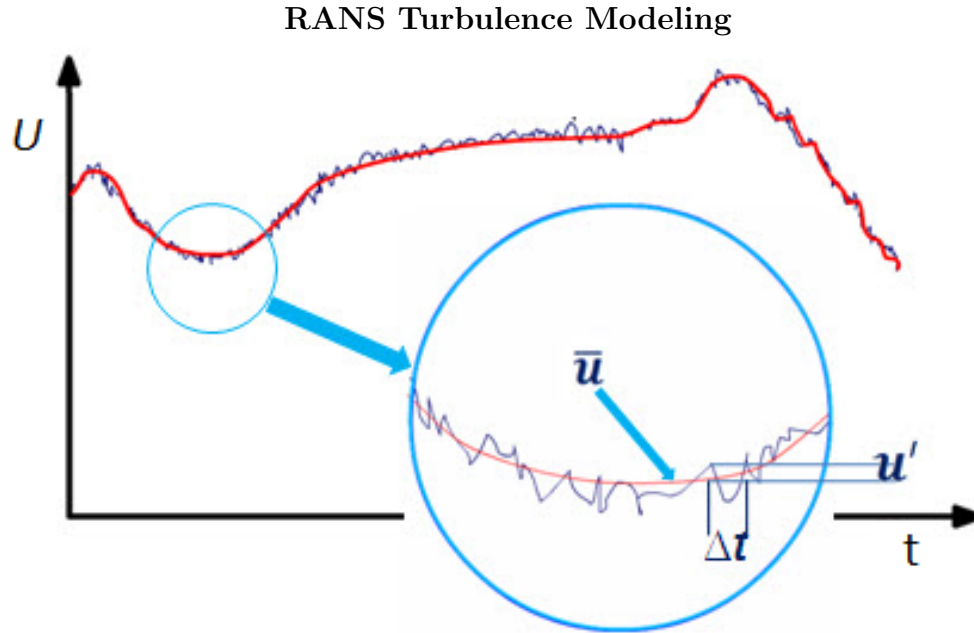


Figure 3.10: Turbulent flow velocity fluctuations and time averaged velocity using RANS approach. Illustration adopted from [35].

eddy resolving simulation, which uses a filtering approach, referred to as large-eddy simulations (LES). The CFD simulations completed over moderately complex terrain in this thesis employ a hybrid RANS-LES approach as described in Senocak et al. [78].

### 3.6.1 Reynolds-averaged Navier-Stokes Equations

RANS equations govern the transport of the averaged flow quantities where all scales of turbulence are modeled, greatly reducing the required computational efforts. RANS is economical in terms of computational expense, thus it is used for practical engineering problems and industry applications [10, 94]. The Reynolds stress is the component of the total stress tensor in a fluid obtained from the ensemble averaging operation over the NS equations to account for turbulent fluctuations in fluid momentum. For an incompressible homogeneous fluid flow, the velocities are

split into mean and fluctuating terms. The time averaged velocity,  $u(t)$ , is given as

$$u(t) = \bar{u} + u', \quad (3.50)$$

where  $\bar{u}$  is the average velocity and  $u'$  is the velocity fluctuations. Here, the average velocity is found using

$$\bar{u} = \frac{1}{\Delta t} \int_t^{t+\Delta t} u dt. \quad (3.51)$$

Likewise, the pressure and other scalar quantities are also decomposed into mean and fluctuating components. The time averaged variables are substituted back into the instantaneous NS equations. The continuity and momentum equations now take the form

$$\frac{\partial \rho}{\partial t} + \frac{\partial}{\partial x_i} (\rho \bar{u}_i) = 0, \quad (3.52)$$

and

$$\begin{aligned} \frac{\partial}{\partial t} (\rho \bar{u}_i) + \frac{\partial}{\partial x_j} (\rho \bar{u}_i \bar{u}_j) = \\ -\frac{\partial \bar{p}}{\partial x_i} + \frac{\partial}{\partial x_j} \left[ \mu \left( \frac{\partial \bar{u}_i}{\partial x_j} + \frac{\partial \bar{u}_j}{\partial x_i} - \frac{2}{3} \delta_{ij} \frac{\partial \bar{u}_l}{\partial x_l} \right) \right] + \frac{\partial}{\partial x_j} (-\overline{\rho u'_i u'_j}). \end{aligned} \quad (3.53)$$

These are the RANS equations. The convective acceleration, known as the Reynolds stresses,  $-\overline{\rho u'_i u'_j}$ , is a non-linear term and must be modeled to close the momentum equation.

### 3.6.2 Large-eddy Simulation Technique

The fundamental idea behind LES is to separate the flow into large and small scales using a mathematical filter [56, 75]. The large-scale turbulence is resolved, while small-scale turbulence which exhibit a more universal behavior being nearly isotropic [94], are treated as statistically universal and modeled. The small scales are referred to as subgrid-scales (SGS), their length scales are smaller than the filter used. LES equations result from filtering the time-dependent NS equations, the filtered form is given as

$$\frac{\partial \bar{u}_j}{\partial x_j} = 0, \quad (3.54)$$

$$\frac{\partial \bar{u}_i}{\partial t} + \frac{\partial}{\partial x_j} (\bar{u}_i \bar{u}_j) = -\frac{1}{\rho} \frac{\partial \bar{p}}{\partial x_i} + \frac{\partial}{\partial x_j} (2\nu \bar{S}_{ij} - \tau_{ij}), \quad (3.55)$$

where

$$S_{ij} = \frac{1}{2} \left( \frac{\partial \bar{u}_i}{\partial x_j} + \frac{\partial \bar{u}_j}{\partial x_i} \right) \quad (3.56)$$

is the deformation tensor, and

$$\tau_{ij} = \overline{u_i u_j} - \bar{u}_i \bar{u}_j \quad (3.57)$$

is the tensor representing the interaction of the SGS on the resolved large scales. The over-bar in these equations represents a filtered quantity. LES provides more details on the turbulent flow field than a RANS method does, however several challenges face LES. The replacement of SGS eddies with a model introduces errors in the simulation [75]. Resolving near-wall boundary layers requires significant computa-

tional resources, particularly at high Reynolds numbers [72]. Another challenge is the specification of inflow boundary conditions that have the proper turbulence spectra to sustain a turbulent flow field [55].

### 3.6.3 Turbulence Closure Problem

Through the process of averaging the governing equations by decomposing the flow into its mean and fluctuating components, additional unknowns have been introduced without any new additional equations. Therefore, three governing equations no longer constitute a closed set; this is referred to as the “turbulence closure problem.” The additional terms are introduced in both RANS and LES numerical approaches.

Early turbulence models were simply correlations of experimental results. This limited simulations to the flows used generating the models. To date, no single turbulence model can be considered universal for turbulent flow, and therefore must be chosen dependent on the flow scenario. Many turbulence models are available, each have strengths and weaknesses in different flow scenarios. Therefore, careful consideration needs to be taken when choosing the closure model employed in CFD simulation. Today, more general methods have been adopted that are based on conservation equations. Unfortunately, all models presently used in practical engineering applications reduce to correlations with experimental data at some level. By incorporating physics as much as possible into the models, it is hoped they will have applicability to a wider range of problems.

### 3.7 Standard k- $\epsilon$ Turbulent Closure Model

One of the most frequently used turbulence models is the k- $\epsilon$  model. It is a two equation turbulence model allowing the determination of both a turbulent length and time scale by solving two transport equations [10]. The standard k- $\epsilon$  model is a semi-empirical model based on modeling transport equations for the turbulent kinetic energy,  $k$ , and its dissipation rate,  $\epsilon$ . The turbulent kinetic energy is derived from the exact solution, while the dissipation rate is obtained using physical reasoning. In its derivation, the assumption is made that the flow is fully turbulent, where viscous effects are negligible. Therefore, the model is only valid in regions where fully turbulent flow exist. The turbulent kinetic energy and dissipation rate are obtained from the following transport equations

$$\frac{\partial}{\partial t}(\rho k) + \frac{\partial}{\partial x_i}(\rho k u_i) = \frac{\partial}{\partial x_j} \left[ \left( \mu + \frac{\mu_t}{\sigma_k} \right) \frac{\partial k}{\partial x_j} \right] + G_k + G_b - \rho \epsilon - Y_M + S_k, \quad (3.58)$$

and

$$\frac{\partial}{\partial t}(\rho \epsilon) + \frac{\partial}{\partial x_i}(\rho \epsilon u_i) = \frac{\partial}{\partial x_j} \left[ \left( \mu + \frac{\mu_t}{\sigma_\epsilon} \right) \frac{\partial \epsilon}{\partial x_j} \right] + C_{1\epsilon} \frac{\epsilon}{k} (G_k + C_{3\epsilon} G_b) - C_{2\epsilon} \rho \frac{\epsilon^2}{k} + S_\epsilon. \quad (3.59)$$

Here  $G_k$ ,  $G_b$ , and  $Y_M$  represent the generation of turbulent kinetic energy due to mean velocity gradients, generation of turbulent kinetic energy due to buoyancy, and fluctuation dilatation in compressible turbulence to the overall dissipation rate, respectively. Additionally,  $\sigma_k$  and  $\sigma_\epsilon$  are turbulent Prandlt numbers for  $k$  and  $\epsilon$ , respectively.  $S_k$  and  $S_\epsilon$  are user-defined source terms and  $C_{1\epsilon}$ ,  $C_{2\epsilon}$ , and  $C_{3\epsilon}$  are

constants.

In this study, CFD simulations over complex terrain use a hybrid RANS/LES technique. RANS models the contribution of the near-wall eddies and acts as a sort of wall model for the LES. The method chosen for simulation is the smooth length scale transition suggested by Senocak et al. [78], given as

$$\nu_t = \left[ \left( 1 - \exp\left(\frac{-z}{h}\right) \right)^2 (C_S \Delta)^2 + \exp\left(\frac{-z}{h}\right)^2 (\kappa z)^2 \right] |S|, \quad (3.60)$$

where  $\kappa$  is the von Kármán constant,  $C_S$  is the dynamic coefficient, and  $h$  is the transition height from RANS to LES. Equation 3.60 blends the length scales produced from the dynamic SGS model with a mixing length RANS model. The logarithmic reconstruction in the immersed boundary method (IBM) maintains consistency with the mixing length turbulence model. The transition height is determined by the following relationship based on the Nyquist theorem,

$$\gamma = \frac{h}{2\Delta}, \quad (3.61)$$

where  $\Delta$  is the base filter width and  $\gamma$  is a parameter chosen depending on the flow. The value of  $\gamma$  dictates how many cells near the wall are modeled by RANS. Ensuring that  $h$  is large enough to encompass at least one full cell is of the utmost importance.

## CHAPTER 4

### IEEE STANDARD 738 VALIDATION

Two frequently used standards for determining overhead conductor thermal conditions are IEEE Standard 738 [48] and CIGRE [20], minor differences between the two methods exist [86]. The IEEE Standard 738 was first published in 1986, revised in 1993, and the current version was revised in 1996. Bontempi et al. [16] suggested that convective heat transfer correlations used in the IEEE standard can be improved.

Therefore, to instill additional confidence into the DLR concept, this chapter is devoted to validation of the convection cooling term in the IEEE standard using ANSYS FLUENT. FLUENT is one of the most widely used CFD packages in industry. It contains the broad physical modeling capabilities needed to model fluid flow, turbulence, and heat transfer. Resulting CFD simulations are compared with steady-state and transient conductor temperature equations available in the IEEE standard.

#### 4.1 Computational Setup for the Heated Conductor Analysis

Individual aluminum and steel wires that comprise Starling 26/7 ACSR conductor are modeled as two concentric cylinders, shown in Figure 4.7. Three high quality 2D structured meshes consisting of 23,820 nodes were created with ICEMCFD. The mesh quality has a minimum value of 0.802 and maximum of 1.0, with  $\sim 98\%$  of the cells

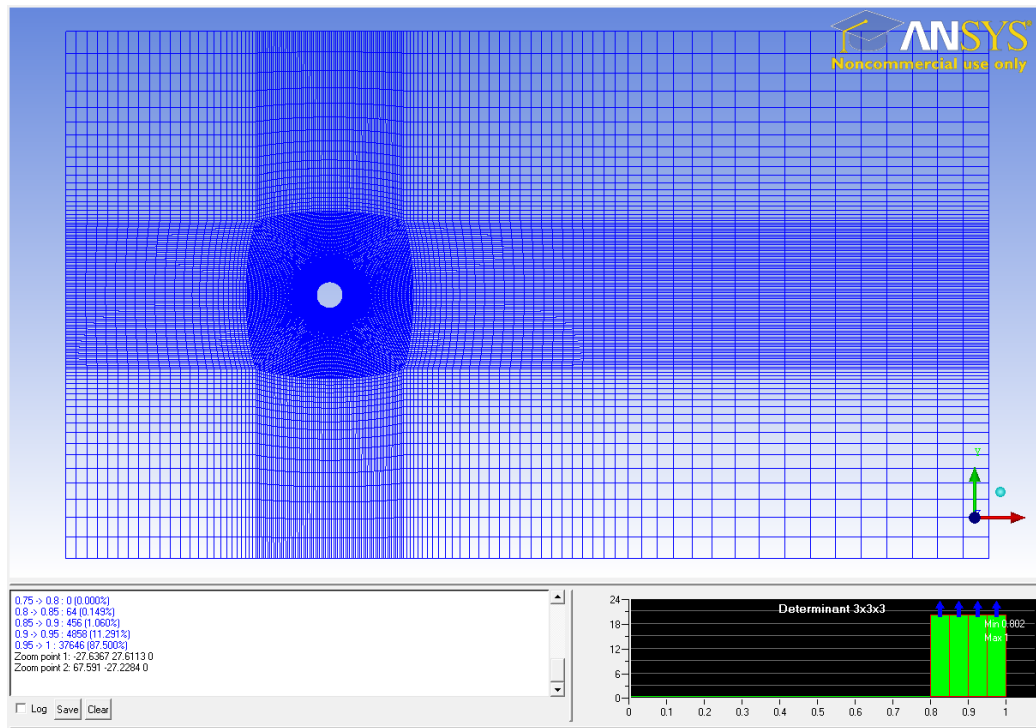


Figure 4.1: Computational mesh generated using ICEMCFD. The conductor has been suppressed, only showing the fluid domain for visualization. The mesh quality has a minimum of 0.802 and maximum of 1, and  $\sim 98\%$  of the cells having a quality  $> 0.9$ .

have a quality  $> 0.9$ . The mesh quality is defined as the relative determinant: it's the ratio of the smallest determinant of the Jacobian matrix divided by the largest determinant of the Jacobian matrix, where each determinant is computed at each node of the element. A determinant value of 1.0 would indicate a perfectly regular mesh element and 0 would indicate an element degenerate in one or more edges [9].

The three individual meshes consisted of the same number of cells, only the size of the cell-adjacent to the conductor was changed, allowing the wall-adjacent cell center to lie in the log-law layer under different inlet velocity conditions. Figure 4.1 shows the mesh of the fluid domain with the conductor domain suppressed for clarity. A view of the computational mesh near the conductor, with small cells-adjacent size,

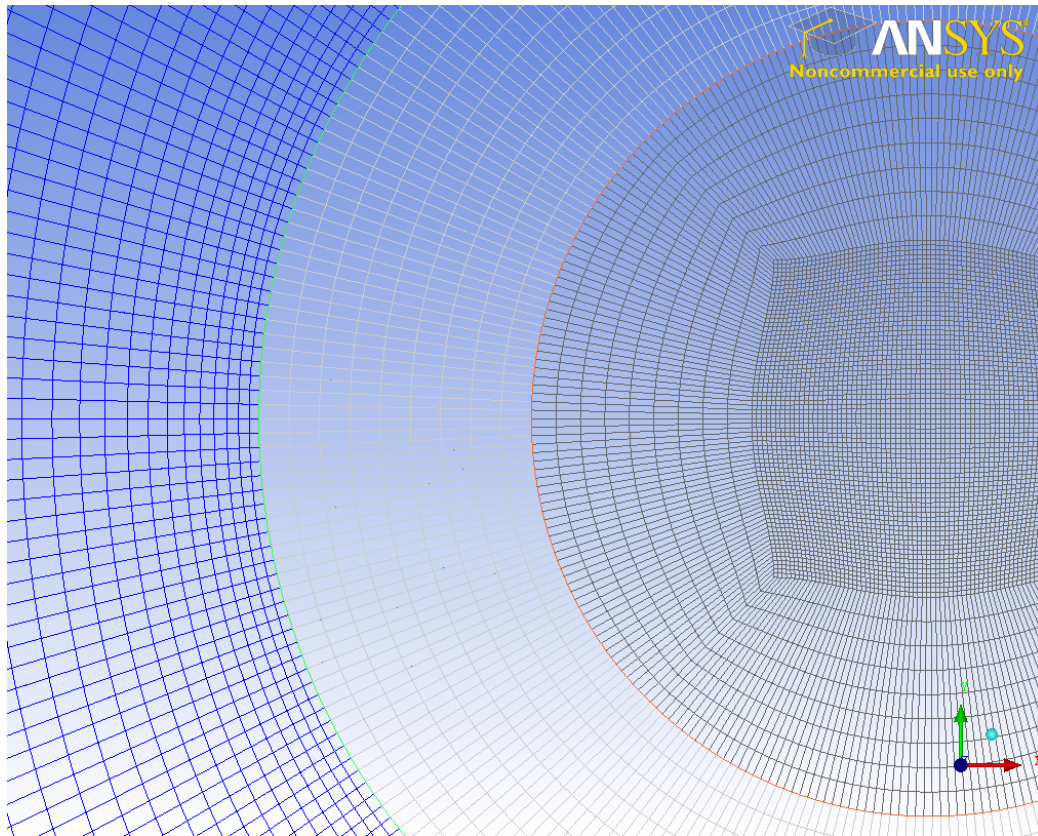


Figure 4.2: Closeup view of the computation mesh at the conductor. The fluid, aluminum, and steel zones are shown with small wall-adjacent cell at the conductor.

is given in Figure 4.2. The cell-adjacent length, in the fluid domain, was double and triple the distance, radially outward from the conductor in other meshes.

## 4.2 Standard Turbulence Wall-Function

CFD numerical solutions can be significantly impacted by the near-wall treatment for turbulent flows. Choosing the appropriate wall model and a consistent mesh is necessary for accurate representation of wall-bounded turbulent flows. Numerous experiments have shown the near-wall region consists of three layers; they are illustrated in Figure 4.3 [10]. The inner layer or viscous sublayer is characterized by flow that

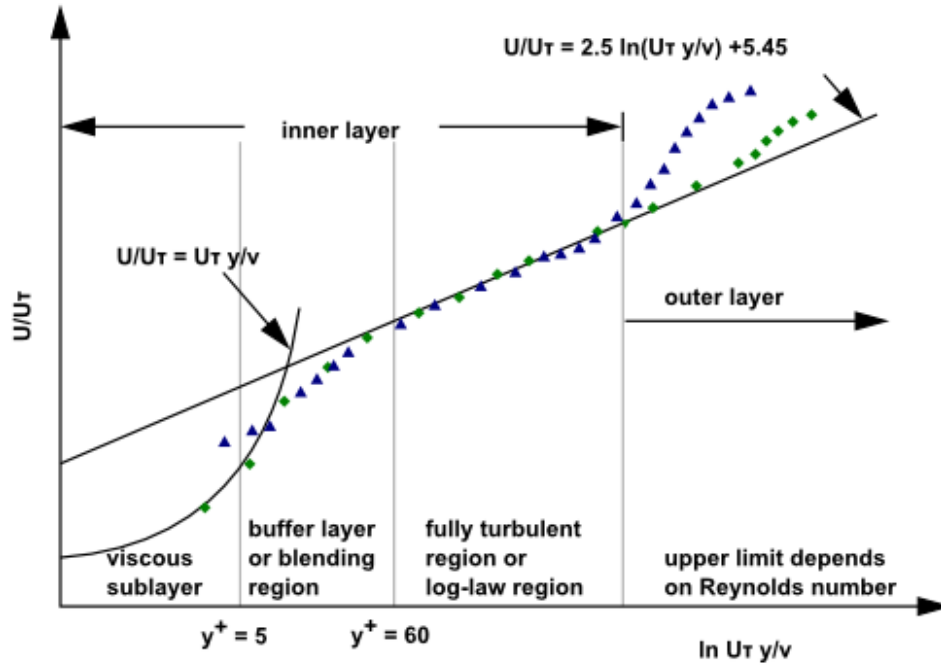


Figure 4.3: Subdivisions of the near-wall region. Adopted from [10].

is almost laminar, dominated by viscosity. Next is a buffer region where the effects of molecular viscosity and turbulence are equally important. The fully turbulent outer region has negligible viscous effects, where the production of turbulence and its destruction is in equilibrium. The vertical separation of the regions is determined by the non-dimensional distance,  $y^+$ , defined as

$$y^+ = \frac{\rho u_\tau y}{\mu}, \quad (4.1)$$

where  $u_\tau$  and  $y$  are the friction velocity and the distance to the wall, respectively.

It's the near-wall region where large gradients in velocity are present, here momentum and other scalar transports occur most vigorously. There are two approaches to handle near-wall flows, they are illustrated in Figure 4.4. The first approach uses

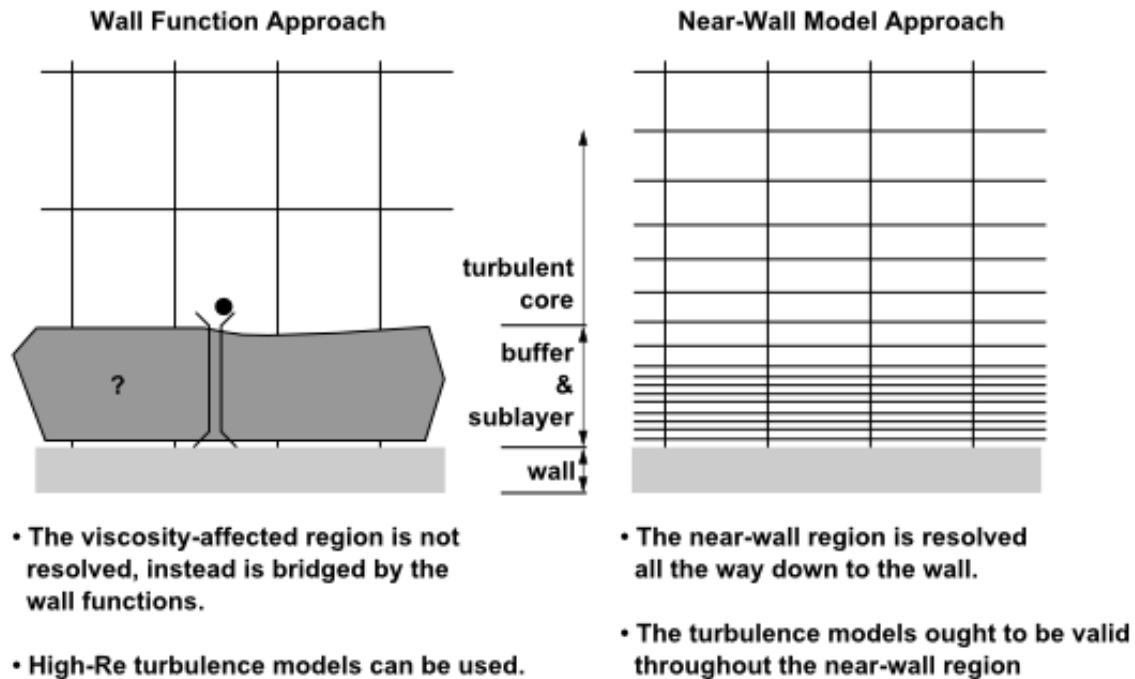


Figure 4.4: The two near-wall approaches used in turbulence modeling are depicted. The wall function approach is shown on the left, where the flow is not resolved but bridged with the use of a wall function. On the right, the near-wall model approach is shown, here the flow is resolved using a refined mesh near the wall. Illustrations adopted from [10].

semi-empirical formulas or wall-functions to model between the wall and turbulent region. The second is using modified turbulence models, which enables the viscosity dominated region to be resolved. This approach requires a refined mesh near the wall and is computationally more expensive.

When the standard wall-function model is employed, the laminar and buffer region are parameterized as turbulent stresses at the wall. The cell-adjacent centers should be located a sufficient distance from the wall, consistent with the standard wall-function formulation. The lower limit lies in the order of  $y^+ \sim 15$ , below this the wall functions will typically deteriorate and the accuracy of the solution cannot be maintained [10].

### 4.3 Conjugate Heat Transfer

Various modes of heat transfer can be modeled with ANSYS FLUENT, including natural and forced convection as well as conduction. Electrical current flowing through a conductor causes Joule heating to occur. This heating is modeled as a conjugate heat transfer problem coupled to the fluid flow over the conductor. The transport of thermal energy is computed, given as

$$\frac{\partial(\rho E)}{\partial t} + \nabla \cdot [\mathbf{V}(\rho E + \rho)] = \nabla \cdot \left[ k_{eff} \nabla T - \sum h_j \mathbf{J}_j + \tau_{eff} \cdot \mathbf{V} \right] + S_h. \quad (4.2)$$

Here  $E$  is the energy per unit mass,  $k_{eff}$  is the effective conductivity,  $\mathbf{J}_j$  is the diffusion flux of species  $j$ , and  $S_h$  is a source heating term. Transport of thermal energy is computed in the simulations for both the fluid (air) and solid (conductor) domains. There is a coupled thermal condition at the boundary between the fluid and solid domain.

### 4.4 IEEE Transient Temperature Calculation

Numerical methods are used to solve the ODE that governs conductor transient temperature change in time, Equation 3.4. Results of the temperature change in time can be greatly affected by the numerical method and size of the time step employed. The IEEE Standard 738 does not give a recommended numerical method to solve the ODE. However, a Quick Basic computer code is supplied in Annex B of the standard, it is used to calculate the conductor temperature as a function of time after a step change in current. The code is a forward Euler method, requiring the time-step size

be sufficiently small in accordance with the thermal time constant, and is prudent to recalculate results with a smaller time step to check the change in results.

This section examines how the numerical method and time step size can affect the solution of the ODE governing the conductors temperature change in time. The IEEE Standard 738 provides an example of a transient temperature response to a step change in current; it is shown in Figure 3.3. The step change in current from 800 to 1,300 Amps is used in this analysis, and the IEEE result, which has a time step of 1 minute, has been digitized. Conductor and environmental conditions are held constant in this example.

In this analysis, a forward Euler's method, like that supplied in the IEEE Standard, is compared with a 4<sup>th</sup> order RK method using different time step sizes. Background on these numerical methods is given in Section 3.3. The Euler and 4<sup>th</sup> order RK methods with time step sizes of 5, 10, and 20 minutes are compared using a normalized L2-norm. The normalized L2-norm is given by

$$\|x\|_2 = \frac{1}{n} \sqrt{x_1^2 + x_2^2 + \cdots + x_n^2}, \quad (4.3)$$

where  $x_i$  is the difference between the calculated and true or reference conductor temperature. The true solution is not feasible, there is not a closed form analytical solution to the ODE. Here the reference temperature is calculated using MATLABs [59] built in ode45 solver, which is a 4<sup>th</sup> order RK method, with the time step size of 1 second. Results are given in Table 4.1, and shown graphically in Figures 4.6 and 4.5.

It's clear that there needs to be careful consideration of the numerical method employed when solving the ODE representing a conductors temperature change in time. If an Euler method is applied, which is only 1<sup>st</sup> order accurate, the time step

Table 4.1: Normalized L2-norm of conductor temperature. Reference temperature calculated with MATLABs [59] 4<sup>th</sup> order Runge-Kutta method (ode45) with a time step size of 1 second.

<b>Runge-Kutta</b>	<b>L2-norm</b>
5 minute	2.48E-5
10 minute	3.43E-5
20 minute	4.36E-5
<b>Euler</b>	<b>L2-norm</b>
5 minute	0.830
10 minute	2.70
20 minute	12.82

size needs to be sufficiently small to maintain accuracy in temperature calculations. Euler’s method will over estimate a conductors heating or cooling response, because the new temperature is calculated using only the slope estimate at the begging of the time step. Additionally, if the time steps is sufficiently large, stability issues can be problematic, as shown by the 20 minute time step size.

However, when a 4<sup>th</sup> order RK is employed, which estimates the new temperature based on slope estimates at the beginning, middle, and end of the time step, a more accurate calculation is achieved. This allows for larger time steps to be taken and can greatly increase the computational efficiency of the ODE solution. Additionally, stability issues are less stringent, a single time step can be used over the entire hour and the numerical error remains negligible. The 4<sup>th</sup> order RK method essentially makes the transient solution independent of the time step size.

To determine the speedup that is gained by employing a 4<sup>th</sup> order RK, the computational time of the transient solution of both methods was compared at the thermal time constant. The thermal time constant is the time required for the

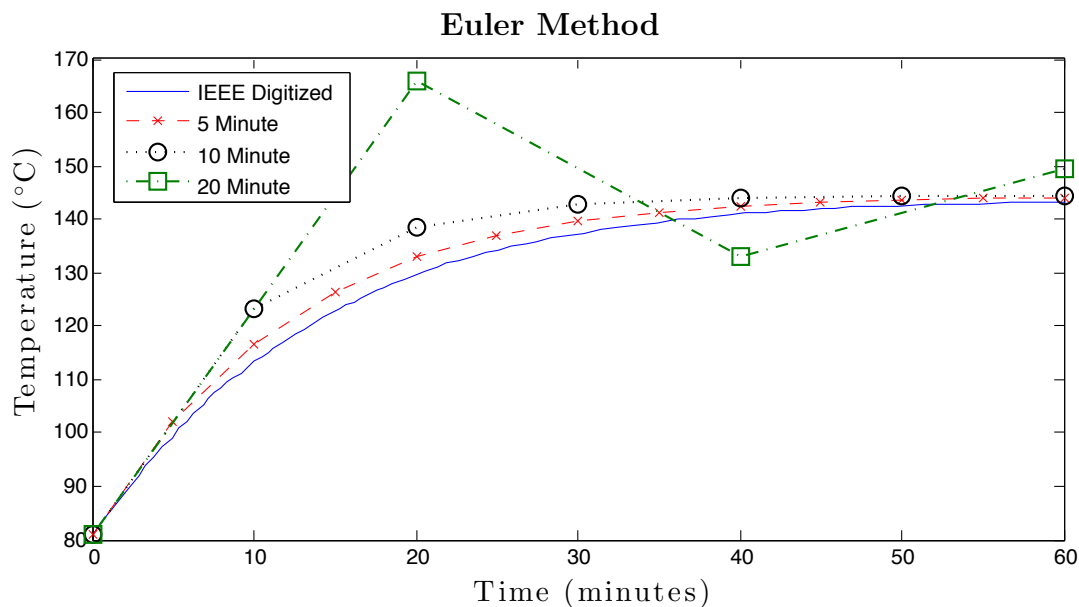


Figure 4.5: Transient conductor temperature solution using Euler's method with 5, 10, and 20 minute time step size. The time step used in the IEEE digitize solution is 1 minute.

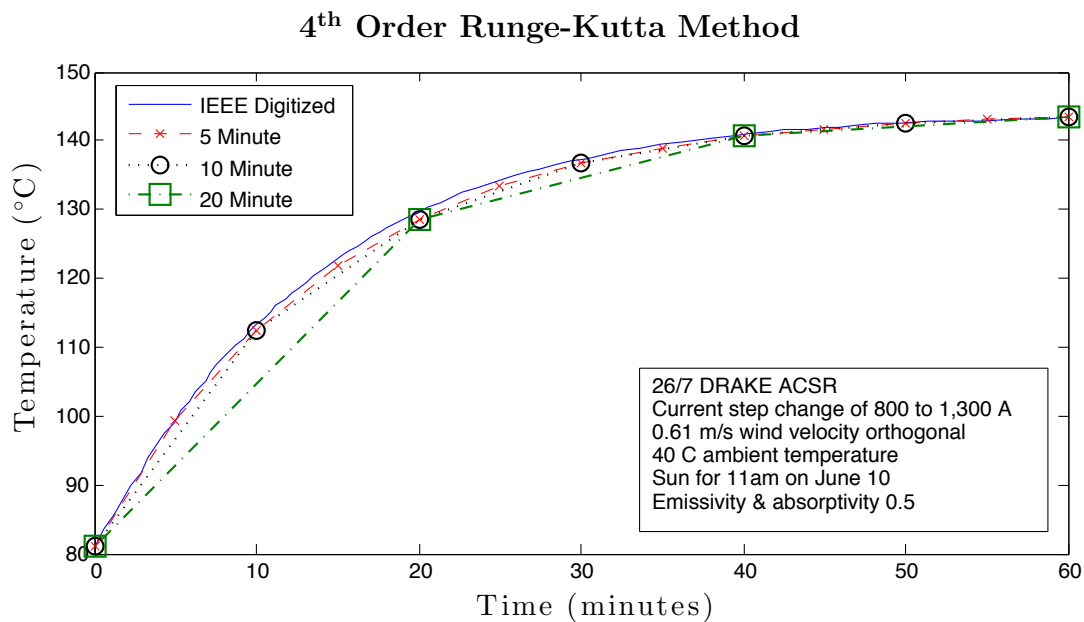


Figure 4.6: Transient conductor temperature solution using 4<sup>th</sup> order Runge-Kutta method with 5, 10, and 20 minute time step size. The time step used in the IEEE digitize solution is 1 minute.

conductor temperature to accomplish 63.2% of a change in initial temperature to the final temperature. For this example, the thermal time constant is 14 minutes and 22 seconds. The IEEE standard states that a time step of 1% of the thermal time constant is usually sufficient, and therefore used in this comparison. The 4<sup>th</sup> order RK employs a single time step over the thermal time constant. Computational speedup using the 4<sup>th</sup> order RK is  $\sim 50\times$  and the numerical error, compared to the reference temperature, is 1.12E-1 and 1.68E-6 for the Euler and RK method, respectively.

## 4.5 Steady-State and Transient Heating Validation

Validation of IEEE Standard 738 convective cooling equations was desired, therefore the solar heating and radiative losses were set to zero for CFD simulations and IEEE numerical calculations. Steady-state simulations with wind conditions ranging from 0.5–3 m/s orthogonal to the conductor axis were done using a laminar flow model. The standard k- $\epsilon$  turbulence model with standard wall-function was used with wind conditions ranging from 2–10 m/s. This is necessary because the standard k- $\epsilon$  model does not detect laminarization. Both models were used in the transition region from laminar to turbulent flow, where wind velocity was 2 and 3 m/s; here the Reynolds numbers based on conductor diameter are  $\sim 3,100$  and  $\sim 4,700$ , respectively.

The Joule heating is not modeled, instead a heat generation term is applied. Aluminum strands carry 98–99% of the current in ACSR conductor [21], therefore in this analysis the Joule heating is assumed to occur in the aluminum region only. The heat generation,  $S_h$ , is calculated as

$$S_h = \frac{I^2 R}{Al}, \quad (4.4)$$

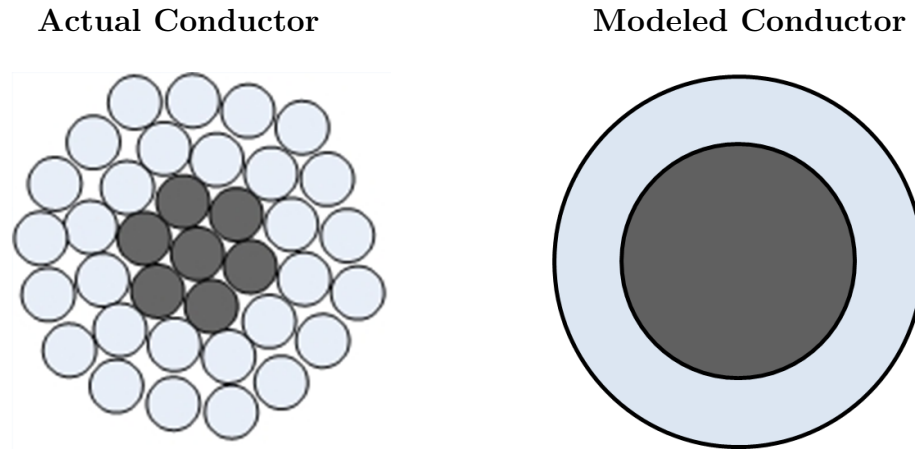


Figure 4.7: ACSR conductor consists of many individual wires but is modeled as two concentric cylinders, aluminum outer with a steel core. The outer diameter and aluminum cross-sectional area are kept constant.

where  $A$  is the cross-sectional area of the Aluminum zone and  $l$  is the same unit length as the given resistance,  $R$ .

Starling 26/7 ACSR transmission conductor is used in this analysis. It's a common high-voltage conductor and its properties are given in Section 3.1. This transmission conductor does not represent actual IPCo transmission lines in the test area. This is simply a test case scenario. The outer diameter and cross-sectional area of the modeled aluminum zone needs to equal that of the actual Starling conductor nominal diameter and total cross-sectional area of the individual aluminum wires, as illustrated in Figure 4.7. A constant outer diameter will ensure a constant Reynolds number between model and actual conductor, and an equivalent cross-sectional area between the model and actual conductor ensure the heating value per unit length of conductor remains consistent.

Conductor temperature in CFD simulations is calculated using the average temperature over the core of conductor. The steady-state results are shown in Figure 4.8, and the corresponding maximum wall-adjacent  $y^+$  value is shown in Figure 4.9. CFD

simulation results and IEEE Standard 738 in general show a good agreement, having  $\sim \pm 2^\circ\text{C}$  differences. The CFD simulated conductor temperature is lower with wind velocity above 5 m/s. Neither model fit the transition region well, as expected. Transition modeling in fluid flow is an active area of research and is not in the scope of this validation study.

The transient conductor temperature simulations were completed in both laminar and turbulent flow conditions. The laminar flow CFD simulation was completed using a laminar flow model and inlet wind velocity of 1.0 m/s and time step size of 1E-3. The turbulent flow CFD simulation was completed using the standard k- $\epsilon$  turbulence model, standard wall-functions, inlet velocity velocity of 8 m/s orthogonal to conductor, and a 1E-5 second time step size. The IEEE Standard 738 transient temperature response, Equation 3.4, was calculated using MATLABs built in ode45 solver, which applies an adaptive time step algorithm to maintain relative and absolute tolerances of 1E-3 and 1E-6, respectively. The temperature time rate of change is dependent on the heat capacity of conductor, so the model and actual conductor must be equivalent. The modeled aluminum cross-sectional area is equal to the individual strands of the actual conductor as illustrated in Figure 4.7, and the specific heat value for the aluminum remains unchanged. However, the specific heat of the steel core must be adjusted in proportion to the difference in area between model and actual conductor.

Results of transient CFD simulations and IEEE ODE numerical calculations for both laminar and turbulent flow conditions were plotted and results are in agreement, validating the use of the ODE equation governing conductor temperature change to be used for DLR calculations. CFD simulation results of the laminar simulation, with a Reynolds number  $\sim 1,500$ , are shown in Figure 4.10, the velocity vectors are shown

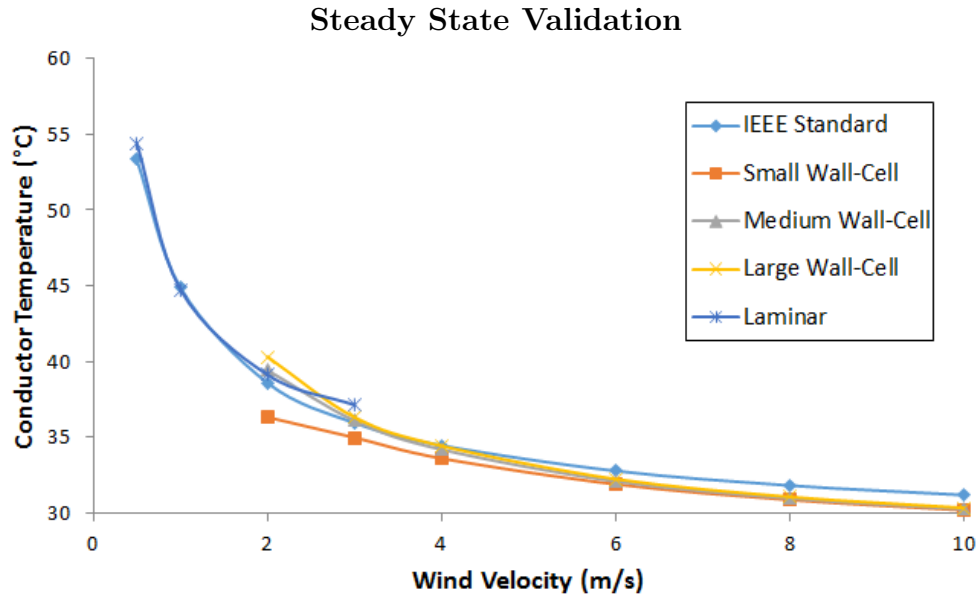


Figure 4.8: Validation of IEEE Standard 738 steady state conductor temperature. Laminar flow model was used for low wind velocity, 0.5-3 m/s, and a standard  $k-\epsilon$  model with standard wall functions for velocity ranging from 2-10 m/s. Results show different cell-adjacent size near the wall.

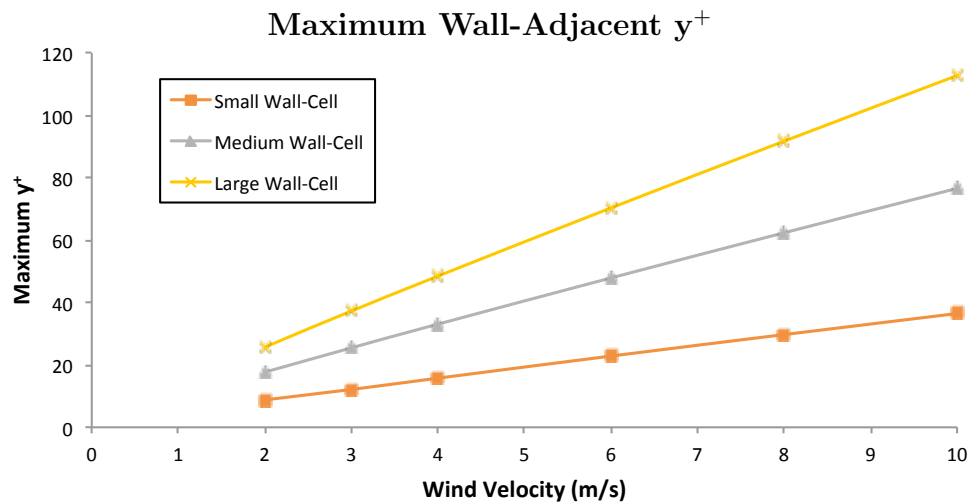


Figure 4.9: Maximum wall-adjacent  $y^+$  value of different wall-adjacent cell size.

on the top and temperature contour is given on the bottom.

## 4.6 Conclusion

CFD simulations were carried out to validate IEEE Standard 738 steady-state and transient equations. The simulations were modeled as a conjugate heat transfer problem coupled to the fluid flow over the conductor. A laminar flow model was utilized with low Reynolds number flow and a  $k-\epsilon$  turbulence model with a standard wall-function was applied for turbulent flow conditions.

The steady-state temperature had a variation of  $\sim \pm 2^\circ\text{C}$ , and CFD simulation results show conductor temperature to be lower when wind velocity is above 5m/s. The IEEE transient heating ODE equation was solved using MATLABs built in ode45 solver, to give 4<sup>th</sup> order accuracy. Transient CFD simulation results matched ODE numerical calculations well, validating the IEEE ODE equation to calculate conductor temperature change in time. The steady-state and transient validations instill further confidence in the use of IEEE equations in a DLR technology.

## Velocity Vectors and Temperature Contour Near Conductor

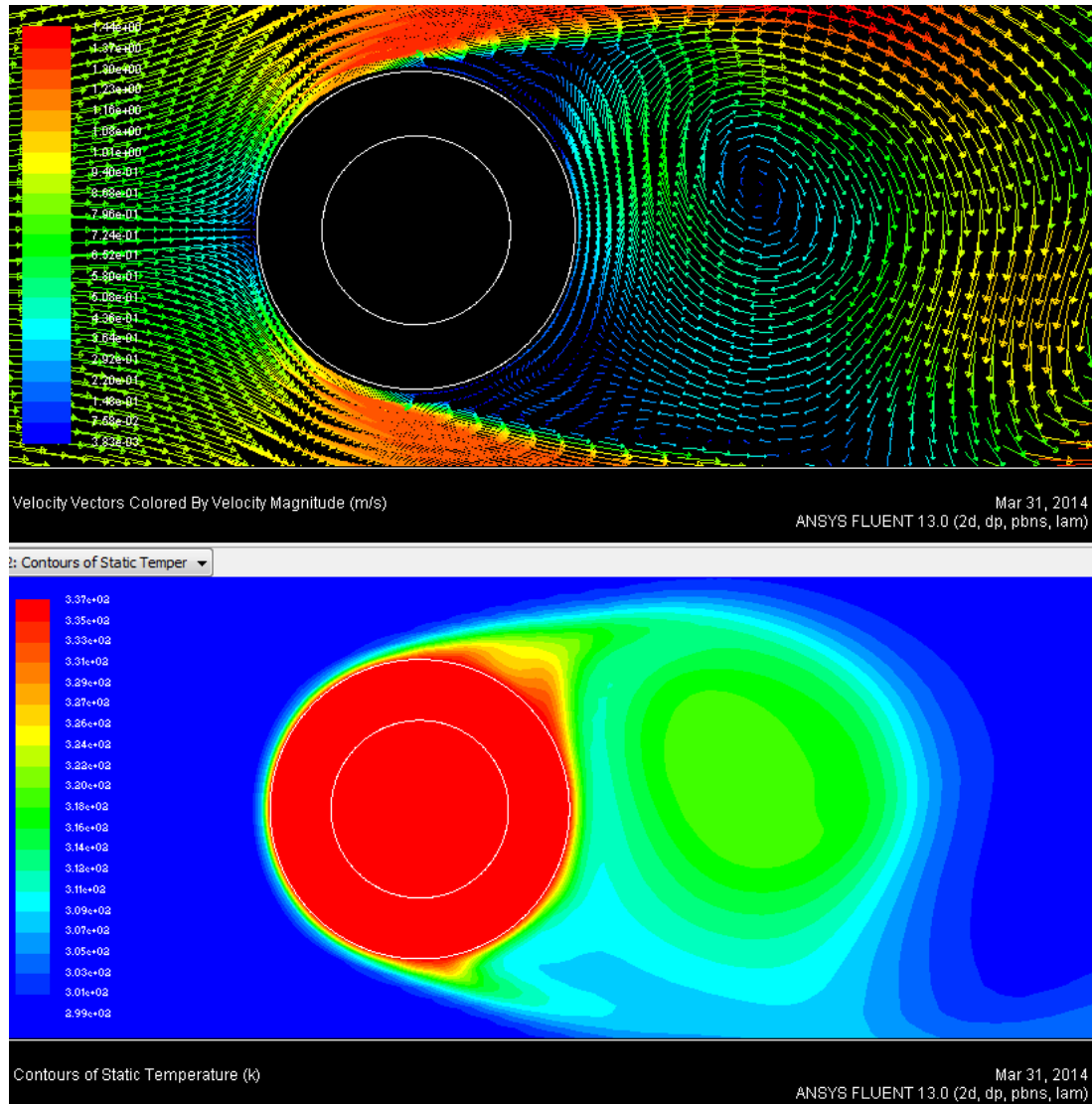


Figure 4.10: Velocity vectors (top) and temperature contour (bottom) of the laminar CFD simulation. Here the inlet velocity is 1 m/s, giving a Reynolds number  $\sim 1,500$ .

## CHAPTER 5

### INL & IPCO TEST BED ANALYSIS

This chapter discusses the motivation to implement a DLR system and presents existing efforts. The INL & IPCo collaborative DLR research test bed area and its instrumentation are described in sufficient detail. INL & IPCo have conducted a study on the increased capacity DLR potentially allows over the current SLR practice in this area. However, this study didn't address if capacity changes in response to the diurnal cycle of the ABL or what can be expected in the spring and fall seasons.

The analysis in this chapter will expand on INL & IPCo findings. The probability of capacity ratings during each hour of the day will be determined using year-long real-time weather data for each season. The methodology used in this analysis will be described in sufficient detail and the results of hourly capacity ratings for each season are presented.

#### 5.1 INL & IPCo DLR Motivation, Test Bed Area, and Previous DLR Analysis

Significant wind power generation projects in the southern Idaho region has greatly increased interest in a DLR system to increase transmission capacity. A natural synergy exists between wind generation and conductor convective cooling [13]. It's desired that when the wind blows, resulting in higher wind power generation, lines

can be dynamically rated higher than the current SLR practice allows. INL with funding from the DOE through the WWPTO, and IPCo have installed weather instrumentation along more than 160 kilometers of high voltage transmission lines to investigate the implementation of a DLR system. DLR capacity is highly dependent on local area climate, therefore without a systematic analysis of wind conditions along transmission lines throughout the year, the outcome of implementing a DLR system in this area is uncertain. Ideally, the analysis should cover multiple years to further increase confidence in the system.

The U.S. electric power demand follows daily, weekly, and seasonal patterns. Hot climate results in high afternoon power demand, while cold climates result in higher mid-morning and mid-afternoon demand. The correlation between DLR capacity and power demand should be addressed to adequately assess the value of DLR implementation. High ampacity ratings are desired during times of high electrical demand.

The INL and IPCo joint test bed area for DLR research is located on the Snake River Plain in southern Idaho, shown in Figure 5.1. The test site covers an area approximately 1,500 square kilometers of moderately complex terrain, which four high-voltage transmission lines traverse. It consists of small towns, large farmland, and high desert terrain. Elevation of the test site ranges from approximately 754 – 1,198 meters, the land topology and transmission lines are shown in Figure 5.2.

The INL & IPCo team have mounted seventeen weather stations in strategic locations along the transmission lines at a height of 10 meters above ground level. All of the weather stations are spaced between 1.5 and 8 kilometers. The measured quantities are wind speed, wind direction, and ambient temperature. Data from the weather stations are reported every 3 minutes; it's an average of 2-second readings

over the 3-minute time interval. Measurements have been continuing since August 2010 to date, and Boise State University (BSU) has been receiving daily data through electronic mail.

INL & IPCo conducted a study on the hypothetical DLR capacity increase over current SLR practice [41]. The summer and winter DLR capacity increase is given assuming different average wind speed and wind direction. However, this study did not investigate how the capacity changes throughout the day or what can be expected during the spring and fall seasons. Additionally, using an average wind velocity may not be the best practice, as wind doesn't generally follow a normal distribution. A better fit is a Weibull distribution [58]. Therefore, this analysis expands on these findings by using year-long real-time weather data to determine the probability of capacity occurring during each hour of the day, during each season.

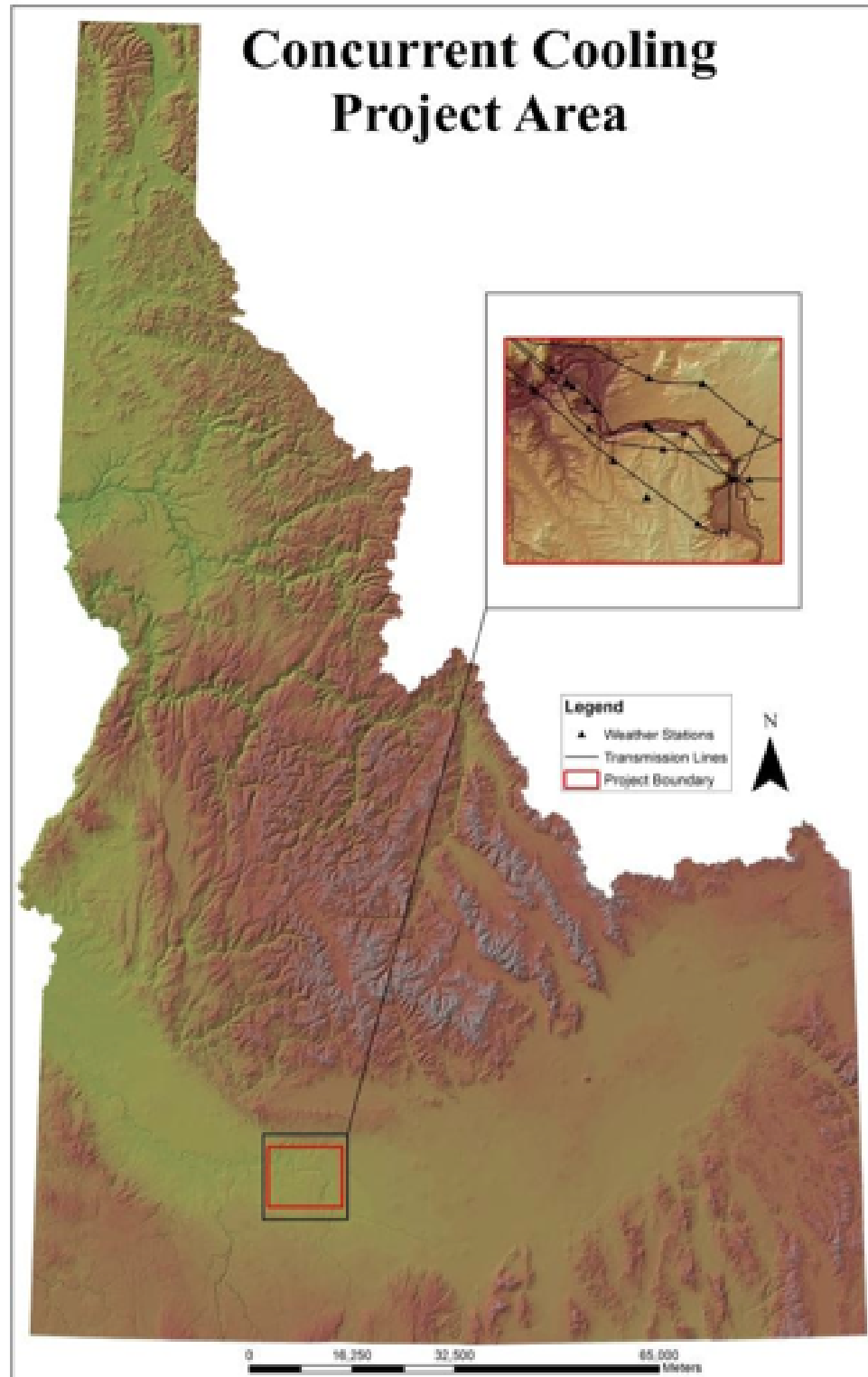


Figure 5.1: Idaho National Laboratory and Idaho Power's dynamic line rating research test bed location in southern Idaho [41].

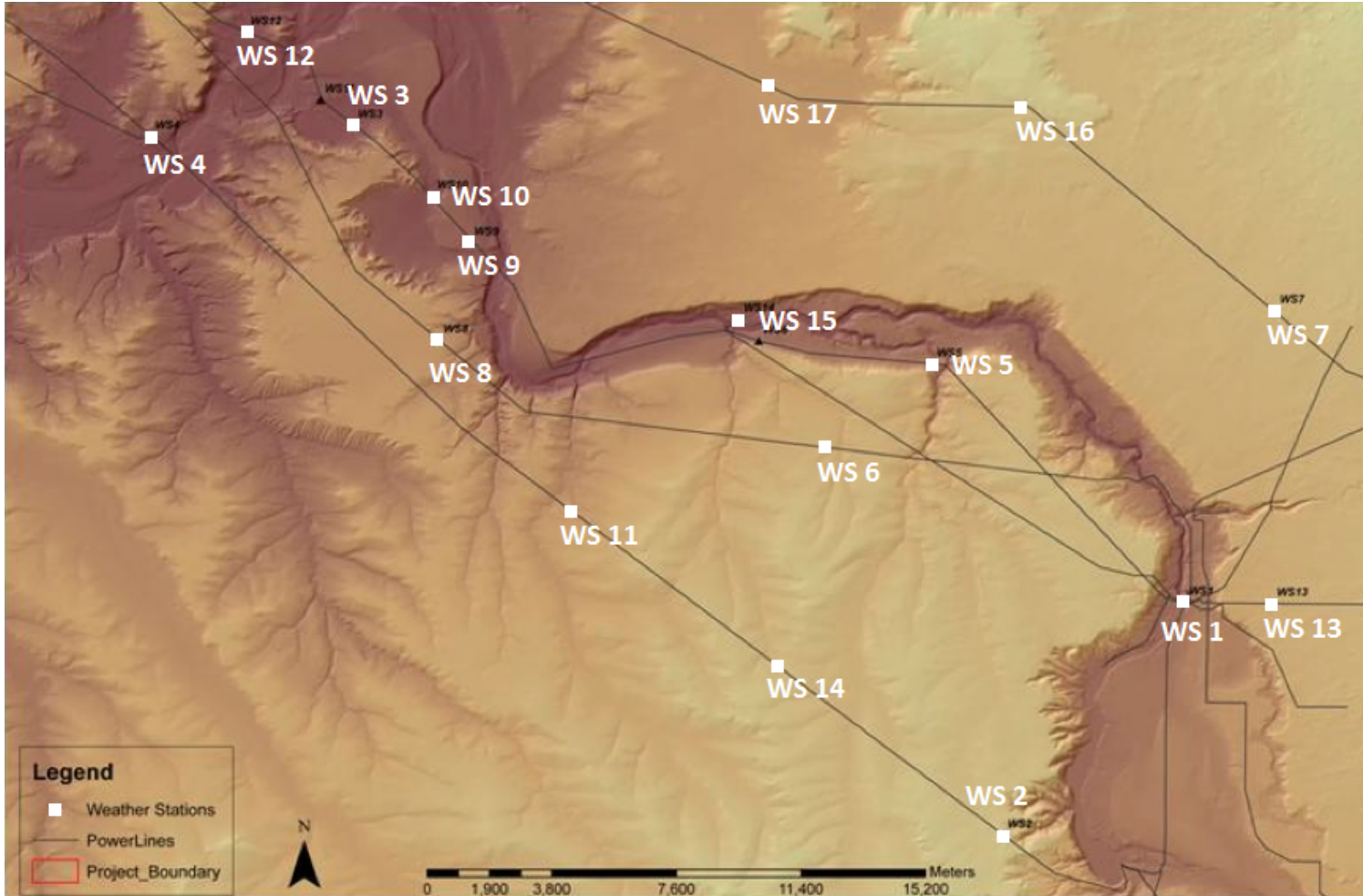


Figure 5.2: Land topology and transmission line's traversing through INL & IPCo DLR research test bed area [41]. Weather stations are labeled and the location is indicated by a white square.

## 5.2 Weather Station Selection for DLR Analysis

In this analysis, year-long weather data starting from July 1<sup>st</sup> 2012 from the INL & IPCo test bed was used. The analysis is separated into four seasons: spring (Mar-May), summer (June-Aug), fall (Sept-Nov), and winter (Dec-Feb). Anytime four values are presented, they follow this order, spring to winter. All wind velocity, angle, and temperature data was run through a filter. This was necessary because at times weather stations were not on and gave erroneous results. The data was filtered with the following criteria: the velocity and angle had a minimum and maximum value of 0–50 mph and 0°–360°, respectively. The seasonal temperature was filtered with minimum and maximum temperatures of: –14 to 37, –1 to 44, –19 to 39, and –32 to 22°C. These temperature values are based off record high and low temperatures in Boise, Idaho [89].

Transmission line ampacity is limited by the critical span, or segment that results in the highest conductor temperature, often the section experiencing the lowest wind velocity. Figure 5.3 depicts year-long wind velocity at all the weather stations in the INL & IPCo test bed area. It's clear different sections of line can expect different transmission capacity due to the spatial variation of wind velocity. For instance, wind velocity at weather station 1 is considerably lower than other weather stations, it would often be the critical span of a transmission line. Sections of transmission lines that are routinely the critical span may be replaced with higher capacity conductor to “balance” the ampacity along the transmission line.

Four transmission lines, each containing multiple weather stations, traverse the INL & IPCo DLR test area. In this analysis, the same transmission line used in the INL & IPCo analysis was selected. It contains weather stations 7, 16, and 17

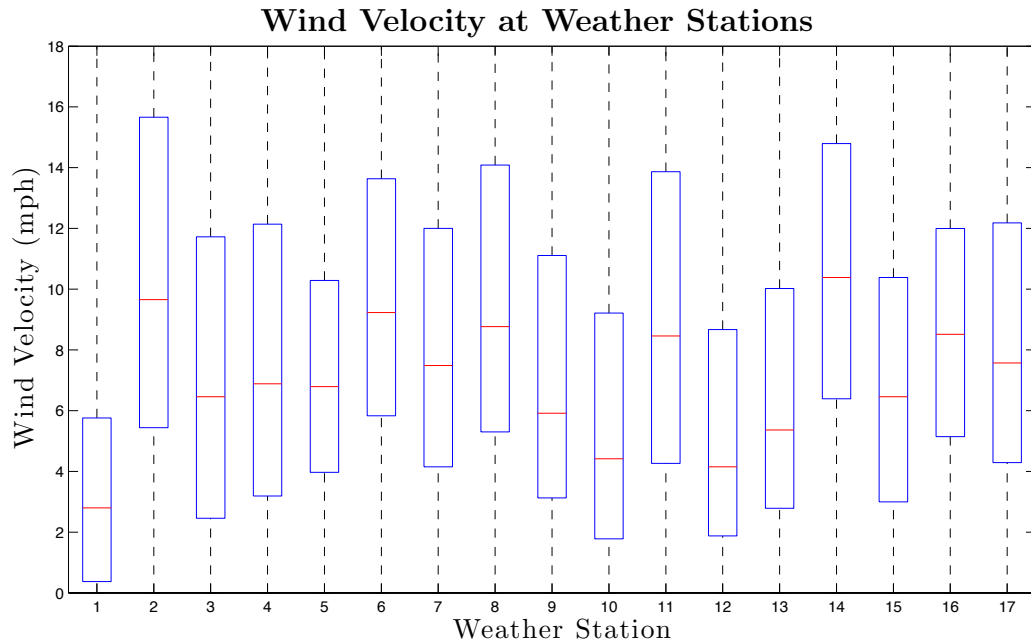


Figure 5.3: Wind velocities at all 17 weather stations from July 2012 through June 2013. Here the box represents the 75<sup>th</sup> and 25<sup>th</sup> percentile at the top and bottom, respectively, and the center line indicates the median.

along its path. The day and night wind velocity of these three weather stations is depicted in Figure 5.4. The daytime wind velocity at all three weather stations is fairly consistent. Weather station 17 (WS17) had lower wind velocity at night during the spring, summer, and fall. Weather station 7 had a lower wind velocity in the winter, however the data has been deemed deficient, having wind velocity readings of 0 m/s over several large time intervals, shown in Figure 5.5. Therefore, weather station 17 was chosen for the DLR analysis in this thesis.

It should be noted that although WS17 has an overall lower wind velocity, and thus used for DLR analysis, this does not imply or guarantee that it is the critical span location at any given time. The weather station with the highest overall wind velocity could at times be the limiting section. Only statistically speaking, WS17 is most likely the limiting section and therefore is used in this analysis.

### Weather Station Wind Velocity

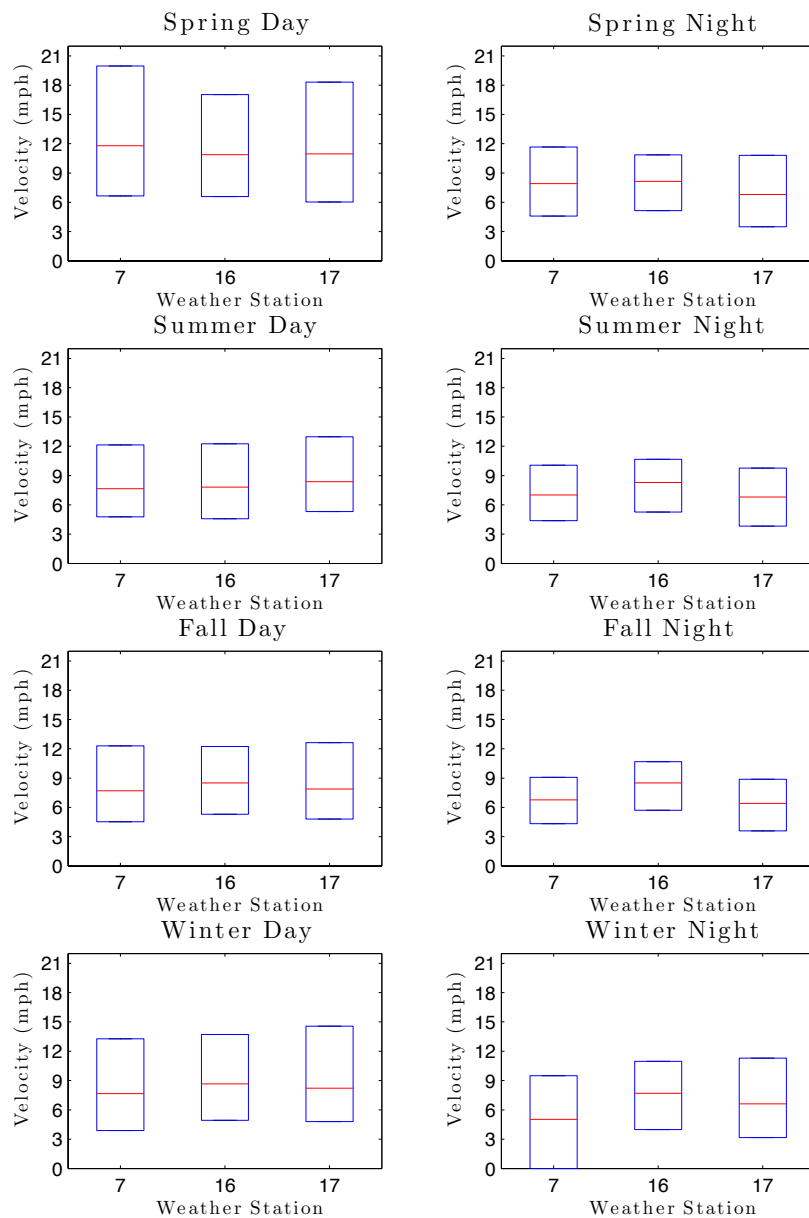


Figure 5.4: Seasonal day and night wind velocity from July 2012 to June 2013 at weather stations 7, 16, and 17. The box represents the 75<sup>th</sup> and 25<sup>th</sup> percentile at the top and bottom respectively, the center line represents the median. WS7 winter wind velocity data is deficient.

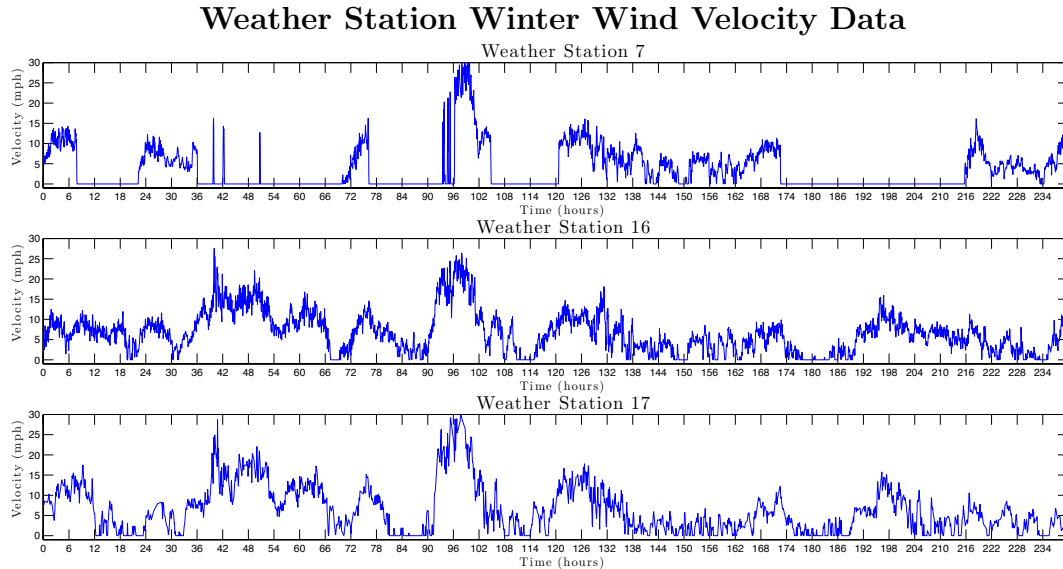


Figure 5.5: Winter wind velocity at weather stations 7, 16, and 17. Weather station 7 did not collect data over several large time spans, giving readings of 0 m/s, therefore it has been deemed deficient.

### 5.3 DLR Capacity Results

The transmission conductor used in the analysis is Starling 26/7 ACSR. It's a common high-voltage conductor; its properties are given in Section 3.1. This conductor does not represent the actual transmission conductors used by the IPCo. It serves only as a test case scenario. Southwire [85] rates Starling ampacity at 849 Amps, calculated assuming a  $75^{\circ}\text{C}$  maximum conductor temperature, 0.61 m/s wind velocity, and  $25^{\circ}\text{C}$  ambient temperature in sun.

The DLR capacity in this analysis are calculated using IEEE Standard 738 and real-time wind velocity, angle, and ambient temperature. The transmission line at WS17 is assumed to run in the WNW-ESE direction, have an elevation of 1,000 meters above sea level, and a latitude of  $43.6^{\circ}$ . Absorptivity and emissivity of the conductor are assumed to be 0.5. The real-time solar heating value is calculated

assuming a clear atmosphere and azimuth angle of  $90^\circ$ ; this is the maximum solar heating possible, and therefore is conservative.

Hourly ampacity results for each season are shown in Figure 5.6. The lines represent the 10<sup>th</sup> through 90<sup>th</sup> percentile of the DLR ampacity from bottom to top, respectively. The horizontal dashed line is the 849 Amp static rating given by Southwire. The percentile is a measure used in statistics, it indicates the value a given percentage of observations fall below. For example, the 20<sup>th</sup> percentile is the ampacity rating 20% of the ampacity observations falls below, or it can be stated: it's the ampacity value that is exceeded 80% of the time.

## 5.4 Conclusion

It's clear that a SLR approach is limiting transmission capacity in this area, especially during times of elevated wind velocity, when large wind generation should be expected. Lowest DLR capacity occurs during the summer, when high ambient temperatures and low wind velocities exist. Even under unfavorable conditions the 10<sup>th</sup> percentile only falls below current SLR around midnight, when wind drops near zero and electrical demands are low. Each season in general shows over a 70% increase half of the time, and a 20% increase 90% of the time.

However, the above discussion is limited to the local observation at weather station 17. Transmission ampacity is limited by the section experiencing the highest temperature along the entire length of the transmission line, therefore spatial variation of wind speed is determined using numerical wind model simulations.

### Hourly Seasonal DLR at Weather Station 17

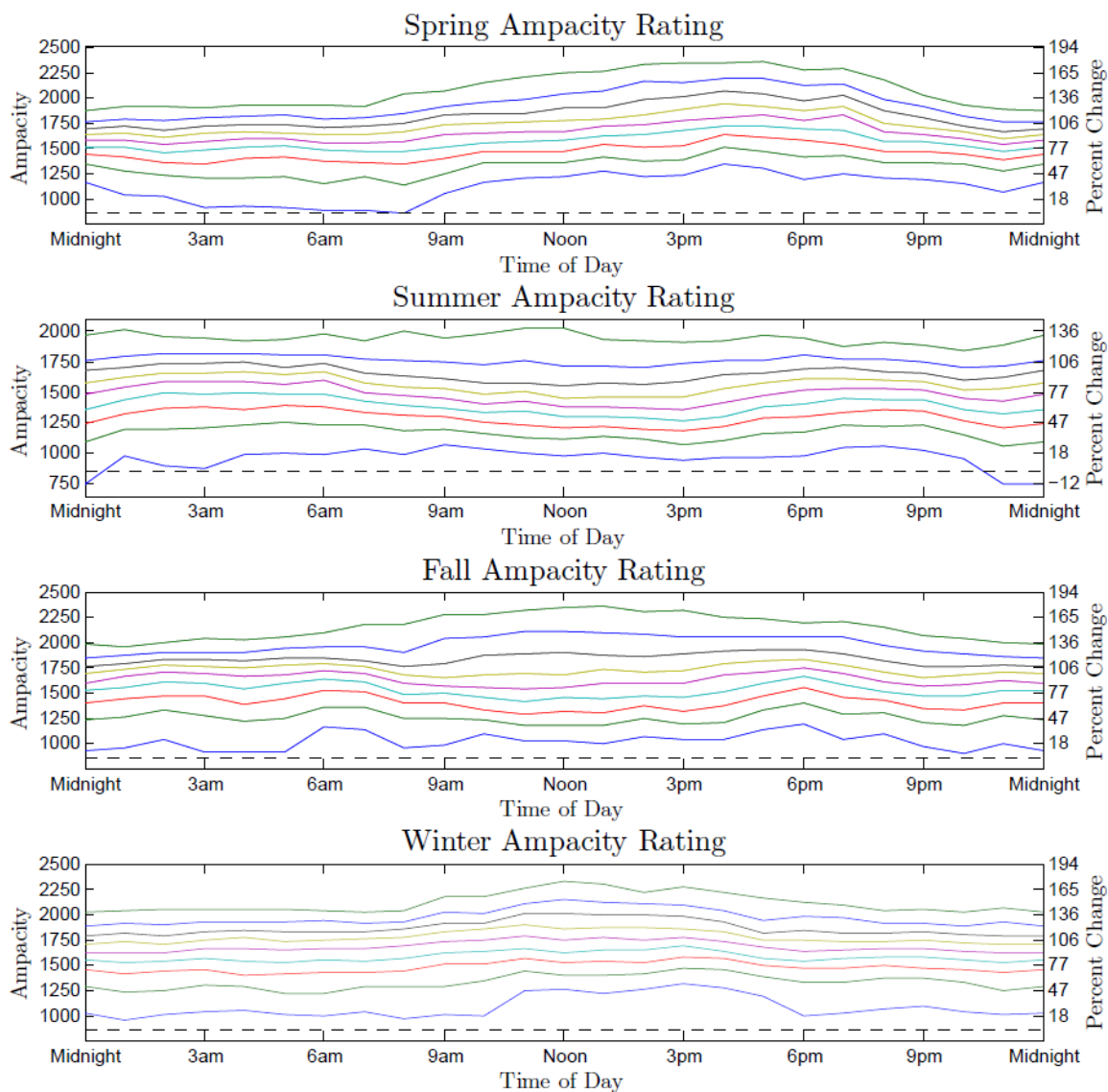


Figure 5.6: Hourly seasonal DLR at weather station 17. The horizontal line is the static ampacity and the variable lines represent the 10<sup>th</sup> – 90<sup>th</sup> DLR percentile from bottom to top, respectively.

## CHAPTER 6

### DLR USING A NUMERICAL WIND SOLVER OVER COMPLEX TERRAIN

Conductor thermal ratings are limited by the hottest spot along the entire length of the conductor. The spatial variation of wind speed and its direction associated with complex terrain has made implementation of current commercially available DLR systems in regions of complex terrain difficult. Such DLR systems only give an average temperature measurement over large transmission spans, or a limited number of single fixed point temperature measurement. Adding enough instrumentation to reduce error to acceptable levels is typically not feasible because they are too expensive [42]. However, with today's improved wind and weather models, communication systems, and computing hardware, the use of numerical wind models over complex terrain to calculate conductor temperature in dense intervals has become a possibility.

Using sparse weather measurements over a large area, the multi-GPU (graphics processing unit) numerical wind solver currently being developed at Boise State University is utilized to extract wind speed along the path of transmission lines where no telemetry is available in dense intervals. A test case scenario that assumes a constant loading condition is used to show the spatial conductor temperature that can occur in regions of complex terrain. Numerical wind simulation results are validated using real-time wind velocity data from the INL & IPCo DLR test bed.

## 6.1 Accelerated Multi-GPU Numerical Wind Solver

Meso-scale numerical weather prediction models have been used to forecast winds, however their applicability to micro-scale ABL flows and ability to reliably predict wind speeds within the surface layer is not clear. In this analysis, a multi-GPU parallel wind solver, which has been under continuous development at BSU since 2007 [27, 50, 90], to potentially forecast winds over complex terrain at the micro-scale level is used for numerical wind simulations. Computational domain size of micro-scale simulations can range from meters to several kilometers. The computations are accelerated on GPU clusters with a dual-level parallel implementation that interleaves Message Passing Interface (MPI) with NVIDIA's Compute Unified Device Architecture (CUDA). The overall goal is to forecast micro-scale atmospheric flows over complex terrain.

In the wind solver, a hybrid RANS-LES technique [78] that blends the Lagrangian dynamic SGS model [61] with the Prandtl's mixing length model is used for turbulence closure. The Lagrangian dynamic model is a localized model and does not require any homogeneous directions in the computational domain, therefore is adequate for arbitrarily complex terrain. In the solver, a Cartesian IBM is used to impose boundary conditions on the surface using logarithmic reconstructions [79]. Additionally, the Cartesian mesh method maps well to the computer architecture of GPUs, allowing for efficient parallel computing [27]. For more detailed background on the BSU wind flow solver and GPU cluster architecture for accelerated computation, the reader is referred to [27, 50, 90].

## 6.2 Application of the Numerical Wind Solver

The wind inlet velocity and direction used in the wind solver was selected to mimic real-time wind conditions over the test bed area. Season long real-time wind velocity and direction are depicted by the wind rose in Figure 6.1. Because some of the weather stations are located in areas of complex terrain, only data from weather stations 2, 7, 8, 11, 13, 16, and 17 were used for the wind rose. These weather stations are in more “flat” terrain areas that better represent the “general” wind flow across the test bed area have less surface effects than those omitted. The color of the wind rose represents the wind velocity and the circular direction represent the direction wind is coming from. It’s clear that the prevailing wind over the test location is in the east and west directions and the wind velocity can be quite variable.

The wind solver is ran with lateral boundary conditions to give a constant direction and wind flow velocity across the terrain of  $\sim 6$  m/s from the west. The land area size covered in the simulation is  $40 \times 49$  kilometers, and the simulation domain extends vertically 1.9 kilometers from the lowest elevation in the test bed area. The Cartesian computational mesh is  $511 \times 1,023 \times 191$ , consisting of  $\sim 100$  million cells. The simulation is ran on 4 Tesla K20 GPUs and computation time is roughly 6 hours. Resulting wind velocity is then extracted at a height of 10 meters above ground level, shown in Figure 6.2.

Initial attempts to assess the wind flow solver has been done by comparing numerical wind velocity with real-time weather station measurements. It’s recognized that this is a difficult and incomplete task, as the current state of the wind solver does not permit time-dependent turbulent lateral boundary conditions. The current neutral stability assumption is also far from the reality of convective turbulence over

the complex terrain. Additionally, point-wise weather station data can be highly influence by local variations in the terrain, which may be missing in the simulations. Therefore, the current assessment of simulation results as preliminary at this stage.

In light of these reservations, the mean wind speed of 27 discrete hour-long real-time measurements, which best represent or mimic the numerical wind solver boundary conditions (Figure 6.3) have been selected for comparison. Each discrete wind speed is calculated using the real-time data, sampled in 3 minute time intervals. The mean and standard deviation of the 27 discrete measurements have been calculated and compared with numerical results, shown in Fig. 6.4. Weather stations 7, 12, and 13 did not fall in the domain of the flow solver, and therefore they are excluded.

Eight of the fourteen wind speed calculations matched real-time measurements rather well, however six fall outside the standard deviation. At this time, it is unclear if this is due to the developmental stage of the flow solver or digitization of the weather station location, which was done using Fig. 5.2. Winds in regions of complex terrain can dramatically change within a few meters because of local effects that may not be present in the simulations. For instance, weather stations 3, 5, and 15 are located in complex terrain where small variations in position can have a large effect on wind speed. Additionally, weather station 14 data has been deemed deficient.

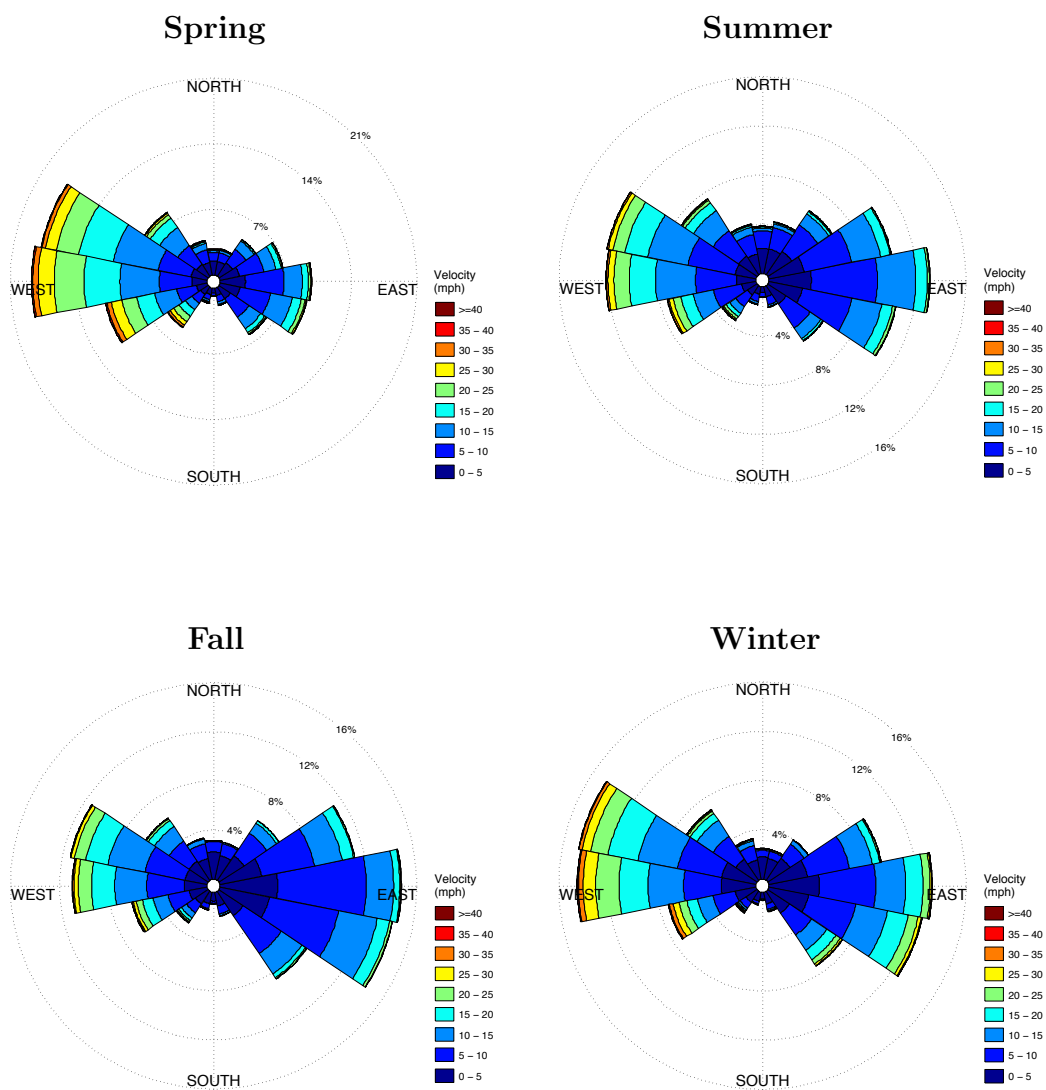


Figure 6.1: Seasonal wind velocity and direction.

Wind Contour at 10m Elevation under Neutral Stability

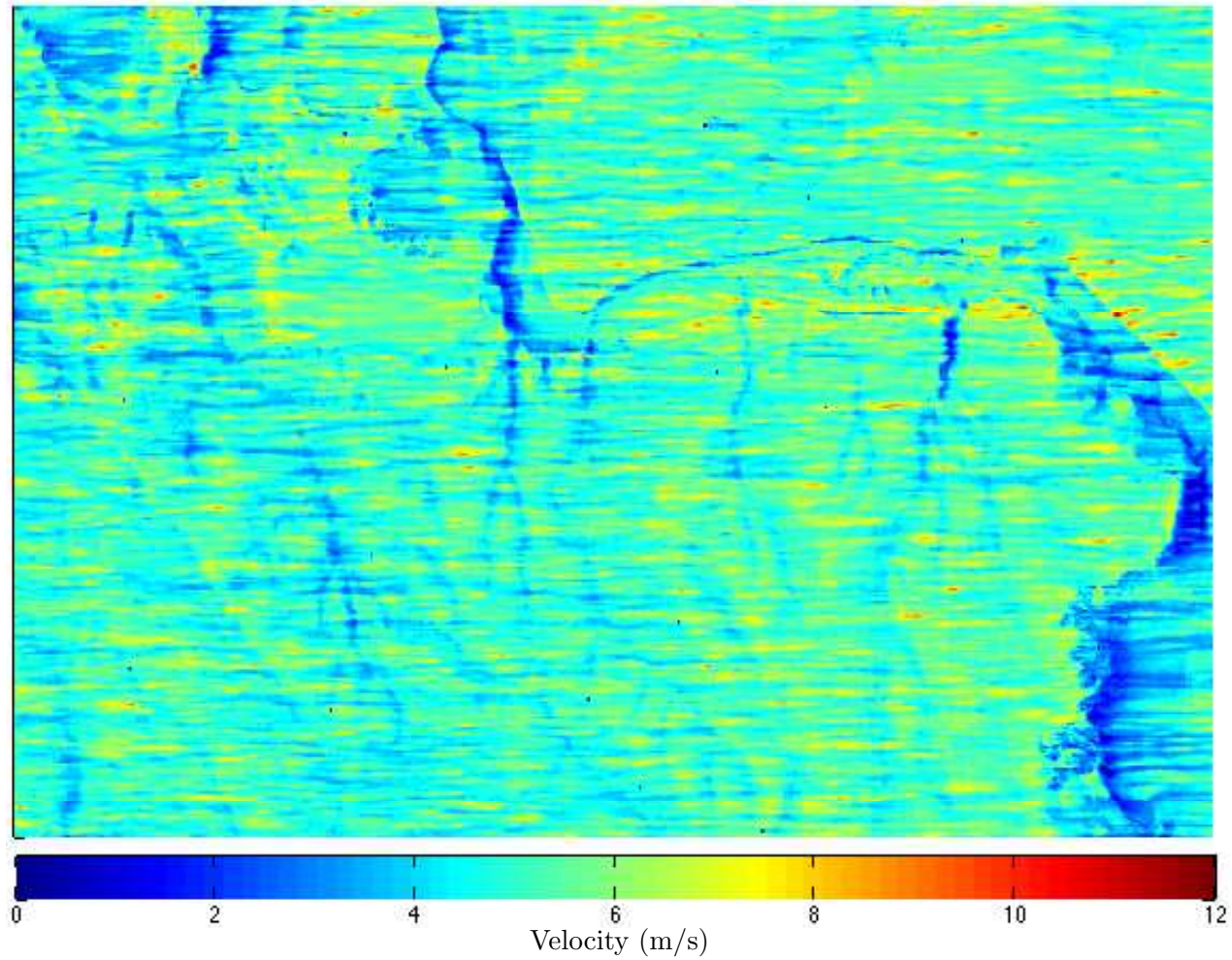


Figure 6.2: Wind contour over the test bed area, having a general wind flow from the west to east direction and  $\sim 6$  m/s wind velocity at 10 meters height.

### 6.3 Spatial Variation of Thermal Ratings Across Complex Terrain

Conductor temperature can have large spatial variation, especially in areas of complex terrain. This is one of the largest concerns with current DLR systems available today; they simply don't take enough measurements along the length of the transmission line. However, the use of numerical wind simulations allow wind conditions and the conductor temperature to be determined in dense intervals where no telemetry is available.

In this test case scenario, the wind velocity results described in Section 6.2 have been extracted along the length of transmission lines that traverse the test bed area. Using the extracted wind velocity, the steady-state conductor temperature is calculated assuming a constant load of 849 Amps, 35°C ambient temperature, 12 W/m solar heating, and Starling 26/7 ACSR conductor, which do not represent actual IPCo transmission lines in the test bed area.

The conductor temperature along the four transmission lines traversing the INL & IPCo test bed area is calculated at 6,385 locations. In the areas of complex terrain where large spatial variation of wind is expected, temperature calculations have been done in denser intervals. Results are superimposed with the land topography and shown in Figures 6.5 and 6.6. Here, results are shown at every 24<sup>th</sup> temperature point for a less cluttered visualization. The transmission lines have spatial changes of 23.5, 38.5, 48.1, and 20.9°C. The spatial temperature variation along the four transmission line is plotted in Figure 6.7. The horizontal line represents the emergency rating temperature of 75°C.

### Real-Time Wind Velocity and Direction

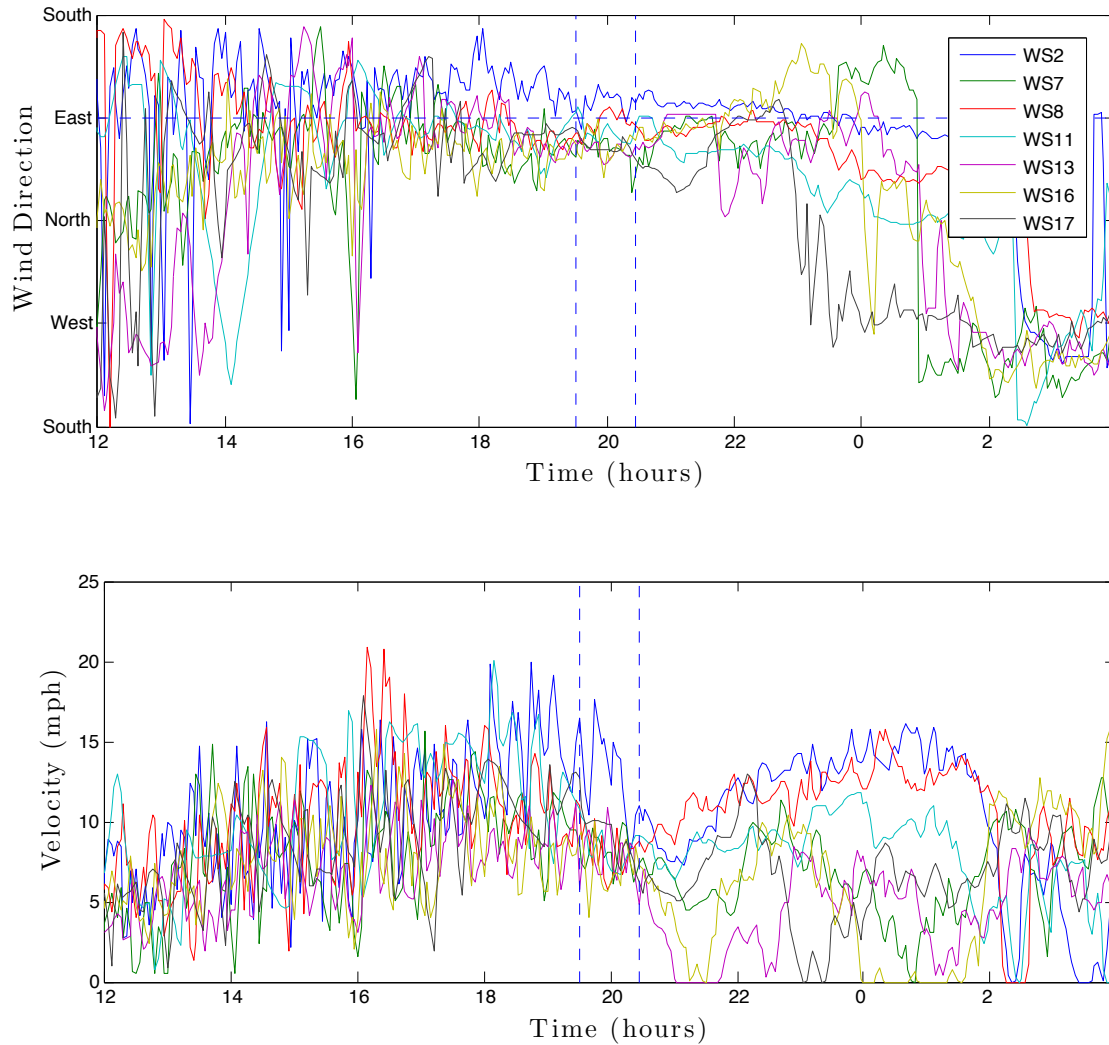


Figure 6.3: Example showing a discrete time interval of real-time wind velocity and angle selected for validation. The selected hour long data used is between the vertical dashed lines, when direction and velocity are stable and mimic the boundary conditions imposed on the wind solver. The horizontal dashed line represents wind that is out of the west, blowing in the east direction.

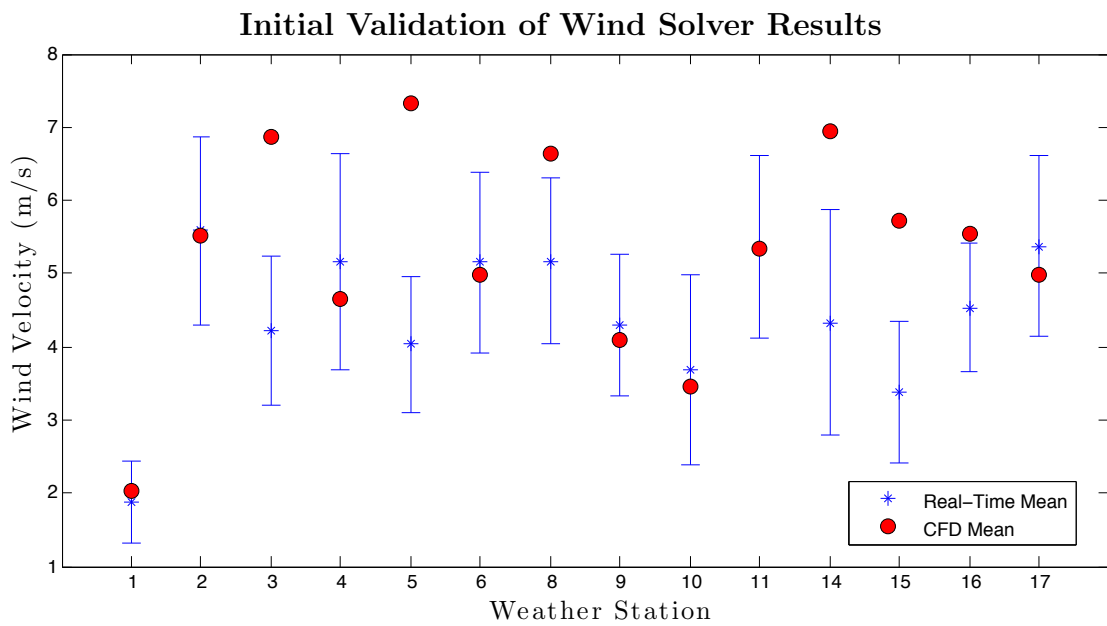


Figure 6.4: Initial attempt at validation of wind flow solver over the INL & IPCo test bed area. The mean and standard deviation of real-time hour-long (27 samples) data reading from the summer are compared with the mean wind velocity from the numerical wind solver.

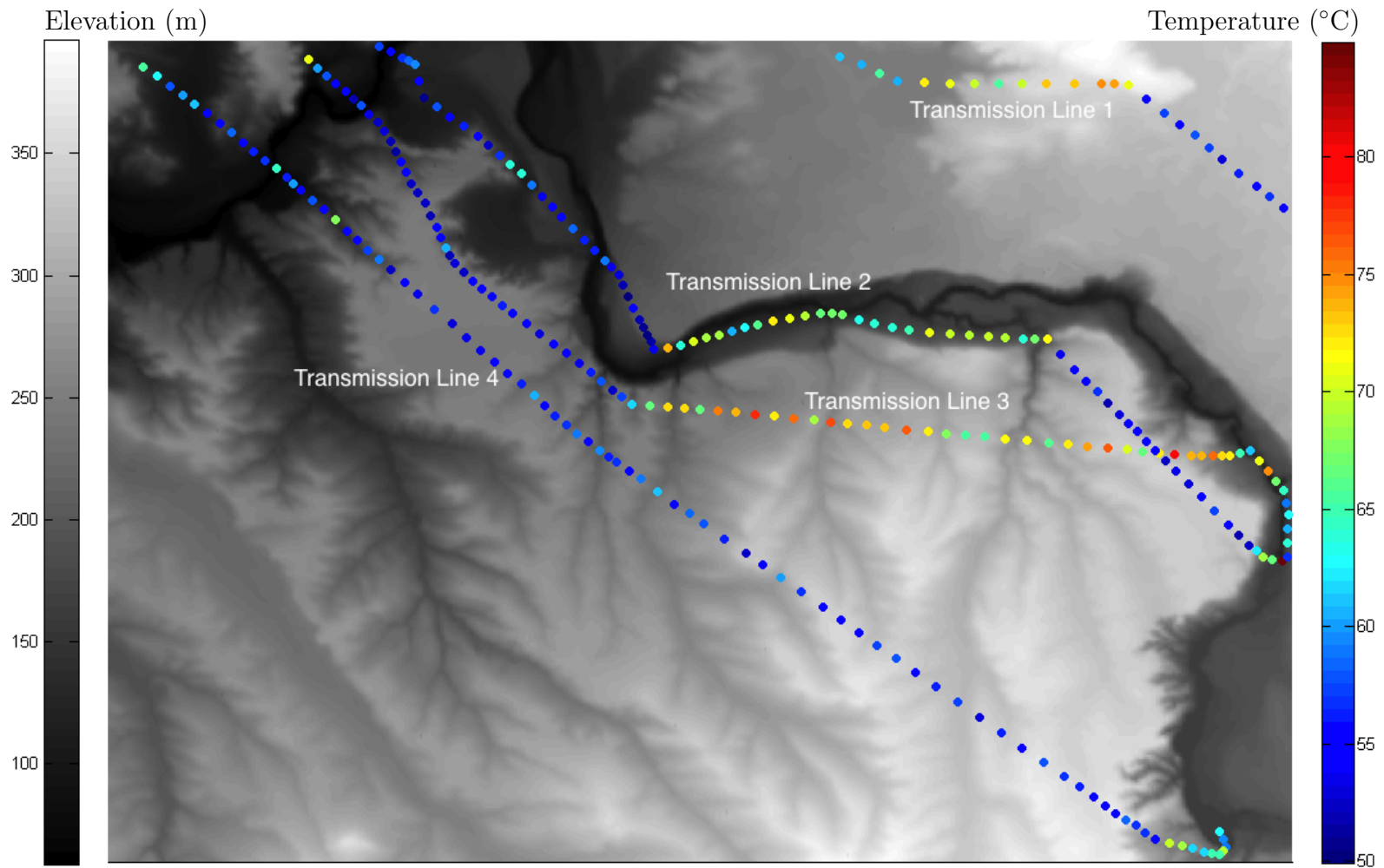


Figure 6.5: Superimposed INL & IPCo test bed area and calculated conductor temperature. The flow field incoming velocity resembles a 12.5 mph wind field out of the east. Temperature is calculated assuming 35°C ambient temperature and 12 W/m solar heating.

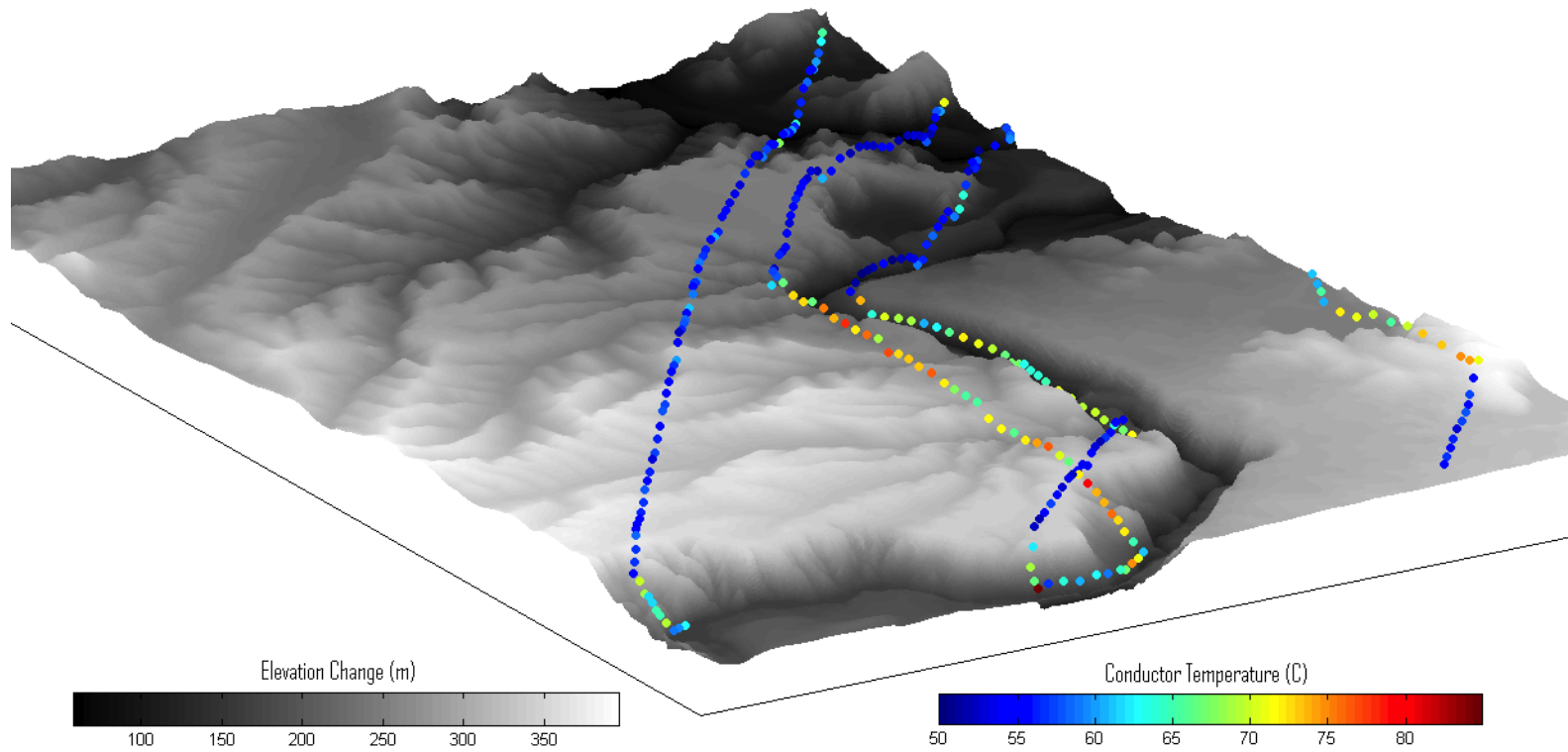


Figure 6.6: Superimposed INL & IPCo test bed area and calculated conductor temperature. The aspect is stretched in the vertical direction by a factor of 6 to better show the terrain.

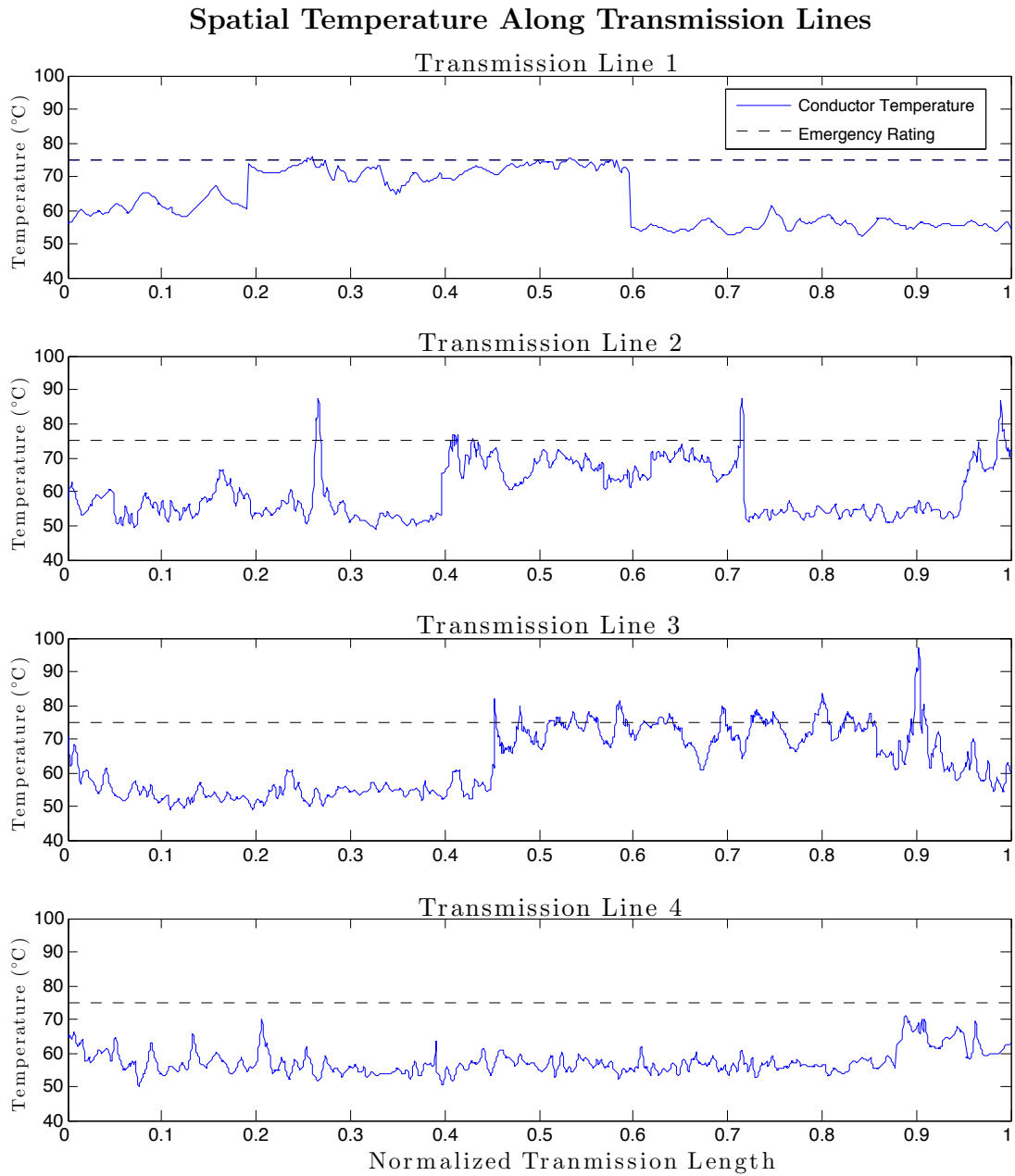


Figure 6.7: Plot of transmission line temperature along its length across the test bed area. Horizontal line represents temperature that indicates emergency ratings, 75°C.

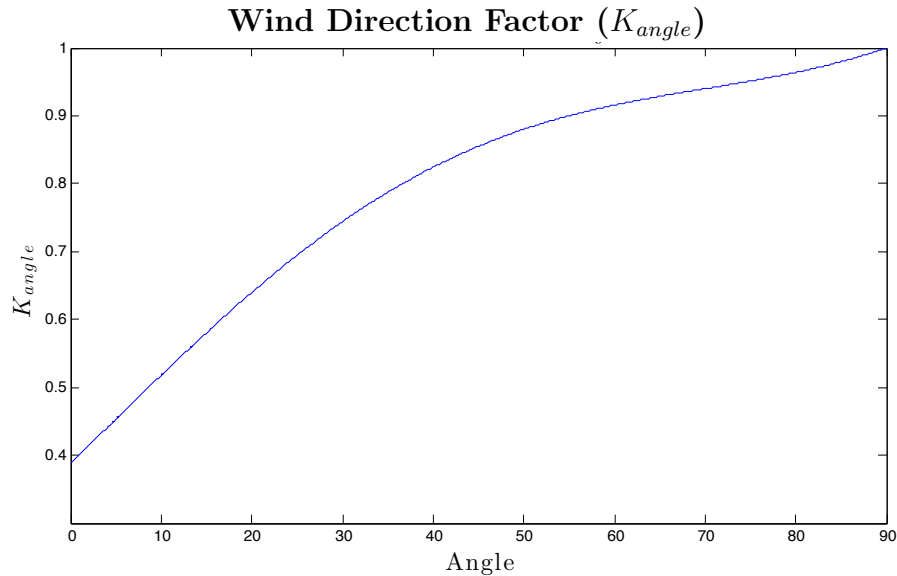


Figure 6.8: Plot showing the sensitivity of the wind direction factor,  $K_{angle}$ , used in convective cooling equations. Here  $0^\circ$  is wind direction parallel to the conductor and  $90^\circ$  is perpendicular.

The effect of wind speed and direction on conductor temperature is clearly visible in Figures 6.5, 6.6, and 6.7. Using current DLR technologies, it would be difficult at best to accurately resolve the spatial temperature differences in this area.

Elevated temperatures occur when the wind direction is parallel to the transmission lines. The increased temperature is caused by the wind direction factor,  $K_{angle}$  given by Equation 3.36, which is used in the IEEE convective cooling calculation. It can be seen in Figure 6.8 that the convective cooling when wind is parallel to conductor is less than 40% of that when it is perpendicular. Additionally, the temperature can be significantly higher in regions of complex terrain due to lower wind speeds. The conductor temperature “spikes” that occur along Transmission line 2, shown in Figure 6.7, may not be resolved if temperature is not determined in highly dense intervals.

Conductor temperature was also compared at weather station locations. The real-

Table 6.1: Calculated conductor temperature using real-time and simulated wind velocity at weather stations.

Weather Station	Simulation Conductor Temperature (°C)	Real-Time Conductor Temperature (°C)	Temperature Difference
1	73.3	75.1	-1.8
2	53.3	53.2	0.1
3	51.5	56.9	-5.4
4	55.1	53.9	1.2
5	59.5	69.5	-9.9
6	67.8	67.2	0.6
8	51.3	53.9	-2.6
9	55.6	55.1	0.6
10	57.6	56.7	0.9
11	53.2	53.2	0.0
14	51.4	56.7	-5.3
15	57.6	65.5	-8.0
16	71.5	75.8	-4.3
17	55.9	55.0	0.9

time temperature was calculated using the mean wind velocity given in the proceeding section, results are tabulated in Table 6.1. It can be seen that even though there were wind velocity outside a standard deviation of real-time wind velocity, all temperature calculations were within 10°C. It should be noted, this may not always be the case, testing with different wind directions as well as speeds must be done before conclusions can be drawn. Also simulations need to assimilate wind variability through time-dependent lateral boundary conditions, which have not been addressed in the present study.

## 6.4 Conclusion

With the use of the wind flow solver under development at BSU, it has been shown that using simulated wind velocity to calculate conductor temperature in dense intervals is a possibility. This DLR method allows spatial temperature differences in conductor temperature to be resolved in much finer detail than currently available DLR technologies.

It has been demonstrated that wind direction as well as velocity is important when determining conductor temperature. Preliminary results show temperature calculations using CFD simulations to be within 10°C of calculations using real-time weather conditions. However, CFD simulations need to assimilate wind variability through time-dependent lateral boundary conditions, which has not been addressed in this study.

## CHAPTER 7

### DLR UTILIZING A TRANSIENT CONDUCTOR TEMPERATURE CALCULATION

The idea of coupling CFD simulations over complex terrain to determine transmission line ampacity using IEEE equations is not new. The DLR method described in [41–43, 45] employs CFD simulations and calculate the IEEE steady-state thermal rating equation to determine real-time ampacity. It is believed that in most situations the error from assuming steady-state is likely to be small, but recognized that under highly variable local weather conditions transient equations may be desired [45]. To date, there has not been any analysis conducted on how the steady-state calculation procedure may affect real-time DLR capacity. Therefore, this chapter will investigate how real-time DLR is affected by the use of steady-state assumptions. A test case scenario is completed using real-time weather data and a constant electrical current applied. Conductor temperature calculations using IEEE steady-state and transient thermal equations are completed and compared.

#### 7.1 INL & IPCo Concurrent Cooling Calculation

INL with funding from the DOE through the WWPTO, and IPCo are researching the use of a library of pre-computed steady-state CFD simulations to dynamically rate transmission lines. The system described in [41–43, 45] uses large volumes of weather

and environmental measurements to identify the pre-computed CFD simulation that best represent current wind conditions. CFD simulations take into account land topography, surface roughness of the terrain, and wind conditions at 17 weather stations over a test area. INL & IPCo team used the WindSim CFD software, the wind field is calculated using the conventional 3-D RANS equations with the standard  $k-\epsilon$  turbulence model for steady-state computations. This technique allows wind conditions to be calculated in dense intervals where no telemetry is available.

WindSim CFD simulations are computationally too intensive to be done in real-time. Therefore, the INL & IPCo team uses a library of pre-computed CFD simulations over the target area. The real-time weather station readings are used to lookup the pre-simulated results that best match current wind conditions. The simulated wind conditions are then applied along the entire length of the transmission line and the ampacity is calculated using the IEEE steady-state thermal rating equation,

$$I = \sqrt{\frac{q_c + q_r - q_s}{R(T_c)}}.$$

Here the steady-state ampacity is calculated using the resistance at the maximum permissible conductor temperature,  $R(T_c)$ .

## 7.2 Transient Calculations for Conductor Temperature

In this analysis, the IEEE transient thermal response of a conductor due to changing environmental conditions is compared with the current steady-state procedure. A transient approach will give a more realistic representation of the conductor temperature due to changing conditions than the current steady-state method allows. Due to a conductor's heat capacity, its temperature does not exhibit an instantaneous

thermal response to changing conditions, like what is implied by the steady-state calculation procedure. A transient calculation approach within a DLR method takes advantage of the the heat capacity of the conductor as well as its initial temperature, which may reduce curtailment on transmission conductor.

It should be noted that it is not possible to directly compare the real-time steady-state calculation procedure, used to determine ampacity, and the transient calculation approach provided in this thesis. The current steady-state method calculates the IEEE steady-state thermal rating equation, which solves the maximum steady-state current a conductor can undergo while staying within its thermal limit, whereas a transient approach calculates the real-time conductor temperature. Therefore, in this analysis, the steady-state temperature is calculated using the IEEE steady-state heat balance equation with a constant electrical load applied. The steady-state conductor temperature is then determined from the conductor resistance, which is given as

$$R(T_c) = \frac{q_c + q_r - q_s}{I^2}. \quad (7.1)$$

Using the calculated resistance, the steady-state conductor temperature is then calculated from tabulated data using a linear interpolation.

A transient method on the other hand calculates the real-time conductor temperature by solving the IEEE ODE governing conductors temperature change in time by employing a 4<sup>th</sup> order RK numerical method. The IEEE transient equation, given as

$$\frac{dT_c}{dt} = \frac{1}{mC_p} [q_j + q_s - q_c - q_r],$$

is described in Section 3.2.2 and the 4<sup>th</sup> order RK numerical method is described in Section 3.3.2.

### 7.2.1 Short-Term Test Case Comparison

This short-term test case scenario used real-time weather data that was sampled in 3 minute time intervals, during the morning hours of July 1<sup>st</sup> 2012. Starling 26/7 ACSR conductor has been selected for this analysis and does not represent IPCo transmission lines. First, the current method, which adopts the IEEE steady-state thermal rating equation, solving the real-time steady-state ampacity having a maximum allowable temperature of 75°C, is shown in Figure 7.1.

The new method, which determines real-time conductor temperature by solving the IEEE transient equation governing conductors temperature change in time, is shown in Figure 7.2. Here a constant load of 849 Amps has been applied and the steady-state conductor temperature, calculated using Equation 7.1, has been shown for comparison. The transient calculation was completed using MATLABs built in ode45 solver using the adaptive time-step algorithm, which maintains an absolute error tolerance below 1E-6.

Unlike the steady-state calculation procedure, the transient calculation does not undergo instantaneous changes in temperature with changing weather conditions. Essentially, the heat capacity creates a “dampening” effect for the temperature response. It can be seen that during times of high wind velocity, the two methods show little difference. However, when low wind velocity occurs, the steady-state method has an instantaneous conductor temperature change that can exceed thermal limits. Only when the initial temperature of the conductor is high or unfavorable wind conditions persist over long time periods does the actual conductor temperature given by the transient calculation exceed thermal limits. When emergency conditions do arise, overhead conductor may be operated at higher temperatures. ACSR is not

### Real-Time vs. Static Ampacity

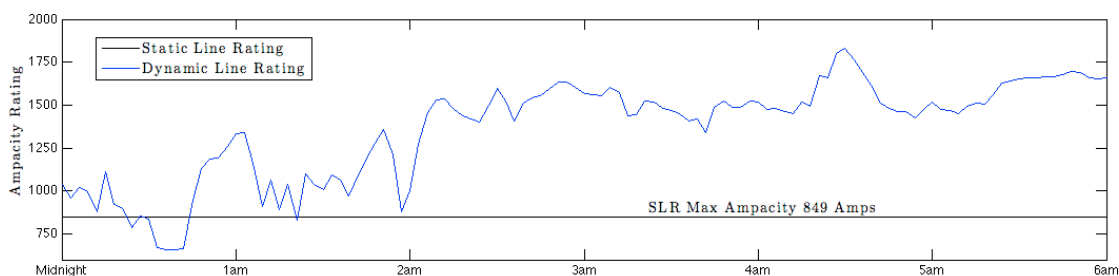


Figure 7.1: Real-time DLR ampacity using the steady-state calculation procedure as described in [41–43, 45].

### Transient vs. Steady-State Conductor Temperature

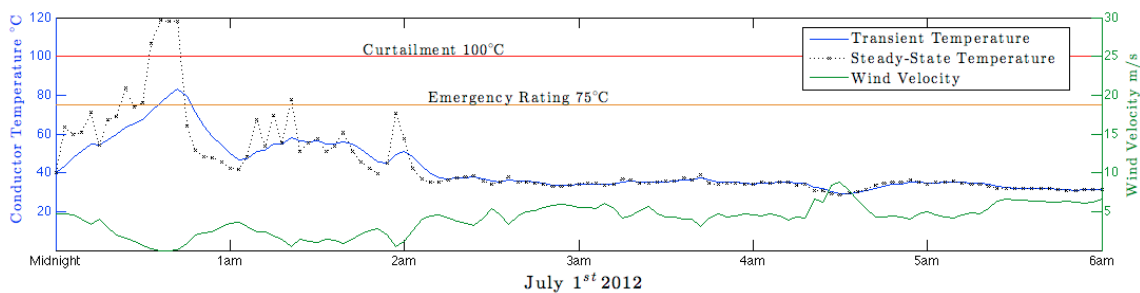


Figure 7.2: Real-time conductor temperature comparison using transient and steady-state equations. The horizontal lines represent the temperature where emergency and curtailment temperatures are reached.

a high-temperature conductor, its rated for 75°C continuous operation but can be operated up to 100°C under emergency operation for a total of 1,500 hours over the conductor life [85]. Temperature in excess of 100°C indicates curtailment is necessary in this analysis.

### 7.2.2 Season Long Test Case Comparison

Real-time summer weather data has been used to compare the steady-state and transient temperature calculations over an entire season. A constant conductor loading of 849 Amps and real-time maximum solar heating under a clear atmosphere as calculated in Section 3.2.2 has been assumed. Resulting temperature calculations between steady-state and transient equations are shown in Figure 7.3, in general the two methods give similar conductor temperature results. The amount of time conductor temperature exceeds emergency ratings show little difference. However, the steady-state calculation procedure results in temperatures that indicate curtailment over four times as often as the transient method; results are tabulated in Table 7.1.

Table 7.1: Time steady-state and transient methods indicate emergency ratings and curtailment. Temperature calculated using summer real-time weather data with a constant 849 Amp load and maximum solar heating.

<b>Thermal Rating</b>	<b>Emergency Ratings</b>	<b>Curtailment</b>
Transient	177:33	26:42
Steady-State	167:12	110:57

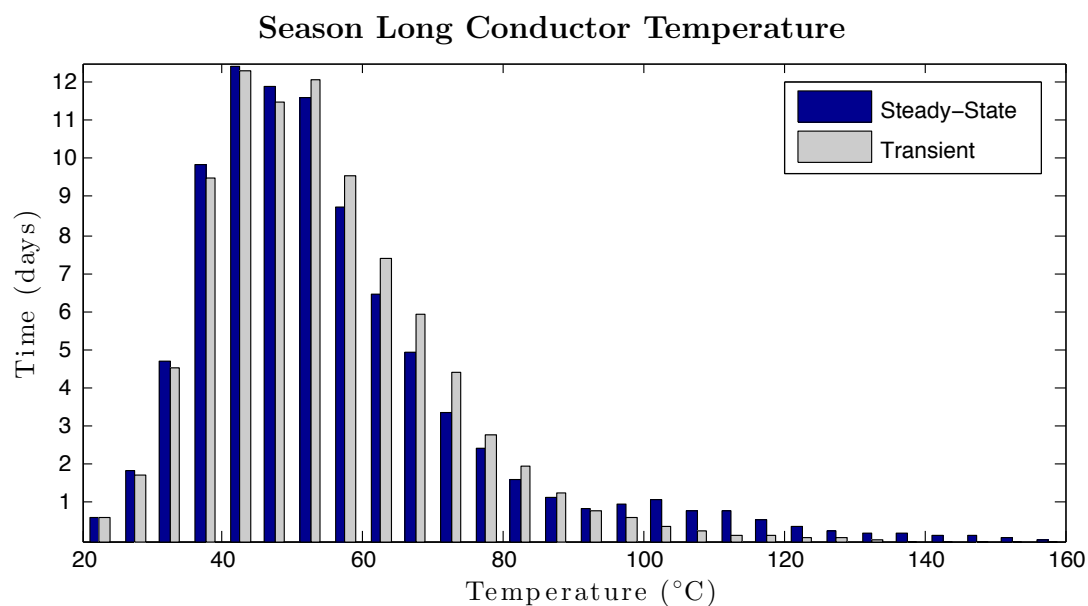


Figure 7.3: Histogram of conductor temperature using real-time summer weather data and a constant load of 849 Amps and maximum solar heating applied.

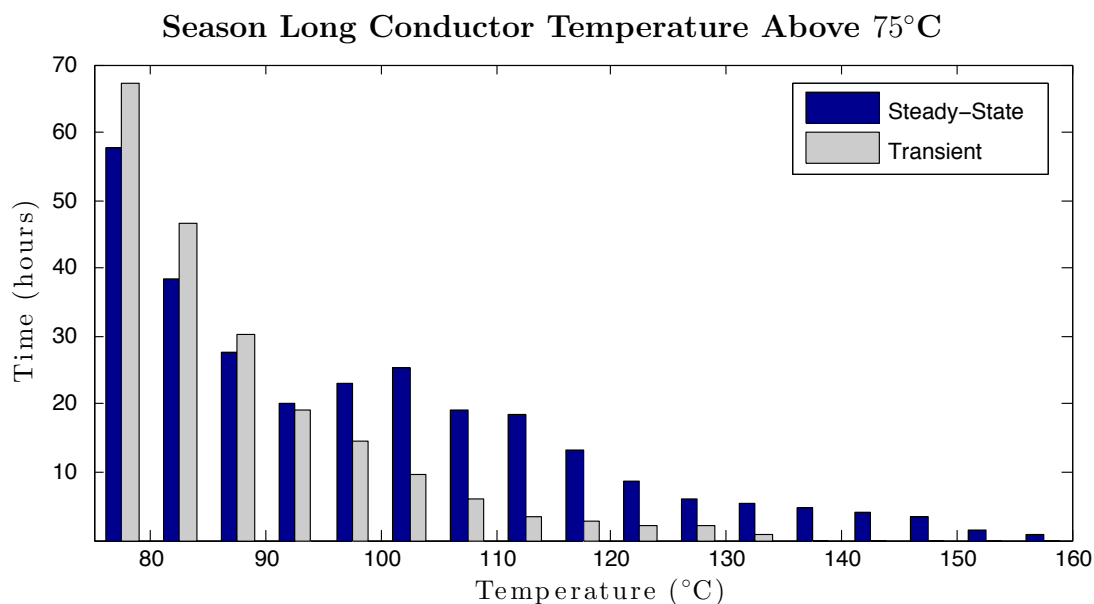


Figure 7.4: Histogram of conductor temperature above 75°C using real-time summer weather data and a constant load of 849 Amps and maximum solar heating applied.

### 7.3 Conclusion

Using real-time weather data, both short-term and season-long analysis has shown the current steady-state thermal rating procedure can overestimate conductor temperature, resulting in unnecessary curtailment. During times of high wind velocity, the two methods show little difference. When low wind velocity occurs the steady-state method has an instantaneous conductor temperature change that can exceed thermal limits. If a transient calculation procedure is adopted, the initial temperature and heat capacity of the conductor is accounted for, giving a more realistic representation of the conductor temperature. This creates a “dampening” effect to the conductors temperature time rate of change. Only when the initial temperature of conductor is high or the unfavorable weather conditions persist over long time periods does the actual conductor temperature given by the transient response exceed thermal limits. Using season long data from the summer, it was shown that the use of a transient method reduces temperature measurements that would indicate curtailment by  $\sim 75\%$ . Therefore, a transient thermal rating approach should be favored in DLR implementations.

## CHAPTER 8

### CONCLUSIONS AND FUTURE DIRECTIONS

#### 8.1 Conclusions

The IEEE Standard 738 equations used to calculate conductor temperature used throughout this study were first validated by coupled CFD and heat transfer analysis. Resulting conductor temperature using CFD simulations were in general agreement with the numerical calculation of equations provided in the IEEE standard, having only  $\sim \pm 2^\circ\text{C}$  difference. Solutions of the ODE that governs conductors transient temperature change were solved using both Euler and 4<sup>th</sup> order Runge-Kutta numerical methods. It was demonstrated that a 4<sup>th</sup> order RK method should be favored over the current Euler method for DLR numerical calculations. The multiple slope estimate gives a more accurate result, allowing for larger time steps to be taken without potential numerical stability issues. This investigation instills confidence in the use of IEEE equations and RK numerical methods to be used in a DLR technology.

Data from the INL & IPCo collaborative test bed area for DLR research was successfully used to show the increased electrical capacity available over the current static rating procedure. The probability of capacity ratings were calculated hourly for each season of the year. The strong connection between wind velocity and conductor temperature allows capacity to be increased by  $\sim 70\%$  when local wind generation can be expected.

The use of CFD simulations for DLR described in [41–43, 45], where the IEEE steady-state thermal rating equation used to determine ampacity has been compared to a transient approach. It has been assumed that the use of steady-state equations result in little error due to the thermal time constant being on the order of 15–20 minutes. However, it was shown that the use of transient equations, which give a more accurate representation of the actual conductor temperature, indicate that the conductor will less often reach temperatures that would indicate curtailment is necessary. Therefore, adopting a transient equation should be favored, potentially helping TSPs transfer electricity more efficiently.

During the course of this study, GPU-accelerated numerical wind solver results over complex terrain were successfully extracted and applied along transmission lines to solve conductor temperature using IEEE Standard 738 equations. This provides the foundation for a DLR technology that could potentially be implemented by a TSP to determine real-time conductor temperatures using a short-term wind forecasting application.

## 8.2 Future Directions

This thesis laid the foundation for developing a DLR technology that calculates conductor temperature in real-time, utilizing a short-term micro-scale wind forecasting solver over complex terrain. Initial attempts at simulating wind over complex terrain and matching real-time data have proven difficult, showing further research and testing is necessary. First, weather station locations needs to be done in a more accurate way than digitization; GPS coordinates should be implemented to ensure correct placement in the resulting wind flow field. Wind simulations need to be

ran in multiple directions as well as velocity before any conclusions of wind velocity accuracy across the test bed can be drawn, as well as a grid refinement study. A systematic analysis of both solution accuracy and computational performance of the flow solver needs to be completed.

Future directions of the numerical wind solver being developed at BSU are as follows: Periodic lateral boundary conditions should be replaced with open lateral boundary conditions. Integrating an adaptive mesh refinement, allowing areas of high interest, terrain along transmission lines, to be refined while areas away from transmission lines could be coarsened. Incorporation of surface fluxes to be accounted for, and possibly coupling of the flow solver with a meso-scale forecasting simulation such as the Weather Research and Forecasting (WRF) model.

Initial analysis of transmission capacity available in the INL & IPCo test bed area indicate current static methods are limiting capacity, however only a single weather station along the transmission line was used. Future capacity analysis should include all weather station along the length of the transmission line, using only the limiting stations capacity along all transmission lines that traverse the test bed area.

## REFERENCES

- [1] Transmission conductors thermal ratings. Report by Transmission Advisory Panel, East Central Area Reliability Coordination Agreement, 68-TAP-28.
- [2] *Aluminum Electrical Conductor Handbook*. Washington, DC, 2 edition, 1982.
- [3] Electricity grid modernization: Progress being made on cybersecurity guidelines, but key challenges remain to be addressed. Technical Report GAO-11-117, United States Government Accountability Office, January 2011.
- [4] The Valley Group a Nexans company. CAT-1 transmission line monitoring system: Optimize your network capabilities.
- [5] Energy Information Administration. Annual energy outlook 2013: Growth in electricity use slows but still increases by 28 percent from 2011 to 2040. Technical report, Energy Information Administration, 2013.
- [6] C. Donald Ahrens. *Meteorology Today: An Introduction to Weather, Climate, and the Environment*. West Publishing Company, St. Paul, MN, 1994.
- [7] ALSTOM. *MiCOM ALSTOM P341: Dynamic Line Rating*.
- [8] Ampacimon. *Innovative solution for Dynamic Line Rating: Direct sag determination based on conductor vibrations measurement*.
- [9] ANSYS, Inc., Canonsburg, PA. *Documentation for ANSYS ICEM CFD 13.0*, 2010.
- [10] ANSYS, Inc., Canonsburg, PA. *ANSYS Fluent 14.0: Theory Guide*, November 2011.
- [11] M. Aten, R. Ferris, T. Yip, C. An, and G. Lloyd. Field measurements analysis for dynamic line rating. In *21<sup>st</sup> International Conference on Electricity Distribution*, June 2011.
- [12] Avistar. Dynamic line rating: Monitor conductor ampacity to enhance transmission system performance.

- [13] P. D. Belben and C. D. Ziesler. Aeolian uprating: how wind farms can solve their own transmission problems. Berlin, Germany, July 2002. Proceedings of 1<sup>st</sup> World Wind Energy Conference and Exhibition.
- [14] M. Bhaskar, A. Jain, and N. Venkata Srinath. Wind speed forecasting: Present status. *Power System Technology (POWERCON), 2010 International Conference*, pages 1–6, October 2010.
- [15] W. Z. Black and W. R. Byrd. Real-time ampacity model for overhead lines. *IEEE Transactions on Power Apparatus and Systems*, PAS-102(7):2289–2293, July 1983.
- [16] G. Bontempi, A. Vaccaro, and D. Villacci. Data-driven calibration of power conductors thermal model for overhead lines overload protection. *International Journal of Reliability and Safety*, 2(1):5–18, 2008.
- [17] G. Botta. Wind analysis on complex terrain: The case of acqua spruzza. *Wind Engineering and Industrial Aerodynamics*, 39:357–366, 1992.
- [18] S. C. Chapra and R. P. Canale. *Numerical Methods for Engineers*. McGraw Hill, Boston, MA, 6 edition, 2010.
- [19] S. Chung. Idaho national laboratory: Inl wind research test cool way to stretch capacity of existing power lines.
- [20] CIGRE WG 12, ELECTRA 144. *The Thermal Behaviour of Overhead Conductors*, 1992.
- [21] B. Clairmont, D.A. Douglass, J. Inglesias, and Z. Peter. Radial and longitudinal temperature gradients in bare stranded conductors with high current densities. Technical Report B2-108, CIGRE, Paris, 2012.
- [22] COMSOL Inc, Palo Alto, CA. *COMSOL*, 2014.
- [23] United States Congress. Public utility holding company act of 1935.
- [24] North American Reliability Corporation. 2009 long-term reliability assessment. Technical report, November 2009.
- [25] North American Reliability Corporation. 2012 long-term reliability assessment. Technical report, 2012.
- [26] A. K. Deb. *Powerline Ampacity System; Theory, Modeling, and Applications*. CRC Press, Boca Raton London New York Washington, D.C., 2000.

- [27] R. DeLeon, K. Felzien, and I. Senocak. Toward a GPU-accelerated immersed boundary method for wind forecasting over complex terrain. *ASME 2012 Fluids Engineering Division Summer Meeting*, 1, July 8–12 2012.
- [28] Prometheus Devices. *RT-TLMS: Real Time - Transmission Line Monitoring System*.
- [29] DOE. What is the Smart Grid?  
[http://www.smartgrid.gov/the\\_smart\\_grid#smart\\_grid](http://www.smartgrid.gov/the_smart_grid#smart_grid).
- [30] D. A. Douglas, T. O. Seppa, M. L. Oatts, and A. A. Edris. Real-time-monitoring and dynamic thermal rating of power transmission circuits. *IEEE transactions on power delivery*, 11(3):1407–1418, 1996.
- [31] D. A. Douglass, A. A. Edris, and G. A. Prichard. Field application of a dynamic thermal circuit rating method. *IEEE Transactions on Power Delivery*, volume 12(2), 1997.
- [32] DTU Wind Energy, Denmark. *Wind Analysis and Application Program (WAsP)*, 2014.
- [33] Electric Power Research Institute. *Increased Power Flow Guidebook: Increasing Power Flow in Transmission and Substation Circuits*, 2005.
- [34] S. Emeis. *Wind Energy Meteorology: Atmospheric Physics for Wind Power Generation*. Springer, Verlag Berlin Heidelberg, 2013.
- [35] Learn Engineering. Computational fluid dynamics: Rans & fvm, May 2013.
- [36] ERCOT. About ercot. <http://www.ercot.com/about/>.
- [37] L. Fish. Power donut systems for overhead electric power line monitoring operator overview. Technical report, USi, November 2012.
- [38] J. Fu, D. J. Morrow, and S. M. Abdelkader. Modelling and prediction techniques for dynamic overhead line rating. *Power and Energy Society General Meeting*, pages 1–7, July 2012.
- [39] J. Fu, J. D. Morrow, S. Abdelkader, and B. Fox. Impact of dynamic line rating on power systems. *Universities' Power Engineering Conference*, pages 1–5, Sept 2011.
- [40] J. R. Garratt. *The Atmospheric Boundary Layer*. Cambridge University Press, 1992.

- [41] J. Gentle, K. S. Myers, T. Baldwin, I. West, K. Hart, B. Savage, M. Ellis, and P. Anderson. Concurrent wind cooling in power transmission lines. In *2012 Western Energy Policy Research Conference*. Idaho National Laboratory, August 2012.
- [42] J. P. Gentle, K. S. Myers, J. W. Bush, and S. A. Carnohan. Dynamic line rating systems in the u.s.: Policy and reliability. Technical report, INL/EXT-13-28553, 2013.
- [43] J. P. Gentle, K. S. Myers, I. J. West, P. Anderson, K. Hart, and M. Ellis. Wind modeling to predict cooling in transmission lines. Technical report.
- [44] J. Duncan Glover, M. Sarma, and T. Overbye. *Power System Analysis and Design*. Cengage Learning, Stamford, CT, 5th edition, 2010.
- [45] D. M. Greenwood, J. P. Gentle, G. L. Ingram, P. J. Davison, K. S. Myers, I. J. West, J. W. Bush, and M. C. M. Troffaes. A comparison of real time thermal rating systems in the u.s. and the uk. Technical Report INL/EXT-13-28553, Idaho National Laboratory, March 2013.
- [46] D. M. Greenwood, G. L. Ingram, and P. C. Taylor. Improving real-time thermal ratings using computational wind simulations. 10th Wind Integration Workshop, 2011.
- [47] K. Hur, M. Boddeti, N. D. R. Sarma, J. Dumas, J. Adams, and S. K. Chai. High-wire act: Ercot balances transmission flows for texas-size savings using dynamic thermal ratings application. *IEEE Power and Energy Magazine*, pages 37–45, January 2010.
- [48] IEEE, New York, NY. *IEEE Standard for Calculation the Current-Temperature of Bar Overhead Conductors. IEEE std 738-2006*, January 2007.
- [49] F. P. Incropera and D. P. DeWitt. *Fundamentals of Heat and Mass Transfer*. John Wiley and Sons Inc, New York, NY, 4 edition, 1996.
- [50] D. A. Jacobsen and I. Senocak. Multi-level parallelism for incompressible flow computations on GPU clusters. *Parallel Computing*, 39(1):1 – 20, 2013.
- [51] J. Johnson. Smart grid demonstration project: Dynamic line rating (dlr). Technical report, Oncor Electric Delivery Company, June 2010.
- [52] J. D. Anderson Jr. *Fundamentals of Aerodynamics*. McGraw Hill, 1995.
- [53] J. C. Kaimal and J. J. Finnigan. *Atmospheric Boundary Layer Flows: Their Structure and Measurements*. Oxford University Press, New York, NY, 1994.

- [54] S. M. Kaplan. Electric power transmission: Background and policy issues. Technical report, Congressional Research Service, April 2009.
- [55] A. Keating, U. Piomelli, E. Balaras, and H.J. Kaltenbach. A priori and a posteriori test of inflow conditions for large-eddy simulation. *Physics fo Fluids*, 16(12):4696–4712, 2004.
- [56] M. Lesieur, O. Metais, and P. Comte. *Large-Eddy Simulations of Turbulence*. Cambridge University Press, 2005.
- [57] G. Lloyd, G. Millar, T. Yip, and C. An. Design and field experience of a dynamic line rating protection. *Advanced Power System Automation and Proteteton*, 2:1068–1073, October 2011.
- [58] G. M. Masters. *Renewable and Efficient Electric Power Systems*. Wiley, Hoboken, NJ, 2004.
- [59] The Math Works, Inc, Natick, Massachusetts, United States. *MATLAB Release 2012a*.
- [60] J. H. Mathews and K. D. Fink. *Numerical Methods Using MATLAB*. Pearson Prentice Hall, Upper Saddle River, N.J., 4 edition, 2004.
- [61] C. Meneveau, T. Lund, and W. Cabot. A Lagrangian dynamic subgrid-scale model of turbulence. *Journal of Fluid Mechanics*, 319:353–385, 1996.
- [62] A. Michiorri, P. C. Taylor, and S. C. E. Jupe. Overhead line ral-time rating estimation algorithm: description and validation. *IMechE Part A: J. Power and Energy*, 224:293–304, 2009.
- [63] P. D. Moeller. Ferc commissioner. In National Conference of State Legislatures 2007 Annual Meeting, editor, *Constructing New Transmission Lines: Implications of the Energy Policy Act*, page 6, Boston, MA, August 2007.
- [64] B. R. Munson, T. H. Okiishi, W. W. Huebsch, and A. P. Rothmayer. *Fundamentals of Fluid Mechanics*. John Wiley and Sons Inc, New York, NY, 7 edition, 2013.
- [65] M. Negnevitsky, P. Mandal, and A. K. Srivastava. An overview of forecasting problems and techniques in power systems. *Power Energy Society General Meeting, 2009. PES 2009. IEEE*, pages 1–4, July 2009.
- [66] J. M. A. Nuijten, A. Geschiere, J. C. Smit, and G. J. Frijmersum. Future network planning and grid control. In *Future Power Systems, 2005 International Conference*, page 7, November 2005.

- [67] United States of America Federal Energy Regulatory Commission. *Order No. 888*, April 1996.
- [68] Department of Energy. 20% wind energy by 2030: Increasing wind energy's contribution to u.s. electricity supply. Technical Report DOE/GO-102008-2567, Department of Energy, July 2008.
- [69] P. Oreschnick. Dynamic rating allows more wind generation. *Transmission and Distribution World*, 59(11):58, 2007.
- [70] D. L. Pearce and C. D. Ziesler. Using cfd modelling to improve the estimation of offshore wind resource. *IMEchE Seminar: Power Generation by Renewables*, pages 207–219, 2000.
- [71] Pike Energy Solutions. *The ThermalRate System*.
- [72] U. Piomelli. Wall-layer models for large-eddy simulations. *Progress in Aerospace Sciences*, 44(6):437, 2008.
- [73] M. R. Raupach, R. A. Antania, and S. Rajagopalan. Rough-wall turbulent boundary layers. *American Society of Mechanical Engineers*, 44(1), January 1991.
- [74] Strategic Energy Research. Dynamic circuit thermal line rating. Technical report, California Energy Commission, October 1999.
- [75] P. Sagaut. *Large Eddy Simulation for Incompressible Flows: An Introduction*. Springer-Verlag Berlin Heidelberg, 2002.
- [76] P. Schavemaker and L. van der Sluis. *Electrical Power System Essentials*. John Wiley and Sons Inc, Hoboken, NJ, 2008.
- [77] S. H. Schneider, M. D. Mastrandrea, and T. L. Root. Encyclopedia of climate and weather. Technical report, Oxford University Press, 2011.
- [78] I. Senocak, A. Ackerman, M. Kirkpatrick, D. Stevens, and N. Mansour. Study of near-surface models for large-eddy simulations of a neutrally stratified atmospheric boundary layer. *Boundary-Layer Meteorology*, 124:405–424, 2007.
- [79] I. Senocak, A. S. Ackerman, D. E. Stevens, and N. N. Mansour. Topography modeling in atmospheric flows using the immersed boundary method. In *Annual Research Briefs*, pages 331–341. Center for Turbulence Research, NASA-Ames/Stanford Univ., Palo Alto, CA, 2004.

- [80] T. O. Seppa. A practical approach for increasing the thermal capabilities of transmission lines. *IEEE Transactions on Power Delivery*, 8(3):1536–1550, July 1993.
- [81] T. O. Seppa, R. D. Mohr, and J. Stovall. Error sources of real-time ratings based on conductor temperature measurements. *CIGRE WG B2.36 Guide on Direct Real Time Rating Systems*, pages 20–21, May 2010.
- [82] D. Shepard. A two-dimensional interpolation function for irregularly-spaced data. 1968 23rd ACM national conference, 1968.
- [83] D. Solan. From federal preemption politics to regional transmission planning and policy integration. *The Electricity Journal*, 25(9):25–36, Nov 2012.
- [84] S. S. Soman, H. Zareipour, O. Malik, and P. Mandal. A review of wind power and wind speed forecasting methods with different time horizons. *North American Power Symposium (NAPS)*, pages 1–8, September 2010.
- [85] Southwire Company, Carrollton, Ga. *Overhead Conductor Manual*, 2007.
- [86] L. Staszewski and W. Rebizant. The differences between IEEE and CIGRE heat balance concepts for line ampacity considerations. *Modern Electric Power Systems*, pages 26–29, 2010.
- [87] D. M. Stephen. Determination of the thermal rating and uprating methods for existing lines. *ELECTRA*, 2000.
- [88] R. B. Stull. *An Introduction to Boundary Layer Meteorology*. Kluwer Academic Publishers, Dordrecht, Netherlands, 1988.
- [89] Idaho The Weather Channel: Monthly Weather for Boise, <http://www.weather.com/weather/wxclimatology/monthly/graph/USID0025> 2013.
- [90] J. C. Thibault and I. Senocak. Accelerating incompressible flow computations with a Pthreads-CUDA implementation on small-footprint multi-GPU platforms. *Journal of Supercomputing*, 59(2):693–719, 2012.
- [91] U.S. Congress. *Energy Policy Act of 1992*, 1992.
- [92] S. Uski-Joutsenvuo, R. Pasonen, and S. Rissanen. Maximising power line transmission capability by employing dynamic line ratings: Technical survey and applicability in Finland. Technical report, VTT, May 2012.
- [93] S. P. Vajjhala and P. S. Fischbeck. Quantifying siting difficulty: A case study of U.S. transmission line siting. Technical report, Washington, DC, February 2006.

- [94] H. K. Versteeg and W. Malalasekera. *An Introduction to Computational Fluid Dynamics: The Finite Volume Method*. Prentice Hall, 2nd edition, 2007.
- [95] M. L. Wald. Ideas to bolster power grid run up against the system's many owners. *The New York Times*, July 2013.
- [96] J. M. Wallace and P. V. Hobbs. *Atmospheric Science: An Introductory Survey*, volume 92 of *International Geophysics Series*. Elsevier, San Francisco, CA, 2 edition, 2006.
- [97] C. J. Yang. Electrical transmission: Barriers and policy solutions. Technical report, Duke University, August 2009.
- [98] Y. Yi, R. G. Harley, D. Divan, and T. G. Habetler. Overhead conductor thermal dynamics identification by using echo state networks. pages 3436–3443, Atlanta, Georgia, June 2009. International Joint Conference on Neural Networks.
- [99] T. Yip, C. An, G. Lloyd, M. Aten, and B. Gerris. Dynamic line rating protection for wind farm connections. *Integration of Wide-Scale Renewable Resources Into the Power Delivery System*, pages 1–5, July 2009.